Department of Physics and Astronomy
University College London

The role of physics in epithelial homeostasis and development

Aida Mehonić

Supervisor: Prof Tom Duke

Dissertation submitted
for the degree of Doctor of Philosophy

August, 2011

I, Aida Mehonić confirm that the work presented in this thesis is my own. Where information has been derived from other sources, I confirm that this has been indicated in the thesis.

Abstract

Developing epithelial tissues are characterised by the disordered cell packing caused by ongoing cell proliferation and changes in tissue size. However, cell packing in adult epithelial tissues exhibits a high level of order, and typically, the apical tissue surface resembles a regular hexagonal lattice of planar polygons.

One of the central questions in tissue development concerns the mechanisms which induce cells to repack. The change in packing may transform the tissue into a regular pattern of hexagonal cells, as seen during the refinement of *Drosophila M.* wing and notum tissue, or it can occur as a mechanism which drives tissue shape change, as seen during embryonal axis elongation during *Drosophila* convergent extension.

We study cell repacking in epithelia effected by the forces that act at the interface between adjacent cells. To this end, we develop a mechanical model of epithelial tissue based on the ideas of the cellular Potts model and building on previous vertex models. Analysing expanding and fixed-size tissues, we find that steady state packing geometries depend on the regularity in the timing of cell divisions.

We predict that cells in topologically active epithelia leave the tissue in response to mechanical compression and geometric anisotropy. Through a collaboration with biologists Eliana Marinari and Buzz Baum, we find that such mechanically driven cell delamination indeed occurs in the *Drosophila* notum. We thus identify a novel process of tissue homeostasis, whereby live cells delaminate from developing epithelium in order to limit overcrowding.

Analysing the relation between stable packing geometries and the mechanical parameters, we suggest that an increase in the strength of acto-myosin contractility alone could cause tissue to repack into a regular lattice.

Modifying the model to describe polarised acto-myosin localisation, we computationally reproduce cell intercalation and actin cable and rosette formation during convergent extension in *Drosophila*.

Contents

Acknowledgements

I would like to thank everybody who supported me during my doctorate at UCL.

I am greatly indebted to my supervisor Prof Tom Duke for his enduring patience, support and generosity with his time and advice. It was a long and uncertain journey from a mathematics graduate to a PhD in biophysics, and I am deeply grateful to Tom for his constant supervision and guidance along the way.

Also, I am grateful to Dr Buzz Baum who taught me a great deal about how to formulate and test hypotheses in biology. I thank Dr Eliana Marinari for being a perfect collaborator and for sharing the ups and downs of our research, especially in the final year of our PhDs.

I am also indebted to Simon Myerson for numerous fruitful discussions. Further, I thank all the colleagues at the LCN who've shared their knowledge and experience with me, and especially Dr Andrea Jimenéz-Dalmaroni, Dorothy Kuipers, Dr Guillaume Charras, Dr Marc Warner, Angie Ma, Dr Mathew Kallumadil, Dr Alex Sena and Dr Simon Gane.

I use this opportunity to remember late Prof Marshall Stoneham whose advice and kind concern for my academic progress were encouraging and inspirational.

Finally, my deepest thanks to all my family and numerous friends in Sarajevo, London and all around the world, for their patience, support and laughs.

Chapter 1

Introduction

1.1 Motivation

Epithelial tissue is an essential component of animal body architecture. It is found in the lining of all internal body cavities and in the skin. The inner layers of blood vessels, respiratory and digestive tubes are formed of epithelia. Specialised epithelial sheets which transduct sensory stimuli into electrochemical signals are found in the eye, ear, nose, tongue and epidermis. Epithelial layers also have important roles in secretion, selective absorption and transcellular transport. Carcinomas, which account for about 90% of human cancers, originate in epithelial tissues.

The primary function of epithelial tissue is to provide a barrier, and this dictates its structure: it must be tightly packed. However, epithelia constantly renew during the life of an organism and so there must exist mechanisms which insure that tissue uniformity is preserved, even as individual cells die and get recycled or divide to form new cells. These processes are the homeostatic processes of life, which maintain structural and functional robustness of living tissues and organs. When *homeostasis* is disrupted, the life-preserving functions of epithelial tissue are in danger. For example, when tumours form, epithelial homeostasis is damaged and altered.

Proper formation of epithelia during organism *development* is essential for their function. For example, a certain type of hearing loss in mammals is caused by improper formation of the sensory epithelial sheet in the inner ear. Cells in these sensory epithelia are typically packed in regular hexagonal arrays (Figure 1.1), with the bundles of stereocilia pointing in the same direction. The stereocilia must be precisely

aligned in order to detect the movement of the ambient fluid and thus detect sound (Lewis and Davies [1]). Once damaged, the sensory epithelium does not regenerate in humans, but it does regenerate in birds. Detailed understanding of the mechanisms which guide the development of the sensory epithelial sheet could point the way to inducing its regeneration in humans (López-Schier and Hudspeth [2]).

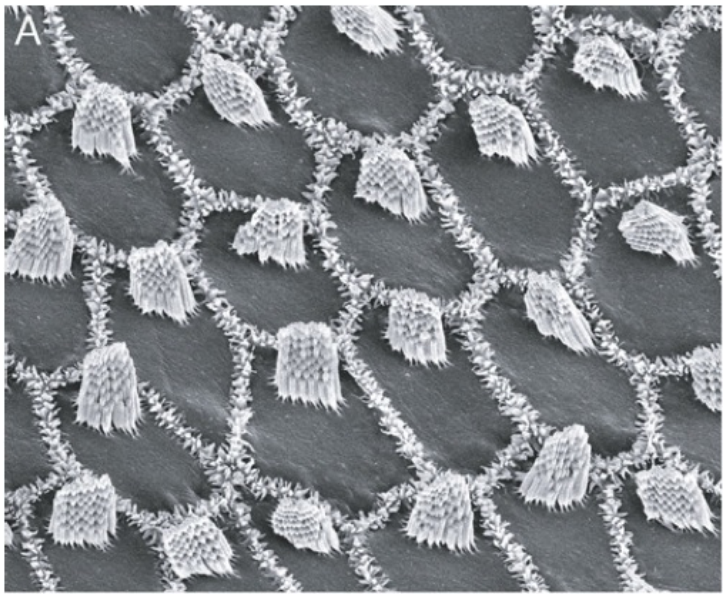

Figure 1.1: High level of order in epithelial tissues is essential for their proper function. Apical view of hair cells in chick cochlea shows cells packed in a regular hexagonal lattice. Adapted from Hudspeth [3].

Cell packing in epithelia is determined by internal cellular mechanics and by contacts along the junctions between two cells. Therefore, the understanding of the mechanisms which regulate cell packing must come from careful study of the mechanical properties of tissues. These findings in turn will crucially contribute to our understanding of normal tissue structure, wound healing and cancer origination (Butcher et al [4]).

More specifically, we are interested in understanding how cellular packing arises in tissue development. Is packing the same for a growing tissue which is free to expand and for a growing tissue whose size is restricted by a physical boundary? Does the timing of cell divisions have an appreciable effect on steady state statistical properties of the tissue in either case? And what is the cellular packing in an adult homeostatic

tissue of fixed size, in which the new cells created by division are balanced, on average, by an equal number that are extruded from the tissue?

Further, we would like to understand how tissue can be remodelled as a result of internal forces. For example, when two separate tissues meet and fuse, as they do in the process of dorsal closure, how does the initial perturbation in geometry get smoothed out to yield a single, uniform tissue. More generally, how does a disorganised tissue, with a broad distribution of cell sizes and shapes, become more ordered such that the cells are mostly hexagonally packed? And in morphogenetic processes such as convergent extension, what changes in the mechanical properties of individual cells lead to the gross changes in tissue shape?

Finally, it is of interest to contemplate the role of stochasticity in all of these processes. The mechanical forces that drive the evolution of tissue geometry and topology are molecular in origin, and thus subject to a significant degree of fluctuation. Might the consequent noise play a constructive part in the remodelling of tissue by helping to anneal the system, which might otherwise get trapped in local minima of mechanical energy?

1.2 Model tissue: *Drosophila* epithelium

The epithelia in *Drosophila* are thin sheets of cells without extracellular matrix. They have a relatively simple structure, and contain few types of cells.

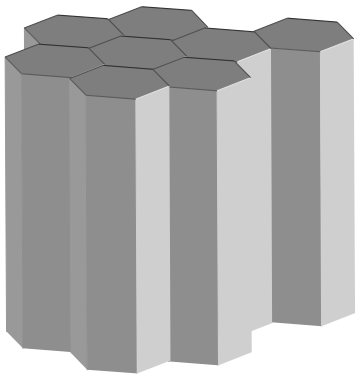

Figure 1.2: A simplified diagram of a developing *Drosophila* epithelium. The cells in the *Drosophila* notum have a diameter-to-height ratio of around 1:5.

The primary model tissue used in the studies described in this thesis is the pupal notum of *Drosophila Melanogaster*. The notum is a monolayer epithelium which forms when two imaginal wing discs fuse during embryogenesis along the midline of the developing back. This process of fusion is called dorsal closure, or more specifically, thorax closure (Zeitlinger et al [5]). In metamorphosis, the notum transforms into the thorax of an adult fly. The different stages of Drosophila development are illustrated in Figure 1.3, and the adult body layout is labelled in Figure 1.4.

We chose to study the notum because it undergoes substantial changes in cellular packing and cell shape during the final stages of its development. However, the overall tissue size and shape remain the same. Therefore, it is suitable for studying the mechanisms of cell repacking that lead to tissue reordering and refinement, without having to take into account overall tissue shape changes. The precise period studied is between 12h and 26h after pupa formation (AP).

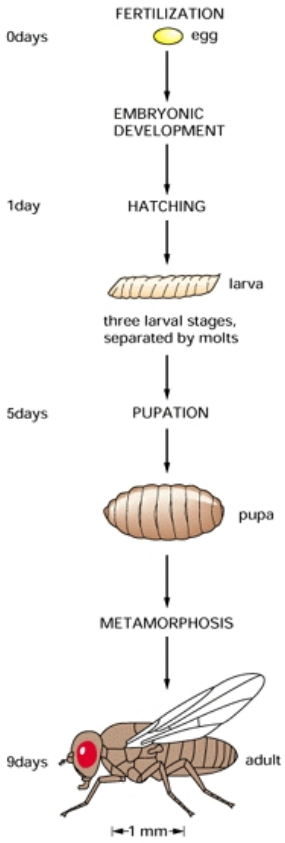

Figure 1.3: Drosophila developmental stages. Adapted from Alberts et al [10].

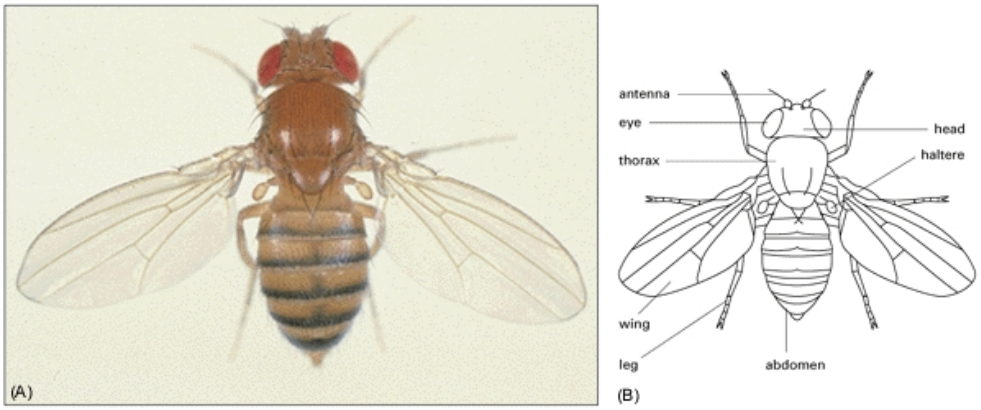

Figure 1.4: **(A)** A photograph showing a dorsal view of an adult *Drosophila Melanogaster*, and **(B)** A schematic indicating different body parts. Adapted from Alberts et al [10].

Cell packing in the notum at 12h after pupariation is largely disordered. Cell size and cell shape vary and the cells in the midline region of the notum are elongated and have wiggly junctions. The size of the notum is fixed during the next 14 hours, but the tissue itself is dynamic. Cells go through several rounds of cell divisions and the cellular packing changes significantly in two ways: cells become more regularly packed approaching a regular hexagonal lattice, and the elongation of cells in the midline region disappears so that the whole tissue reaches an isotropic state.

The phenomenon of tissue reordering into a regular hexagonal lattice has been reported for various developing epithelia (*Drosophila* eye: Käfer et al [6], Hayashi and Carthew [7], *Drosophila* wing: Classen et al [8]) and has been increasingly studied in recent years.

Drosophila wing disc undergoes repacking from a disordered into a quasi-hexagonal lattice (Classen at al [8]) as shown in Figure 1.5. The arrangement of cells into a regular quasi-hexagonal lattice is thought to be important for tissue patterning. The epithelial hairs start growing shortly after the tissue repacks and are conditioned by the prexistence of a hexagonal array. The precise arrangement of the hairs guides the airflow around the wings so as to facilitate the flight (Wootton [9]).

The thorax of an adult fly also exhibits clear patterning - the bristles that grow out of it are precisely arranged (Simpson [11], Simpson [12], Simpson [13], Calleja et al [14]). The positional patterning of the bristles is thought to closely depend

on the hexagonal cellular arrangement in the notum. Since the bristles have a sensory function in the adult fly, it is likely that their precise positional arrangement is important.

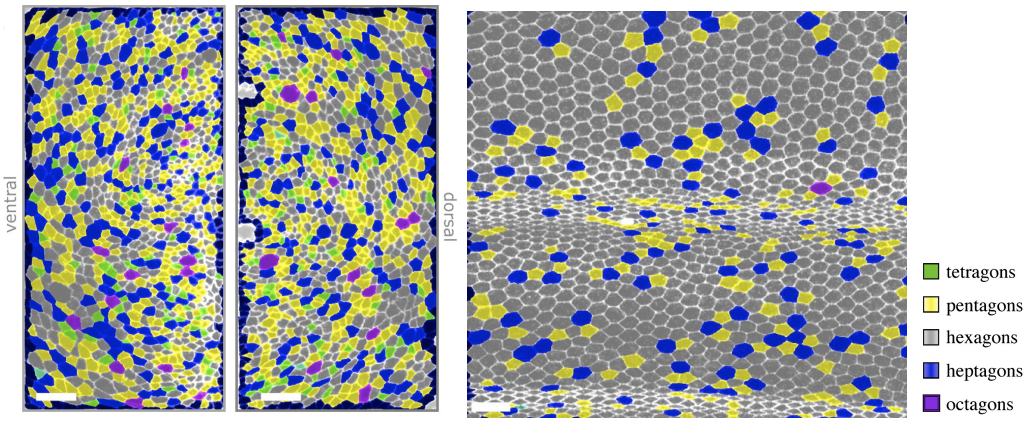

Figure 1.5: Cells in the wing epithelium repack to approach a regular hexagonal lattice. Images of *Drosophila* wings, at (left): the larval stage, and (right): the late pupal stage of development. Adapted from Classen et al [8].

The tissue comprising the *Drosophila* notum, wing (Doyle et al [15]) and retina (Lawrence and Shelton [16]) exhibits the phenomenon of *planar cell polarity* (Klein and Mlodzik [17]). In addition to cells being polarised in the apical-basal direction, in the sense that they have an asymmetric structure along the axis of polarity, the wing and notum cells also have a proximal-distal asymmetry. The asymmetry is established by the pattern of localisation of PCP proteins on cell junctions (Vinson and Adler [19], Saburi and McNeill [20]). A certain set of proteins is enriched only in the junctions parallel to the proximal-distal axis, and a complementary set of proteins is enriched in the junctions that are orthogonal to them (Amonlirdviman et al [18]).

Classen et al [8] report that cellular repacking and the establishment of planar polarity happens at the same time. Moreover, the planar polarity proteins are essential for the repacking of the wing epithelium from an irregular array into an ordered quasi-hexagonal array. They determine the orientation of the wing hairs [8].

Since the establishment of planar polarity grid in the tissue happens concomitantly with the repacking of the cells into an ordered array, the two are believed to be mechanically linked.

Another extensively studied system exhibiting planar cell polarity is the *Drosophila* germband during body axis elongation. The germband elongates in the process called *convergent extension*, which is thought to be driven by the polarised forces at cellular junctions (Zallen and Zallen [21], Rauzi et al [22], Bertet and Lecuit [23]).

Given that homologues of the planar polarity pathway exist in humans (Montcouquiol et al [24]), there is significant interest in understanding their effect on tissue organisation and patterning. In this context, a need arises for a comprehensive description of collective cellular mechanics in epithelia. In the following sections, a few recently proposed models are described.

1.3 Thesis overview

The thesis consists of five chapters. In this chapter, we introduce several unresolved questions concerning physical and geometric organisation of cells in planar epithelia and present an overview of existing models and theories.

Chapter 2 describes the computational model of epithelial cell physics (mechanics). The model assumes that junctions between cells experience a potential energy with a linear and a quadratic term in junction length, and it solves for equilibrium states, with a constraint on apical cell area. The dynamic evolution is implemented using Monte Carlo simulations. The model is applied to several cases of biological relevance: growing tissue and tissue of fixed size, with and without coordination in cell division timings.

Chapter 3 describes a study of cell delamination in epithelia. The conclusions of the study strongly suggest that there exists a previously unreported mechanism of compression-induced cell delamination, which is distinct from the widely studied apoptosis-induced delamination.

Chapter 4 describes a theoretical and a computational analysis of phase transitions in the epithelium caused by the change in physical parameters. In particular, the study suggests that junctional acto-myosin contractility can modulate cell repacking in a tissue, so as to drive it towards a regular hexagonal lattice.

In Chapter 5, a computational study of convergent-extension in *Drosophila* germband is presented. The findings indicate that polarisation in acto-myosin contractility can

cause the formation of rosette-like structures and actin-cables, which are reported to be observed *in vivo*.

1.4 An Overview of Computational Models of Epithelial Organisation

1.4.1 Lattice models: the cellular Potts' model

The *cellular Potts model*, or the *Glazier-Graner model* as it is also called, is an example of a computational 2D lattice model devised to study biological tissue. It was published in 1992 by Glazier and Graner [25] and it became the basis for a range of subsequent models. In this framework, the tissue is comprised of a set of generalised lattice cells, each cell defined by the *cell id* (in analogy to particle *spin number* in the Ising model). One lattice site per timestep is updated stochastically. The *Hamiltonian* captures the dynamics of the system because it is used to calculate the probability with which a lattice site changes at each timestep. Before describing the Hamiltonian in the Glazier-Graner model, I will briefly describe a simplified theory which is used in foam physics.[1]

Consider the Hamiltonian used in the large-Q Potts model:

$$H = \sum_{(i,j),(i',j') \text{ neighbours}} \left(1 - \delta_{\sigma(i,j),\sigma(i',j')}\right). \tag{1.1}$$

A collection of N cells is defined by the set of N degenerate spins $\sigma(i,j) = 1, ..., N$, where (i,j) is a lattice site. The cell σ contains all the lattice sites with spin σ. The Hamiltonian dictates that site-site interaction energy is 1 when two different cell spins are adjacent ($H = 1$ when spins $\sigma(i,j)$ and $\sigma(i',j')$ are different), and 0 when the same cell spin occupies the neighbouring sites ($H = 0$ when $\sigma(i,j) = \sigma(i',j')$). This Hamiltonian energetically punishes the length of the cell-cell interface. It therefore describes surface tension and it is used to model cohesive phenomena.

Time evolution is implemented as follows. At each time step, a cell lattice is chosen at random and its cell id is changed from σ to σ' with the Monte Carlo probability

[1] Historically, quantitative studies of biological tissue often built on studies of the physics of foams (Plateau [30], Taylor [31]), Weaire [32].

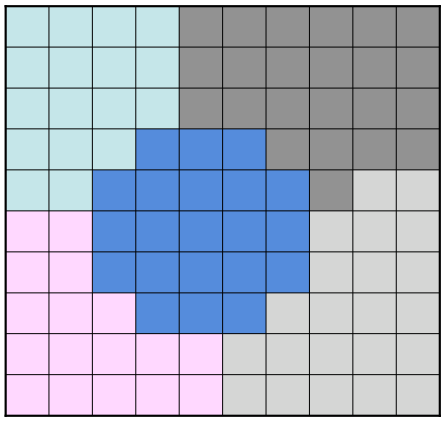

Figure 1.6: A collection of N=5 cells in the Potts model. Every lattice site (pixel) is allowed to assume any colour. A pixel with $\sigma = 1$ is green, $\sigma = 2$ is dark gray, $\sigma = 3$ is light gray, $\sigma = 4$ is blue and $\sigma = 5$ is pink. A collection of all green lattice sites (pixels) defines cell 1, etc.

(for temperature $T > 0$, and k the Boltzmann constant):

$$\begin{aligned} P_{\sigma\to\sigma'} &= \exp(-\Delta H\frac{k}{T})\,, \qquad \Delta H \ > 0 \\ &= 1, \qquad\qquad\qquad\quad \Delta H \ \leq 0. \end{aligned}$$

When $T = 0$, we have:

$$\begin{aligned} P_{\sigma\to\sigma'} &= 0, \qquad \Delta H > 0 \\ &= 0.5, \quad \Delta H = 0 \\ &= 1, \qquad \Delta H < 0. \end{aligned}$$

This model is good for the grain-growth of the soap-froth. However, it needs to be modified for biological applications. This is because biological cells have a volume constraint which limits their size, as opposed to soap bubbles which do not have such limitations.

The Hamiltonian in the original Glazier-Graner paper [25] is as follows:

$$\begin{aligned} H &= \sum_{(i,j),(i',j') \text{ neighbours}} J\left[\tau(\sigma(i,j)), \tau(\sigma(i'j'))\right]\left(1-\delta_{\sigma(i,j),\sigma(i',j')}\right) \\ &+ \lambda \sum_{\sigma \text{ id types}} (a(\sigma) - A_{\tau(\sigma)})^2 \theta(A_{\tau(\sigma)}). \end{aligned}$$

This is known as the *cellular Potts model* or the *Glazier-Graner model* and it became the basis for a range of subsequent models. Since some features of this model are similar to the model proposed in this project, it is described here in some detail.

τ is another 'spin number' which describes cell *type*. Let $\tau = \{l, d, M\}$, where l stands for 'light', d for 'dark' and m for 'medium'. So each lattice site has two quantum numbers, "τ" and "σ". There may be many cells of the same type τ, whereas σ is unique for each biological cell and consists of all lattice sites with cell id σ. $\tau(\sigma)$ is the type of cell σ. $J(\tau, \tau')$ is the surface-energy between cells of type τ and τ'.

The second term describes the elastic area constraint. $A_{\tau(\sigma)}$ is the target area for the cell of type τ. $\tau = M$ describes the medium where cells are kept (extra-cellular matrix, substrate, culture solution, etc). The target area of the medium is set to be negative. This is stabilised by multiplying the area term in the Hamiltonian by the Heaviside step function $\theta(x) = \{0 : x < 0;\ 1 : x > 0\}$. The tissue kept in mind for this simulation is the embryo with two types of cells: the mesoderm and the ectoderm (Steinberg [26]). Since these cell aggregates are compact, an additional requirement is imposed, so that a lattice site is allowed to flip only to the cell id of a neighbouring site. Therefore, nucleation of medium-filled sites is prevented since it is not observed in the embryo.

The described Hamiltonian minimises interface tension between neighbouring cells while constraining the size of the cells. The results of a simulation are shown in Figure 1.7. Light cells have high surface energy (low adhesion), and dark cells have low surface energy (high adhesion). The system moves to the configuration of minimum potential energy, and this results in a change in the relative positions of cells. Therefore, a mixed collection of light and dark cells sort into separate domains. Sorting behaviour is robust and it occurs over a wide range of parameters. This has become the standard way to model differential adhesion phenomena (Brodland [27], Steinberg [28]). More recently, however, it was shown that embryonal cell sorting is not purely driven by

differential adhesion, but also involves other processes such as cell cortex tension (Green [29]).

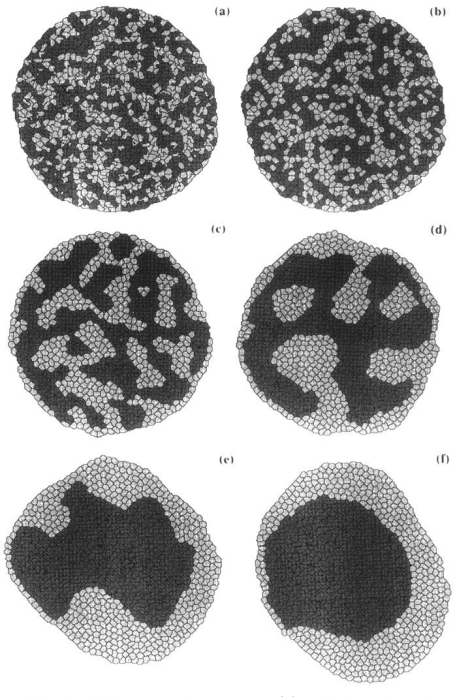

Figure 1.7: Glazier-Graner simulation
Cell sorting time series: (a) Initial configuration with randomly assigned cell types, (b) 1 MCS, (c) 100 MCS, (d) 1000 MCS, (e) 4000 MCS, (f) 10 000 MCS. Light cells have high surface energy (low adhesion), and dark cells have low surface energy (high adhesion); $J(d,d) = 2$, $J(d,l) = 11$, $J(l,l) = 14$, and $J(d,M) = J(l,M) = 16$.

Owing to its success in studying differential adhesion phenomena, the cellular Potts model was adjusted for use in multiple situations. In a recent paper, Käfer et al [6] study cell shapes in a *Drosophila* retinal ommatidium. The authors conclude that the ommatidium cell shapes cannot be accounted for by only taking adhesion-related surface tension into account, and their Hamiltonian includes an additional term of the form:

$$\sum_{\text{cells}} \gamma_P (P_i - P_{i0})^2,$$

where P_i is the perimeter of cell i, P_{i0} is the target perimeter of cell i and γ_P is the perimeter modulus.

This additional term quantifies the effect of cortical cytoskeleton in a cell. It

is usually described as cell contractility, and it features in most recent models of epithelial mechanics (Hufnagel et al [35], Farhadifar et al [36]). In [35], the contractile contribution to the Hamiltonian is proportional to cell perimeter, and in [36], its contribution is proportional to the square of cell perimeter. Cell contractility also prominently features in the model which we develop. However, we use junctional contractility rather than perimeter contractility.

1.4.2 Analytical models: Topology of an epithelial tissue

What exactly can we learn from revealing the details of apical topology of an epithelial sheet? Is there any adaptive advantage in having differing topologies? Is the tissue patterning and signalling robust under a change of topology? Or whether attaining a specific topology is essential for ensuring that the development of the tissue proceeds correctly? These are still largely open questions that will hopefully be tackled by understanding more about global tissue topology.

Furthermore, to what extent does tissue topology depend on genetic instruction? There is strong evidence that at certain points in development, a tissue switches on genetic regulation to induce a programmed morphogenetic change (such as the intercalation of cells during convergent extension in the germband). But at other times, there seems to be little regulation and the topology is determined by the stochastic averages over individual cell behaviour. There seems to be a default topological configuration of the tissue, which is the one when regulation is absent (Axelrod [37]). When the tissue wants to implement a specific change, genetic regulation is switched on and a large-scale transformation is induced by the local cell-cell interactions, driven by the polarised myosin, for example.

In order to understand this tissue behaviour, several research groups have proposed topological models of epithelial sheets (Rivier and Lissowski [38], Dubertet and Rivier [39], da Fontoura Costa et al [40]). The reasoning is as follows: If we can construct a good model of default tissue behaviour, then we are one step closer to understanding the details of tissue behaviour when it is regulated. And this may in turn feed back more insight into the limitations of strategies available to the tissue for implementing a specific large-scale transformation. In the last instant, understanding these mechanisms will help understand how topology and structure in general influence function, and eventually it will help with finding remedies for malformations.

The Markov Chain Model

Gibson et al [41] propose an interesting analytical model of epithelial topology based on the properties of convergent Markov chains. It is a very simple model, but it is instructive for understanding equilibrium properties of epithelial topology.

The model is based on a set of simple assumptions about individual cell behaviour. The aggregate behaviour is described by a Markov chain. Since the assumed cell behaviour results in a convergent Markov chain, the model predicts that the tissue should reach a stable configuration, described by a constant distribution of polygons in the plane. This model is elegant and instructive, but it assumes that no cell neighbour exchanges occur in the tissue. However, epithelial tissues undergoing cell divisions are topologically active, and neighbour exchanges occur throughout most of pupal development of the notum.

Therefore, this analysis finds stable configurations of tissue topology resulting solely from cell proliferation.

The assumptions are:

1. Cells are polygons with a minimum of 4 sides.
2. Cells do not exchange neighbours.
3. Mitotic siblings share a common junctional interface.
4. Cells have asynchronous, but roughly uniform cell cycle times.
5. Cleavage planes always cut a side, rather than a vertex of the mother polygon.
6. Mitotic cleavage orientation binomially distributes existing junctions to daughter cells.

In the notation of graph theory, v_t, e_t and f_t denote the number of vertices, egdes and faces after t divisions. The equations for their time evolution are as follows:

$$f_t = 2f_{t-1}. \tag{1.2}$$

This follows from the fact that after every round of division, every cells has divided once, and so the total number of faces doubles. And because each cell division results

in the creation of two new vertices and three new edges, we have:

$$v_t = v_{t-1} + 2f_{t-1} \tag{1.3}$$
$$e_t = e_{t-1} + 3f_{t-1}. \tag{1.4}$$

For large t, the boundary effects become negligible and the average number of sides per cells is:

$$s_t = 2 \times \frac{e_t}{f_t} = 2 \times \frac{e_{t-1} + 3f_{t-1}}{2f_{t-1}} = \frac{s_{t-1}}{2} + 3. \tag{1.5}$$

The solution of this recurrence relation is:

$$s_t = 6 + \frac{1}{2^t}(s_0 - 6), \tag{1.6}$$

where s_0 is the initial configuration of the network.

The lesson to take from this result is that the system will *on average* tend to a hexagonal topology without any minimal packing conditions, but solely as a consequence of cell proliferation and the requirement that all stable vertices are of order 3.

From this point, they formulate a model that gives predictions not just for the average distribution of edges per cell, but also for the relative frequency of different polygons in the tissue (as inspired by earlier work, Cowan and Morris [42]).

Let p_s be the frequency of s-sided polygons in the network. Then the state of the network after t divisions is described by the state vector:

$$\mathbf{p}^{(t)} = \begin{pmatrix} p_4 \\ p_5 \\ p_6 \\ p_7 \\ p_8 \\ \dots \end{pmatrix}$$

The dynamics is described by:

$$\mathbf{p}^{t+1} = \mathbf{p}^t PS, \tag{1.7}$$

where P and S transition matrices:

$$P = \begin{pmatrix} 1 & 0 & 0 & 0 & 0 & 0 \\ 1 & 1 & 0 & 0 & 0 & 0 \\ 1 & 2 & 1 & 0 & 0 & 0 \\ 1 & 3 & 3 & 1 & 0 & 0 \\ 1 & 4 & 6 & 4 & 1 & 0 \\ 1 & 5 & 10 & 10 & 5 & 1 \\ \dots & & & & & \end{pmatrix}$$

P_{ij} gives the (un-normalised) probability that an i-sided cell divides to become a j-sided cell. The entries in P_{ij} are the same as the entries of Pascal's triangle. This is the direct consequence of the division rule whereby the cleavage plane cuts a side of the mother cell so that the mother vertices are assigned to daughter with the binomial distribution.

As an example, consider a hexagonal cell which divides. Let us pick one of the daughter cells. It can have 4, 5 or 6 vertices (in any other case, a 3-vertex cell would arise, which is forbidden). The counting argument is as follows: in addition to the compulsory 4 vertices, the daughter can receive another 0 vertices in $\binom{2}{0}$ ways, another 1 vertex in $\binom{2}{1}$ ways or another 2 vertices in $\binom{2}{2}$ ways.

Note: This is not a very realistic biological scenario for the way vertices are distributed between the daughter cells. If the cleavage plane orientation is assumed to be uniformly distributed on $[0, 360]$ as the authors claim, the resulting distribution is not binomial.

S takes into account the fact that cells gain sides from neighbour divisions too, on average one new side per cell cycle.

$$S = \begin{pmatrix} 0 & 1 & 0 & 0 & 0 & 0 \\ 0 & 0 & 1 & 0 & 0 & 0 \\ 0 & 0 & 0 & 1 & 0 & 0 \\ 0 & 0 & 0 & 0 & 1 & 0 \\ 0 & 0 & 0 & 0 & 0 & 1 \\ \dots & & & & & \end{pmatrix}$$

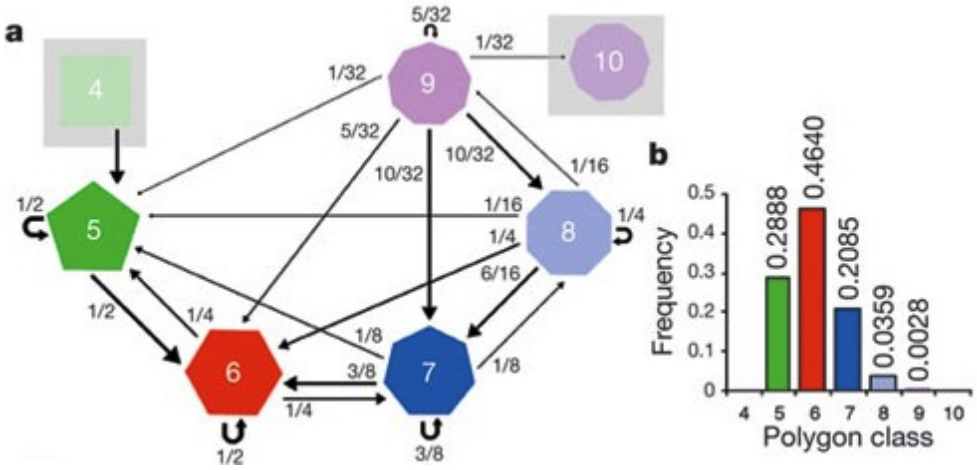

Figure 1.8: The Markov chain model of tissue topology. Adapted from Gibson et al [41].

Frobenius-Perrimon theorem ensures that this Markov chain reaches equilibrium irrespective of initial conditions. The exact equilibrium calculated from P and S is approximately: 28.9% pentagons, 46.4% hexagons, 20.8% heptagons and lesser frequencies of other types. This distribution is reached at an exponential rate. The model is summarised in Figure 1.8 (as illustrated in [41]).

Gibson at al report good agreement (Figure 3 in [41]) between the model predictions and the measurements in various epithelial tissues. However, the predicted distribution does not agree with other published *in vivo* tissue topologies (such as the experimental data from Farhadifar et al [36].) One of the main shortcomings of this model is that it does not take topological transitions into account: cells in the model do not exchange neighbours, and they do not die. However, since these processes happen throughout epithelial development, it is important to take them into account.

1.4.3 Vertex models

A step further from the purely topological models are the so called *vertex models* in which the vertex positions are dynamic variables responding to local mechanical forces. The vertex positions change in response to forces which arise from cell properties such as membrane elasticity, acto-myosin contractility, cell-cell adhesion, etc. Neighbour exchanges or *T1 transitions*, as they are also called, are a result of these forces (Figure 1.9). A second kind of topological change taken into account is cell death, or a *T2 transition* (Figure 1.10). Cell proliferation is also included, and it perturbs the model away from equilibrium. The rule for cell division is described in Figure 1.11.

Hufnagel et al [35] and Farhadifar et al [36] formulate a model of this type. Since the model in [36] is more similar to the model which we develop, it is described here in some detail.

In [36], the authors reason as follows:

> "The statistics of neighbor numbers in proliferating tissues were recently discussed by Gibson et al., who argued that the fraction of n sided polygons in the junctional network can be determined by simple topological rules describing allocation of neighbors after cell division. These topological rules are not based on the physical properties of the cells. However, we expect the redistribution of neighbors after cell division to depend on physical cellular properties. Also, a purely topological description cannot account for cell size and shape or local force balances."

The system contains N_C polygonal cells and N_V vertices. Stationary and stable network configurations satisfy a mechanical force balance; this implies that at each vertex, the total force F_i vanishes. These force balances as local minima of an energy function:

$$E(\mathbf{R}_i) = \sum_{\alpha} \frac{K_\alpha}{2}(A_\alpha - A_\alpha^{(0)})^2 + \sum_{<i,j>} \Lambda_{ij} l_{ij} + \sum_{\alpha} \frac{\Gamma_\alpha}{2} L_\alpha^2, \tag{1.8}$$

so that

$$\mathbf{F}_i = -\frac{\partial E}{\partial \mathbf{R}_i}. \tag{1.9}$$

The first term describes an area elasticity with elastic coefficients K_α, for which

A_α is the area of cell α and $A_\alpha^{(0)}$ is the preferred area, which is determined by the cell height and the cell volume. The second term describes line tension L_{ij} at the junction between cells i and j. Here, l_{ij} denotes the length of the junction linking vertices i and j and the sum over $< ij >$ is over all bonds. Line tensions can be reduced by increasing cell-cell adhesion or reducing acto-myosin contractility. The third term describes the contractility of cell perimeter L_α, quantified by a coefficient Γ_α, which reflects the mechanics of the acto-myosin ring, and it is the same term that is used by Käfer et al [6], as explained in Section 1.4.1.

The work function is minimised using the *conjugate gradient method* [43]. Conjugate gradients is a numerical method which finds a local minimum of the work function at every timestep. The tissue is thus relaxed into a local minimum at every timestep and cell divisions are what drives the system out of equilibrium. The division of a cell is implemented as follows (Figure 1.11): a cell is chosen at random and its target area is increased to twice its initial value in small steps (so that the deformation of the tissue is quasi-static), after which the cell is divided by a line of random orientation which passes through the midpoint of the cell. The daughter cells are assigned the initial target area. The timing of cell divisions is random.

In the simulations of tissue growth induced by cell division, the statistical properties of the cellular network converge to a *steady state*, which is determined by the values of the parameters K, A, Λ and Γ.

An important contribution of Farhadifar et al [36] is that it demonstrates that the described system exhibits a *phase transition* between two states: a regular hexagonal network and a disordered soft-network (Figure 1.12). The critical point is at $\frac{\Gamma}{\Lambda}\sqrt{A_0} = -0.13$.

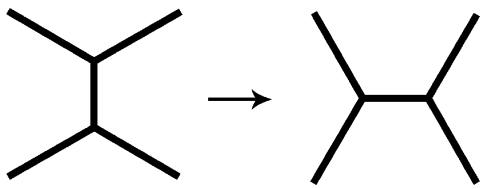

Figure 1.9: A diagram showing a neighbour exchange, or a T1 transition. Adapted from Farhadifar et al [36].

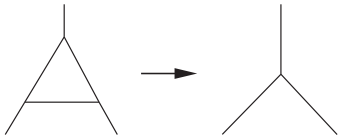

Figure 1.10: A diagram of cell death, or a T2 transition. Adapted from Farhadifar et al [36].

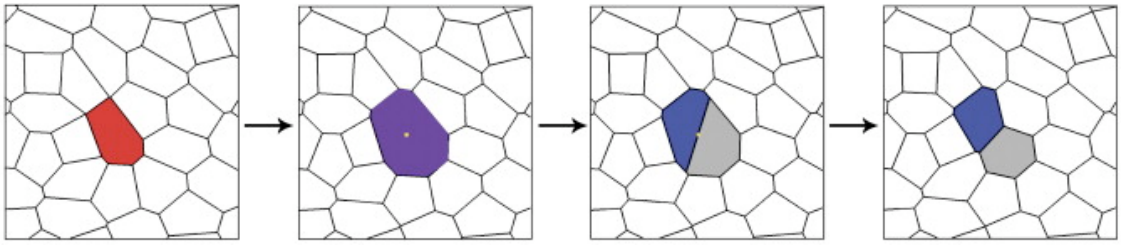

Figure 1.11: A diagram of cell division in the vertex model proposed by Farhadifar et al [36]. A cell is chosen at random, and its preferred area is increased. The orientation of the new edge which divides the cell is chosen at random. Daughter cells are assigned the initial preferred area. Adapted from Farhadifar et al [36].

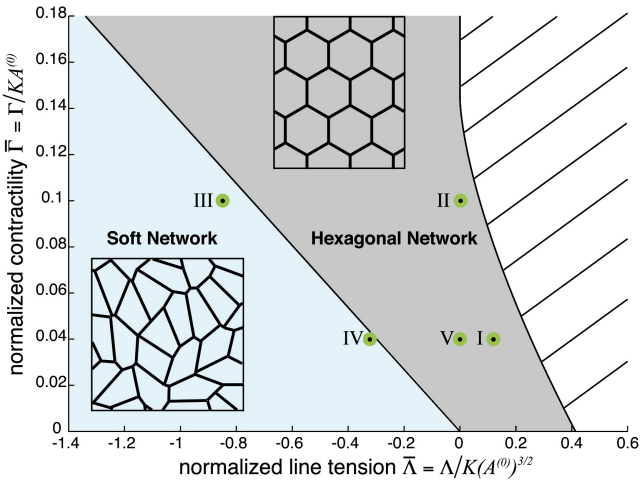

Figure 1.12: The ground state polygonal distribution undergoes a phase transition. Adapted from Farhadifar et al [36].

1.4.4 Idealised tissue with monodispersive cells

Hočevar and Ziherl [44] propose a simplified analytical approach to studying stable cellular network topologies. Their analysis is based exclusively on the neighbour exchanges and an energy function that describes the cell-cell interface. They describe equilibrium epithelial topologies that arise from the stochastic neighbour exchanges and do not take any cell division into account.

The cell shapes are determined by the minimisation of the energy function of a cell, in the aggregate. The total energy is proposed to be:

$$W = \left[\frac{\pi K}{R} - \frac{\Gamma}{2}(L - 2\pi R)\right] h, \tag{1.10}$$

where K is the bending constant for each cell, Γ the adhesion strength, h the cell height, L the cell perimeter and $R = \sqrt{K/\Gamma}$. From this expression, it follows that the cells with the same value of L have the same energy.

It is instructive to briefly analyse where the energy function comes from. All cells have the same height h which is constant. Cell polygonal bases and perimeters are also the same and constant (this is different from the other models considered in this report). The quantity which relates the polygonal base area and the polygon perimeter in the following way

$$a = \frac{4\pi A}{L^2} \tag{1.11}$$

is called the *reduced area* and it is a useful quantification of the inflatedness of the polygon. Since the bases and the perimeters are taken to be equal and constant, then the reduced area is also constant and equal for every cell. This is the so called monodispersive formulation of the model.

The bending energy of each cell is given by:

$$W_b = \left(\frac{Kh}{2}\right) \oint C^2(s) ds, \tag{1.12}$$

with K and h as before, $C(s)$ is the local curvature of the contour and the integral is along the contour defined by the edges of a cell, of length L. The adhesion energy

per cell is given by a similar expression:

$$W_a = \left(\frac{\Gamma h}{2}\right) \sum_i \int_{contact} ds_i. \tag{1.13}$$

Assuming that the contact sections are straight and the non-contact sections are circular arcs of radius $R = \sqrt{K/\Gamma}$. Combining equations (12) and (13) yields the total energy per cell in (10).

The dynamics of the model is based on **Monte Carlo-type** steps which involve a random edge length change or a neighbour exchange ($T1$ process). The book-keeping is done using a software package called the SURFACE EVOLVER, as explained in Brakke [45]. Following every step (length change or neighbour exchange), the system is relaxed so as to fulfil the area, perimeter and convexity requirements, and so every local transformation affects the system globally. After $3000 - 5000$ Monte Carlo steps the system reaches equilibrium and the polygon distribution remains constant.

The system exhibits two phases that correspond exactly to the phases in Farhadifar et al [36]. The disordered phase which is the equilibrium for $a < 0.785$, and the regular hexagonal ordered phase which is the equilibrium for $a > 0.865$. Equilibrium states for these two phases and for intermediate values of a are shown in Figure 1.13.

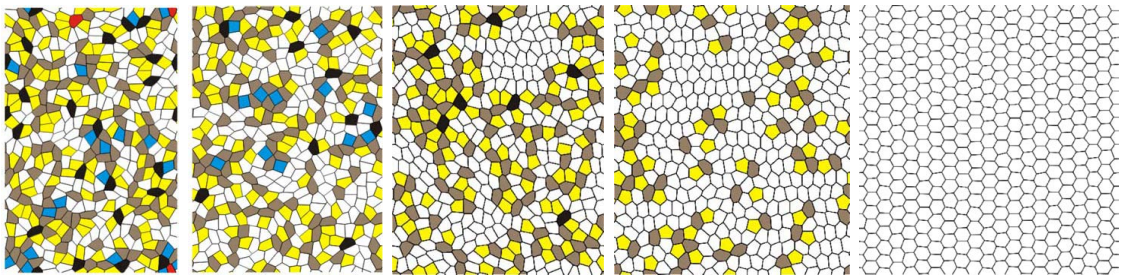

Figure 1.13: Equilibrium tilings for reduced areas given by $a = 0.74$, $a = 0.78$, $a = 0.82$, $a = 0.86$ and $a = 0.90$, respectively. Each polygon class is represented by a colour. At $a = 0.865$, the order-disorder transition takes place; for $a > 0.865$, all polygons in the tiling are regular hexagons. Adapted from Hočevar and Ziherl [44].

The simulations computationally predict the equilibrium distribution of the disordered phase. The disordered equilibrium state contains 5% four-sided, 26% five-sided, 40% six-sided, 23% seven-sided, 5% eight-sided and 1% nine-sided cells, with the error-bar less than 2%.

Hočevar and Ziherl conclude:

> "In our view, cell proliferation is of secondary importance for the structure of epithelia: the dynamics associated with cell division merely provides a way to sample the possible states of the tissue which, if unbiased, leads to entropy-maximising configuration."

The limitation of this approach lies in the fact that living tissue does not necessarily assume the entropy-maximising state. Entropy in this context is not the molecular thermal entropy, it is the entropy associated with the idealised mesoscopic system in which cellular junctions are fundamental units (Edwards and Oakeshott [46], Blumenfield and Edwards [47], Blumenfield and Edwards [48]). Ideal gases in thermodynamics assume the entropy-maximising configuration. However, living tissue is very different from an ideal gas. In this sense, tissue is more similar to a glass, since it can permanently exist in a local minimum of the potential energy.

1.5 A stochastic vertex model

In this context, we develop a physical computational model which attempts to reconcile the described opposing arguments concerning the choice of assumptions used to explain equilibrium tissue topology. In this respect, our model resembles those put forward by Hufnagel et al [35] and Farhadifar et al [36] as it includes both cell proliferation and neighbour exchanges. However, there is one important distinction. The models described in [35] and in [36] are deterministic, in a sense that time evolution is implemented using the conjugate gradient algorithm. This means that the work function of the system is minimised at each step, which results in the tissue reaching the nearest local equilibrium, and not necessarily the global work function minimum. Therefore, the initial condition and the precise path of tissue evolution (the precise sequence of division events) determine the eventual configuration. This would correctly describe the dynamics of the tissue if there was no *noise* present in it.

If there is noise present in the tissue, it could induce tissue rearrangements which are not necessarily minimising the work function at every timestep. Noise thus helps the tissue sample alternative relaxation paths and this partially offsets the dependance of the steady state on the precise sequence of division events.

In thermodynamics, a system with thermal noise finds equilibria by minimising the *free energy*, while in the deterministic system (equivalent to zero temperature), the equilibria are found by minimising the *potential energy*. This is the distinction between the described vertex models ([35], [36]) and the model formulated in this thesis. We include noise in the system and thus we find equilibria which minimise the mechanical analogue of free energy. We choose noise with the white spectrum, and so it is mathematically identical to thermal noise. Origin of the noise is not thermal however, it is due to stochasticity of active molecular processes.

It is instructive to look at the limiting cases when noise is very low and when it is very high in our model. For the low value of noise, our model resembles the time evolution presented in the conjugate gradient models ([35], [36]) since in this case the system minimises the work function at every timestep. For the high value of noise, the entropic contribution to the free energy dominates the work function contribution. Therefore, at high noise, the system maximises the entropy.

Finally, junctions of epithelial cells incorporate molecules which are subject to stochastic behaviour. It is reasonable to expect that the intrinsic stochasticity of the cellular medium translates into fluctuations of the mechanical parameters such as membrane tension, acto-myosin contractility, cell volume etc. Therefore, including noise in the mechanical description of the cellular junctional network is justified. Since we do not have information about the spectrum of the noise, we make the simplest assumption that it is not time-correlated. Interestingly, as explained in Chapters 2 and 5, we find that noise can be an essential ingredient in the toolkit utilised by the self-organising tissue.

Chapter 2

A Model of Tissue Mechanics

2.1 Introduction

Many morphogenetic processes require tissues to dramatically change shape, as they do during gastrulation, neurulation and organogenesis. All these changes occur as a result of coordinated changes in cell shape and so understanding cell shape changes is central for the understanding of development. Moreover, cell shape is important for the correct proceeding of cell division, where mitotic rounding is understood to help organisation within cells (Martin et al [49]). Despite the central importance of the processes driving cell shape changes, the details of their cell biology and the corresponding mechanical description are still not understood in a satisfactory way.

In order to study the mechanical forces in epithelia, and how they couple with various developmental processes in the tissue, we develop a simple mechanical model of epithelial tissues. One should stress that there is no such thing as the correct model, we judge the model only by how useful it is. Among significant criteria which determine the model's usefulness is the requirement that the model parameters are related to the measurable biological parameters. It is also important that model predictions are directly testable experimentally. Models based on the cellular Potts' model have proved successful in aiding our understanding of tissue growth and growth control (Hufnagel et al [35], Farhadifar et al [36], Shraiman [50]), in the understanding of tissue patterning (Käfer et al [6]), as well as the coupling of mechanical stress and biochemical signalling such as the coupling of Dpp morphogen and cell proliferation (Wartlick et al [51]) in *Drosophila* development. Vertex models are inspired by the concept of minimisation of energy used in the cellular Potts' model, however they are

distinct from the original model proposed by Glazier and Graner (Glazier and Graner [25], Merks and Glazier [33], Glazier and Graner [34]) because rather than being lattice models, they take into account the precise positions of cell-cell boundaries. The dynamic variables in the vertex models are the positions of the vertices.

2.2 The apical tissue surface is represented by a polygonal network

We design and implement a variant of the existing vertex models. Its role is to capture key features of the effects of mechanical force, through simplifying the epithelial cellular network and describing it by several mechanical and geometric parameters. There are several distinctions between our model and the existing ones, and these will be highlighted and discussed in due course.

The apical epithelial network is modelled by a two-dimensional network of planar polygons, where a cell's apical surface is demarcated by the vertices and the junctions which it shares with its nearest neighbours, as seen in Figure 2.1. The third dimension is the height of the epithelium and it is not explicitly included in the model. Therefore, the apical surface of a cell is approximated by a polygon and we are concerned with modeling a polygonal tiling. A polygonal tiling is an example of a 2d graph and so we are concerned with a study of random 2d graphs, with certain constraints that reflect realistic tissue configurations.

The dynamic variables are the positions of the vertices of the polygons. As the vertex positions change, so do the cells' size, shape and relative positions. Vertices are labelled by letters (i,j,...). Cell-cell junctions are labelled by its vertices (ij,kl,...), and the cells are labelled by Greek letters (α, β,...). Junction length is labelled by l_{ij}, and cell area is A_α.

2.3 Mechanical forces

Epithelial cells exist in a crowded and dynamic environment, and they are subject to mechanical forces caused by various intercellular processes and the environment. These forces arise from: the properties of the cell membrane, the activity of the cytoskeleton, fluid flow within and outside of the cells and compressive stress from

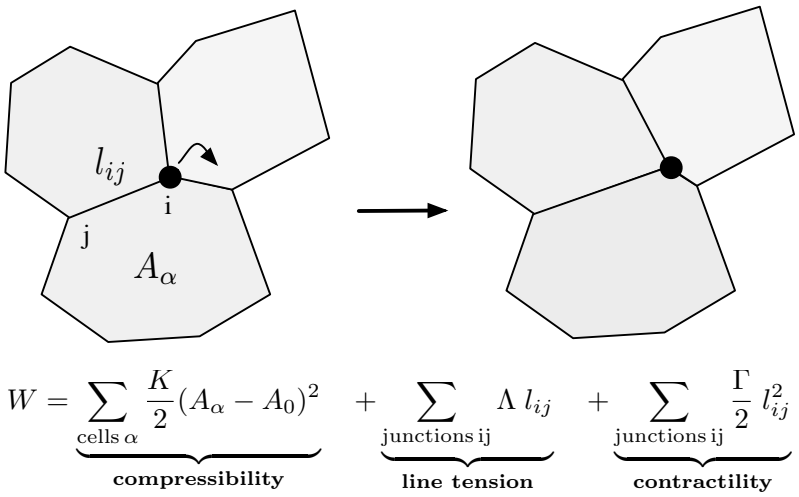

Figure 2.1: Tissue evolves through displacements of the vertices.

the neighbouring cells. There are also external sources of mechanical compression induced by other tissues. Finally, active processes such as cell division and cell death exert a mechanical force. It would be very difficult to try to model the mechanics of a tissue by including a long list of possible forces, and even if it was done, it would be very difficult to measure the values of the parameters which describe these individual forces in the model. Therefore, the force term used in all the different versions of the cellular Potts' model includes only a few terms.

The dominant mechanical forces in epithelial tissues are thought to arise from:

1. mechanical properties of the cell cytoskeleton, such as acto-myosin contractility,
2. elastic properties of the cell membrane,
3. tension of the cell membrane due to the composition of the surrounding fluid and the constituent molecules of the membrane,
4. adhesive properties of cell-cell contacts, and
5. limited compressibility of cell volume.

Taking these factors into account, it is possible to write a *work function* which

determines the dynamics of the system:

$$W = \sum_{\alpha} \frac{K}{2}(A_\alpha - A_0)^2 + \sum_{ij} \Lambda_{ij} l_{ij} + \sum_{ij} \frac{\Gamma_{ij}}{2} l_{ij}^2. \tag{2.1}$$

The gradient of this function describes the instantaneous forces in the system $F(\mathbf{r}) = -\frac{dW}{d\mathbf{r}}$. Therefore, the system will move towards the state where W has a minimum, either a local or a global one.

The coefficients multiplying the geometric quantities are physical parameters that need to be fitted to the experimental values in live tissues. The first term is summed over all the cells α : $\frac{K}{2}(A_\alpha - A_0)^2$ represents **cell area elasticity**; A_α is the area of cell α, A_0 is its preferred area and K is the area elasticity coefficient. The preferred area captures the idea that there is a balance between the forces of outside compression on a cell (by its neighbours), and the limited compressibility of the cell's volume. Therefore, force balance is established at some equilibrium value of cell area A_0. In the simplest version of this model, we assume that all cells have the same preferred area, although this condition can be readily relaxed ($A_0 \to A_\alpha^{(0)}$), for example in order to study daughter cells with a smaller preferred area than that of the parent cells.

The second and the third term are summed over all the junctions ij. $\Lambda_{ij} l_{ij}$ represents **line tension** of junction ij due to cell-cell adhesion and cell membrane tension.

Actin filaments and myosin motors localise at the cell's cortical domain and so they exert force along the junctions. $\frac{\Gamma_{ij}}{2} l_{ij}^2$ represents **junctional contractility**. Rearranging 2.1 yields:

$$\begin{aligned} W &= \sum_{\alpha} \frac{K}{2}(A_\alpha - A_0)^2 + \sum_{ij} (\Lambda_{ij} l_{ij} + \frac{\Gamma_{ij}}{2} l_{ij}^2) \\ &= \sum_{\alpha} \frac{K}{2}(A_\alpha - A_0)^2 + \sum_{ij} \frac{\Gamma_{ij}}{2}(l_{ij} - l_{ij}^{(0)})^2 - \frac{\Lambda_{ij}^2}{2\Gamma_{ij}}, \end{aligned}$$

with

$$l_{ij}^{(0)} = \frac{-\Lambda_{ij}}{\Gamma_{ij}}.$$

If mechanical parameters are isotropic ($\Lambda_{ij} = \Lambda, \Gamma_{ij} = \Gamma$, $\forall i, j$), then $-\frac{\Lambda_{ij}^2}{2\Gamma_{ij}} = -\frac{\Lambda^2}{2\Gamma}$

is constant at every timestep. Since the dynamics does not depend on the absolute value of the work function, but only on differences $\Delta W = W_2 - W_1$, the constant term $-\frac{\Lambda_{ij}^2}{2\Gamma_{ij}}$ is irrelevant in this case, and the work function is equivalent to:

$$W = \sum_{\alpha} \frac{K}{2}(A_\alpha - A_0)^2 + \sum_{ij} \frac{\Gamma_{ij}}{2}(l_{ij} - l_{ij}^{(0)})^2.$$

Written in this form, the work function yields to an alternative physical interpretation. It favours those polygons which have the area closest to the **target area** A_0 and the lengths of its junctions closest to the **target junction lengths** $l_{ij}^{(0)}$. In isotropic cases (e.g. such as in the absence of planar polarisation in the tissue where the values of Λ_{ij} and Γ_{ij} depend on the orientation of the junction ij) we assume that contractility and junction line tension are the same for all junctions, and therefore $\Lambda_{ij} = \Lambda$, $\Gamma_{ij} = \Gamma$, and $l_{ij}^{(0)} = l_0$. These tissues are expected to have cells with the same values of target junction length l_0, and the work function simplifies to

$$W = \sum_{\alpha} \frac{K}{2}(A_\alpha - A_0)^2 + \sum_{ij} \frac{\Gamma_{ij}}{2}(l_{ij} - l_0)^2.$$

This is the expression which is used in the remainder of this Chapter and in Chapters 3 and 4.

Finally, it is of course possible to have a positive value of cell line tension Λ, so that the value of target junction length l_0 is negative. The adhesive contribution to Λ has to be small for this to happen. In these circumstances, cell junctions are trying to constrict no matter how short they are.

2.4 The energy phase-space

An interesting quantity to consider here is $a = 4\pi\frac{A_0}{L^2}$, the so called target *reduced area* of the cell, where L is the cell perimeter. It is a geometric quantity that describes how much junctional length is needed to enclose a given area by a 2D shape. The more efficient the packing, the less junctional material is used for a given area, and the greater the value of a. Therefore, a quantifies how far a given polygon is from the most efficient polygon in terms of rationing the junctional material. So, for a

circle which is the most efficient isolated geometric shape in this sense, $a_{circle} = 1$. The most efficient polygon in a polygonal tiling is a regular hexagon, and it has the value $a_6 = 0.907$ ($A = \frac{3\sqrt{3}}{2}l^2$, $L = 6l$ for the regular hexagonal polygon with junction length l). Other polygonal shapes have lower values of a.

Hočevar and Ziherl [44] study the so-called monodispersive polygonal tilings, in which every polygon has the same value of a, as well as the same area and perimeter. This is clearly an idealisation of the realistic biological tissue in which the values of cell areas and cell perimeters are not *all* the same. However, it is a useful first approximation. They find that if we consider a set of these simple polygonal tilings, such that each tiling in the set has a different value of a, there is a **phase transition** at the critical value $a_c = 0.865$. In Figure 1.13, we see several such tilings. Their finding is based on a numerical search. More on the geometric arguments concerning the relationship between a and the bulk properties of the polygonal tiling can be found in Chapter 4.

Equally, Farhadifar et al [36] find that there is a phase transition in the 2D phase-space determined by the parameters of the work function. The corresponding phase-space in our model is shown in Figure 2.2.

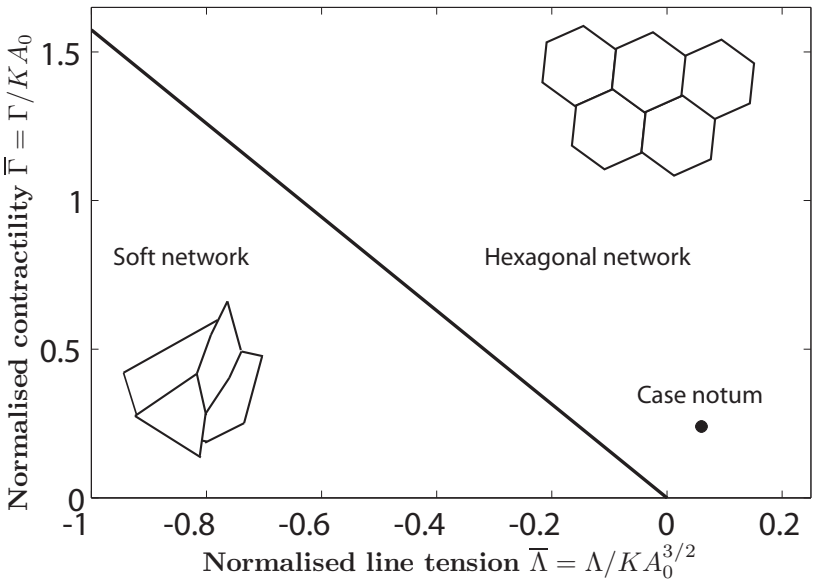

Figure 2.2: Phase space for our model.

The line which divides the two phases corresponds to $a_c = 0.86$. To show this, consider its slope s:

$$s = \frac{\Gamma}{KA_0} \times \left(\frac{\Lambda}{KA_0^{3/2}} \right)^{-1} = \frac{\Gamma}{\Lambda}\sqrt{A_0} = \frac{-1}{l_0}\sqrt{A_0}.$$

Squaring this yields

$$s^2 = \frac{1}{l_0^2}A_0.$$

Remembering that $l_0 = \frac{L_0}{6}$ where L_0 is the perimeter of a hexagonal cell with sides l_0, and that $a = 4\pi\frac{A_0}{L_0^2}$, we get

$$\begin{aligned} s^2 &= \frac{36}{L_0^2}A_0 \\ 4\pi s^2 = 36 \quad &\times \quad 4\pi\frac{A_0}{L_0^2} = 36a_c. \end{aligned}$$

Therefore

$$s = \pm\sqrt{\frac{36 \times 0.86}{4\pi}} = \pm 1.57.$$

The difference between the phase space in Figure 2.2 and the phase space in [36] arises because the contractile term in [36] is the **perimeter contractility** $\frac{\Gamma}{2}L_\alpha^2$, whereas in our model we use the **junction contractility** $\frac{\Gamma}{2}l_{ij}^2$. When perimeter contractility is used, the slope of the line that divides the two phases is $s = -0.13$. It can be verified that the two slopes are equivalent if one takes into account that $L_0 = 6l_0$ and $L_0 = \frac{-\Lambda}{2\Gamma}$ in [36], and therefore the predictions of our model and those in [44] and in [36] are mutually consistent.

2.5 The principle of free energy minimisation applied to the polygonal network

One of the key insights required for modeling biological systems is that equilibrium models can be used for non-equilibrium problems, under the condition that some processes happen a lot faster than others. We make use of this by noting that there are "fast" and "slow" processes in the epithelium. When a cellular junction is laser ablated, its mechanical response to the change in tension is fast. Equally, the mechanical response of the junction which experiences external pulling is fast, as is the elastic response of cell area. Therefore, if a cell is subjected to external compression, it will respond quickly. On the other hand, the process of cell division is slow. In reality, the duration of mechanical readjustment of a junction following a laser cut is several seconds. The duration of cell division is a lot longer, of the order of one hour.

Therefore, it is useful to study mechanical equilibrium states of the epithelial network, even though the epithelium is an example of the system out of equilibrium in which a vast number of active processes are occurring at any given time. We assume that processes that affect the mechanical properties of the epithelial network are fast enough to justify the assumption that the system is equilibrated from the point of view of a slow process such as cell division. However, there is certainly a fair amount of **noise** in the epithelial sheet, and perhaps there is enough of it to be capable of disrupting the state of mechanical equilibrium on non-negligible timescales. Noise here is to be understood as the aggregate stochasticity of the system, resulting from the interconnections between a vast number of processes occurring in a crowded environment, and ultimately caused by the thermal noise of the constituent molecules.

In this situation, two sorts of effects are important: those arising from finding the minimum of the mechanical potential energy, as well as those to do with the uncertainty and randomness in the exact positions of the vertices due to the compounded noise. We capture this by using Monte Carlo sampling to determine the likely evolution of the system. Since we introduce noise, entropic effects become important. In such a system, equilibrium states result from a competition between energetic and entropic effects, and instead of minimising the potential energy of the system, we minimise its **free energy**.

The limiting case when the noise goes to zero results in the equilibrium state being determined only by the mechanical potential energy and the entropy is zero. On the other hand, when the noise is very high, the entropic term dominates in determining the equilibrium state.

2.6 Monte Carlo sampling

The mean value of a thermodynamic variable $\langle x \rangle$ is equal to the weighted sum over all available states s :

$$\langle X \rangle = \frac{\sum_s X_s e^{-\beta E_s}}{\sum_s e^{-\beta E_s}}. \tag{2.2}$$

E_s is the energy of the system in state s, X_s is the value of the thermodynamic variable in state s and β is a free parameter (in statistical mechanics β is inverse temperature). The denominator $\sum_s e^{-\beta E_s}$ is also called the partition function.

It is possible to generate a Markov chain of configurations with the property that $\overline{X}_n$, the average of X over n successive states, converges to the thermodynamic average:

$$\overline{X}_n = \langle X \rangle + O(n^{-1/2}). \tag{2.3}$$

So, if we generate an appropriate Markov chain and evolve it through a sufficient number of successive states, we can approximate the thermodynamic value of the variable. This is also a computationally practical way of finding the thermodynamic equilibrium of a system. In equilibrium, the probability of the system occupying state E is weighted by the Boltzmann factor $e^{-\beta E}$. This set of methods is called **Monte Carlo** sampling. It is designed to give a thermodynamic mean of a variable, from a knowledge of the energy. The noise which we use is not thermal, and we distinguish between a work function and a thermodynamic energy.

Computationally, we construct the Markov chain by using the **Metropolis sampling algorithm** which is a choice often used in Monte Carlo simulations.

We generate the Markov chain of states $\{s_1, s_2, ...\}$ as follows:

$$P(s_i \to s_{i+1}) = 1, \quad \text{if } W_{i+1} \leq W_i, \tag{2.4}$$

$$= e^{-(W_{i+1}-W_i)}, \text{ if } W_{i+1} > W_i. \tag{2.5}$$

This Markov chain converges to the state of *dynamic equilibrium*. When in equilibrium, the probability of the system occupying state s is e^{-W_s}. Depending on how W is normalised, the system can be more or less likely to depart from the the state of minimal W. The departure from the minimum value of W is allowed is due to the thermodynamic noise.

It is also important to stress that the successive states of the Markov chain generated above are correlated. Therefore, it may take a large set of states to find the equilibrium state. Moreover, the work function W may have many local minima. When perturbed, the system will relax into one of them. Because the landscape of the work function W may be very complicated, it is possible to reach a type of dynamic equilibrium which describes a local minimum of the work function, if the noise is not large enough for the system to eventually escape from the local minimum towards the global ground state.

The dynamic variables (or the *microstates*) are the positions of cell vertices. As the vertex positions change, so do the cell size, shape and position in the tissue change. The computational step which evolves the system through the states $\{s_i\}$ is implemented as follows. Choose a vertex at random, move it through a small displacement $\boldsymbol{\delta} = (\delta_x, \delta_y)$ and calculate the change in the work-function, ΔW, of the entire tissue. If $\Delta W < 0$, accept the move; if $\Delta W > 0$, accept the move with probability $\exp(-\Delta W)$. Moreover, δ_x and δ_y are not constant, but they are independent uniformly distributed random variables on the interval $[0, \delta_{max}]$, where δ_{max} is a free parameter. Moves that lead to polygons not being simply connected are rejected.

Since there is a non-zero probability that the system will occupy state s for which the energy is not the minimum energy of the system, the system is stochastic at short timescales. It is reasonable to assume that tissue parameter values do not remain constant over a period of tens of hours of development, but rather fluctuate at a very *short time scale* compared to the time scale for physiological processes and this is a result of internal cell dynamics. We do not attempt to mimic the precise movements of cell junctions over short timescales. This would require additional work in quantifying and characterising fluctuations in junction lengths at these short time intervals. We assume that the fluctuations are such that the resulting work function is weighted with the Gibbs measure. This is a common choice of measure in physical systems, since it is the unique measure which maximises the entropy for a given expected energy.

It is possible to study the effect of noise in other ways. One option is to introduce fluctuations in parameter values as is seen in the section on annealing in Farhadifar et al [36]. The authors randomly vary $\Lambda_{ij} = \Lambda(1 \pm \mu)$ at randomly selected junctions $< ij >$, where μ is the noise strength.

2.7 Topological changes: T1 and T2

As the tissue evolves, cells can exchange neighbors through a process known as the **T1 transition**. We implement the following procedure, illustrated in Figures 2.3: At every simulation step, we monitor the tissue for junctions shorter than a given threshold value; if a short junction exists, we attempt a vertex move that reduces the junction length to zero, using the same acceptance rule as above, and exchange cell neighbors. Since we allow 4-vertices to form, the T1 transitions are fully reversible (i.e. a junction can shrink to a 4-vertex and resolve back to its initial state). As T1 transitions occur in developing epithelia even in the absence of cell divisions, and some of the 4-vertices resolve back to their original state, modeling T1 transitions as reversible processes may potentially have important consequences. Confocal micrographs in Figure 2.4 show a T1 transition in live tissue, indicating the typical timescale of 20 minutes.

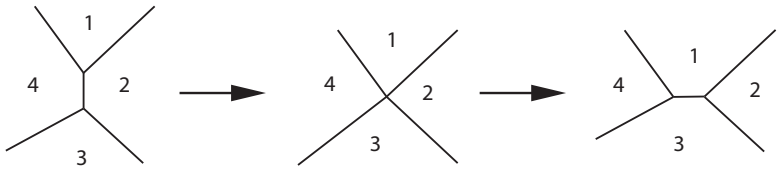

Figure 2.3: A neighbour exchange or a T1 process

So in the vertex model in the previous section, the system converges to a *steady state*, and in this model the network converges to a *dynamic equilibrium*, as expected from a stochastic dynamical system with Boltzmannian noise. It is worth pausing to clarify the terms in this context. A system is in a steady state if the composition of the system is unchanging in time. A system is in a dynamic equilibrium if the rate of every 'forward reaction' is equal to the rate of its 'backward reaction', and there is no actual transport of energy. One 'reaction' in the context of our model is the T1 transition. Forward and backward directions can be suitably defined. There is

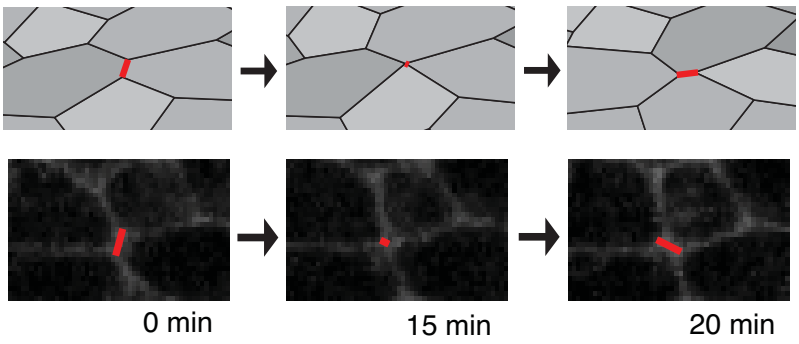

Figure 2.4: A neighbour exchange or a T1 process

some evidence that T1 transitions occur throughout the tissue even in the absence of cell divisions, which is consistent with assuming that T1 transitions can be caused by local fluctuations.

A second kind of topological change - an irreversible **T2 transition** - can occur when a cell is extruded from the tissue. As illustrated in Figure 2.5, we model this by removing any cell that has only 3 junctions and whose apical area is smaller than the threshold value, typically 1/4 of initial cell target area A_0, thus cell death or cell extrusion occurs when a cell becomes small. The stills from the simulation showing a T2 process are shown in Figure 2.6.

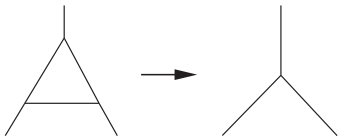

Figure 2.5: Cell delamination or a T2 process

The tissue patch has **continuous boundary conditions** and so its topology is toroidal. Care is taken that the sheet is sufficiently large so that spatial auto-correlation between cells is negligible. We normally work with sheets which are at least 10 cells across.

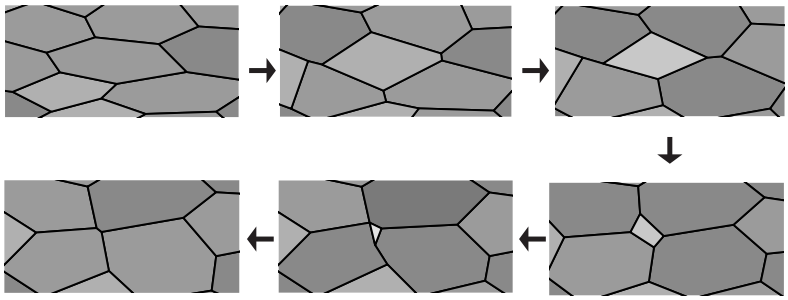

Figure 2.6: Cell delamination or a T2 process

2.8 Cell divisions

Cell division is externally introduced and it perturbs the system away from equilibrium. The rule which decides whether a given cell will divide at a given timestep can be modified by the user, and we study two different cases, as will be explained later. Once a cell is chosen, one of its edges is chosen uniformly at random. The midpoint of this edge is connected with the midpoint of the opposite edge. This introduces three new edges, one new cell and two new vertices in the system. If the mother cell has an even number of edges (n_c is even), the opposite edge is defined by $n_c/2$ edges counter-clockwise away from the given edge. If the cell has an odd number of edges, the opposite edge is defined by $(n_c \pm 1)/2$ (either being chosen with probability 1/2) edges counter-clockwise away from the given edge.

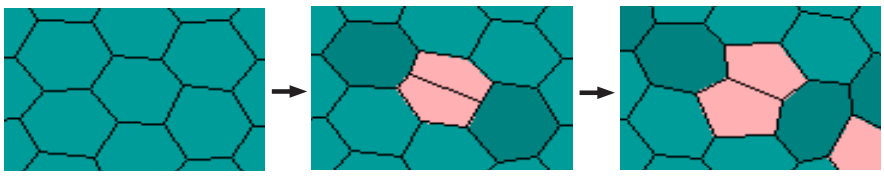

Figure 2.7: Cell division rule

2.9 Homeostasis for growing tissues and for tissues of fixed size

To characterise the model further, we study its equilibrium states. The initial condition is a regular hexagonal network and cell division is introduced to perturb the system away from equilibrium. The daughter cell target area is set to be equal to the mother target cell area. The values of the parameters used are shown in Table 2.1.

Table 2.1: Parameters values

A_0	1.30
K	160
Λ	56.8
Γ	49.9

These values correspond to realistic biological configurations, as studied by Farhadifar et al [36]. The tissue evolves through several rounds of cell divisions. Four different cases are compared, each corresponding to a possible biological realisation.

2.9.1 Tissue of finite size with co-ordinated cell divisions

An example of a developing tissue of finite size is the Drosophila notum during the pupal stages. The total tissue size and shape do not change, however, there are cell divisions and neighbour rearrangements, and the total number of cells increases. We model this situation by simulating a tissue of fixed size with ongoing cell division and observe the resulting tissue behaviour. Cell division times in the notum are coordinated, so that all cells divide within a given time interval after which the division process halts for several hours before the onset of the next round of cell divisions. Thus, cell division times can be modelled by the **gamma distribution**, so that the probability of division of cell i at age t_i has the following probability density function:

$$f(t_i) = t_i^{n-1} e^{-\lambda t_i} \lambda^{t_i} / (n-1)!,$$

where t_i is the age of the cell i, and n determines the length of a division round. In the simulations shown in Figure 2.8, $n = 101$. λ determines the time between two successive division rounds, $\lambda = t_{gen}$, with $t_{gen} = 6000$.

The external input of energy via cell divisions is eventually counterbalanced by the internal response of the system which irreversibly loses energy through the T2 transitions. Hence, the total number of cells eventually reaches a dynamic equilibrium, as shown in Figure 2.9, Panel 2. This is a natural way to generate configuration states to use as initial conditions when studying realistic biological configurations.

The polygon distribution also reaches a state of dynamic equilibrium after about 20 000 timesteps, as shown in Figure 2.9, Panel 5. The equilibrium distribution of polygon types depends both on the precise rule of cell division and on on the values of the parameters n and λ, and it is shown in Panel 1, Figure 2.17.

The number of T1 and T2 transitions reaches a periodic pattern after the first 3 division rounds (Figure 2.9, Panel 3 and 4). The number of transitions peaks during the time period in which cells divide, and it decreases when the divisions stop.

2.9.2 Tissue of finite size with a uniform rate of cell division

To test whether the co-ordination of cell division has a large effect on equilibrium properties, we change the timing of cell divisions. Here, cell division rate is uniform. The probability that a cell divides at each timestep is the same and equal to $P = 1/t_{gen}$. That is to say, consecutive cell division events are modelled as a Poisson process. This results in the division events being **exponentially distributed**, so that the probability that cell i has divided by reaching age t_i has the following probability density function:

$$f(t_i) = e^{-\lambda t_i}\lambda.$$

Stills showing tissue evolution for $\lambda = 1/t_{gen} = 1/6000$ are shown in Figure 2.10. In this case, too, the total number of cells reaches an equilibrium as shown in Figure 2.11, Panel 2. Since the size of the tissue is constrained, this also means that the average area available to a cell reaches an equilibrium value (Figure 2.11, Panel 6). The polygon distribution too reaches a volatile dynamic equilibrium (Figure 2.11, Panel 5 and Figure 2.17, Panel 2). The rates of T1 and T2 transitions (Figure 2.11, Panel 3 and 4) also equilibrate. Comparing the T1 and T2 rates to the case of co-ordinated cell division, it is apparent that the periodic trend observed in the previous section is now largely lost, as is expected when switching from co-ordinated to uniform division.

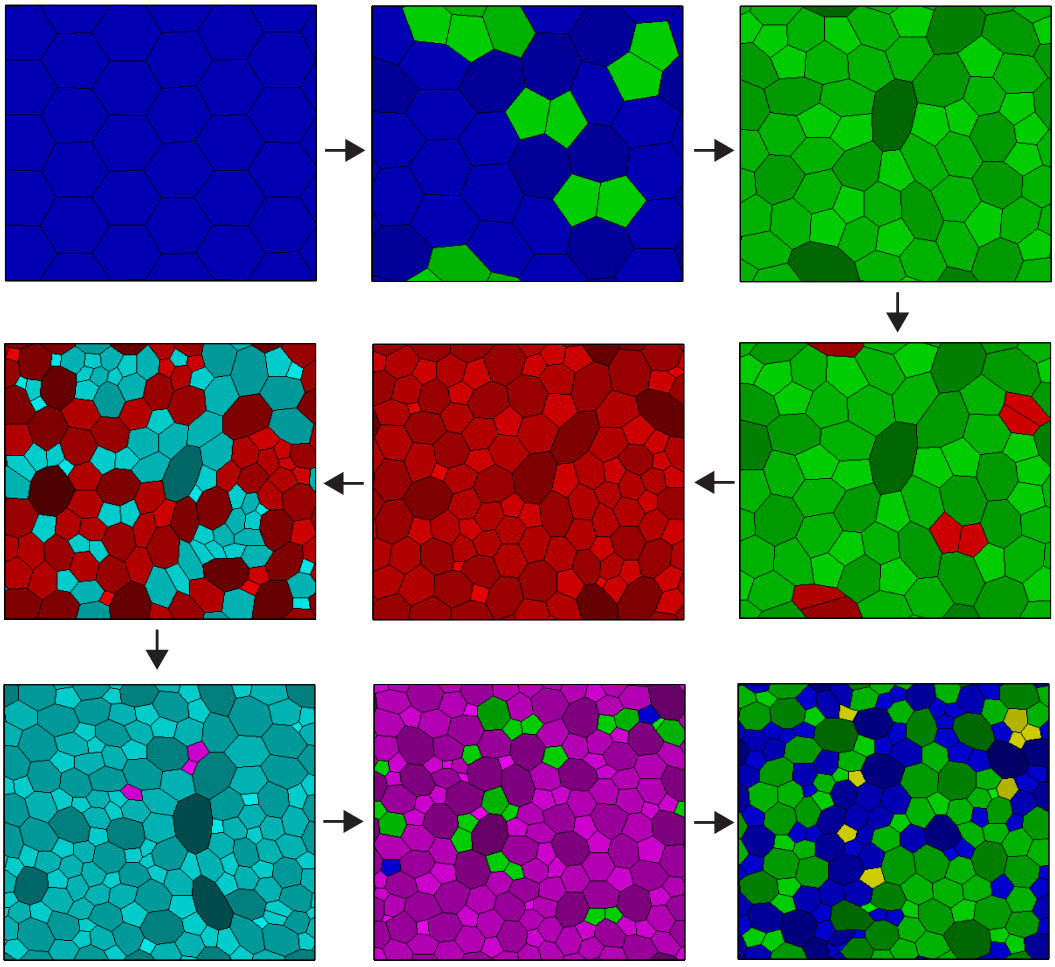

Figure 2.8: Stills showing evolution of tissue of fixed size with co-ordinated cell divisions. Colour coding: Blue - generation 1; Green - generation 2; Red - generation 3; Turquoise - generation 4; Magenta - generation 5; Green - generation 6; Blue - generation 7; Yellow - generation 8.

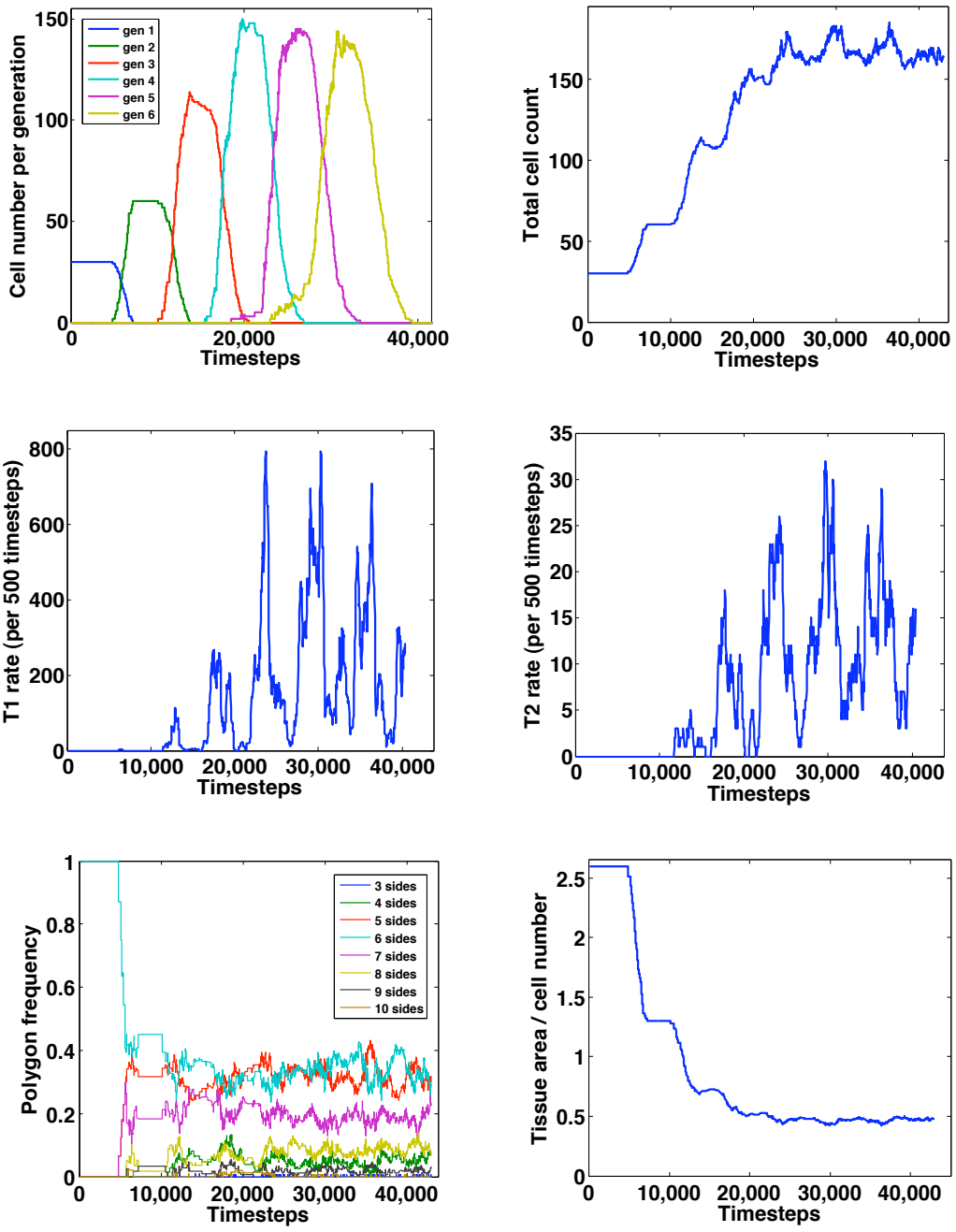

Figure 2.9: Graphs showing evolution of tissue of fixed size with co-ordinated cell divisions.

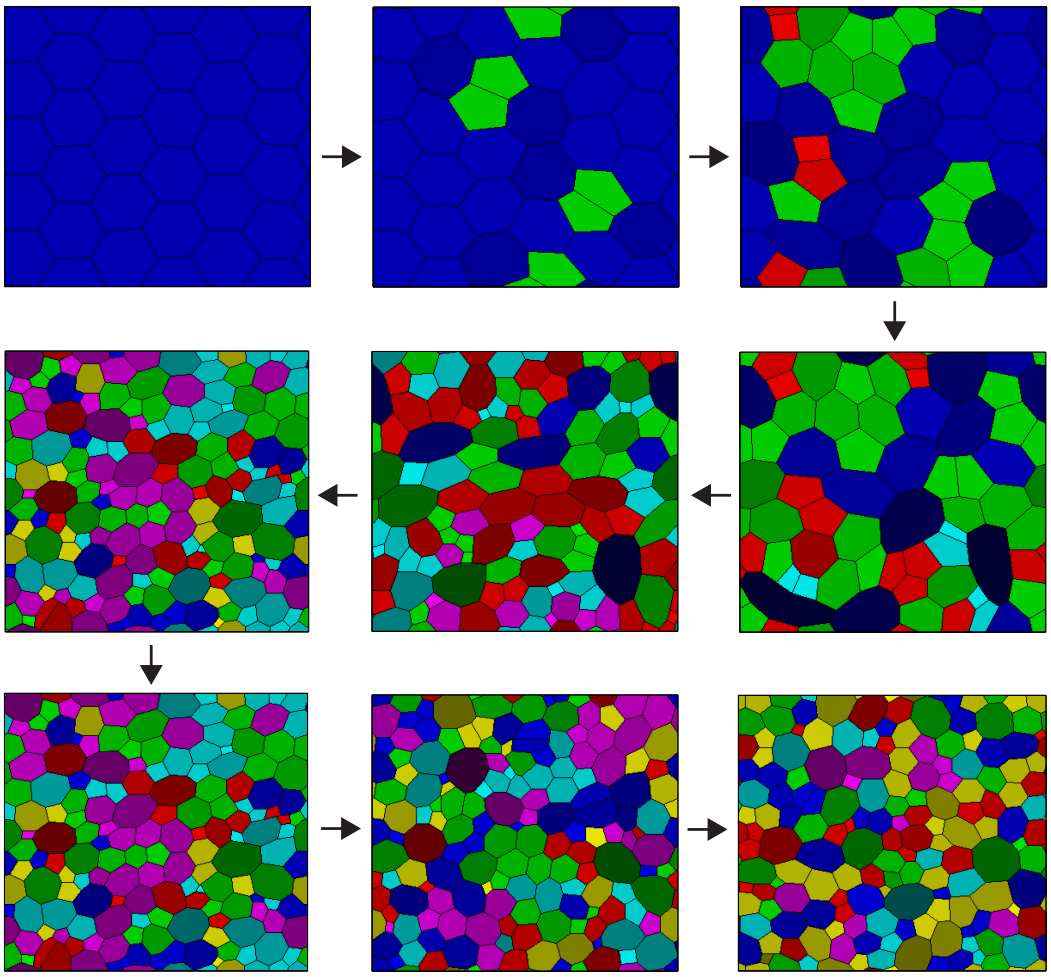

Figure 2.10: Stills showing evolution of tissue of finite size with a uniform rate of cell division. Colour coding: Blue - generation 1; Green - generation 2; Red - generation 3; Turquoise - generation 4; Magenta - generation 5; Green - generation 6; Blue - generation 7; Yellow - generation 8; etc.

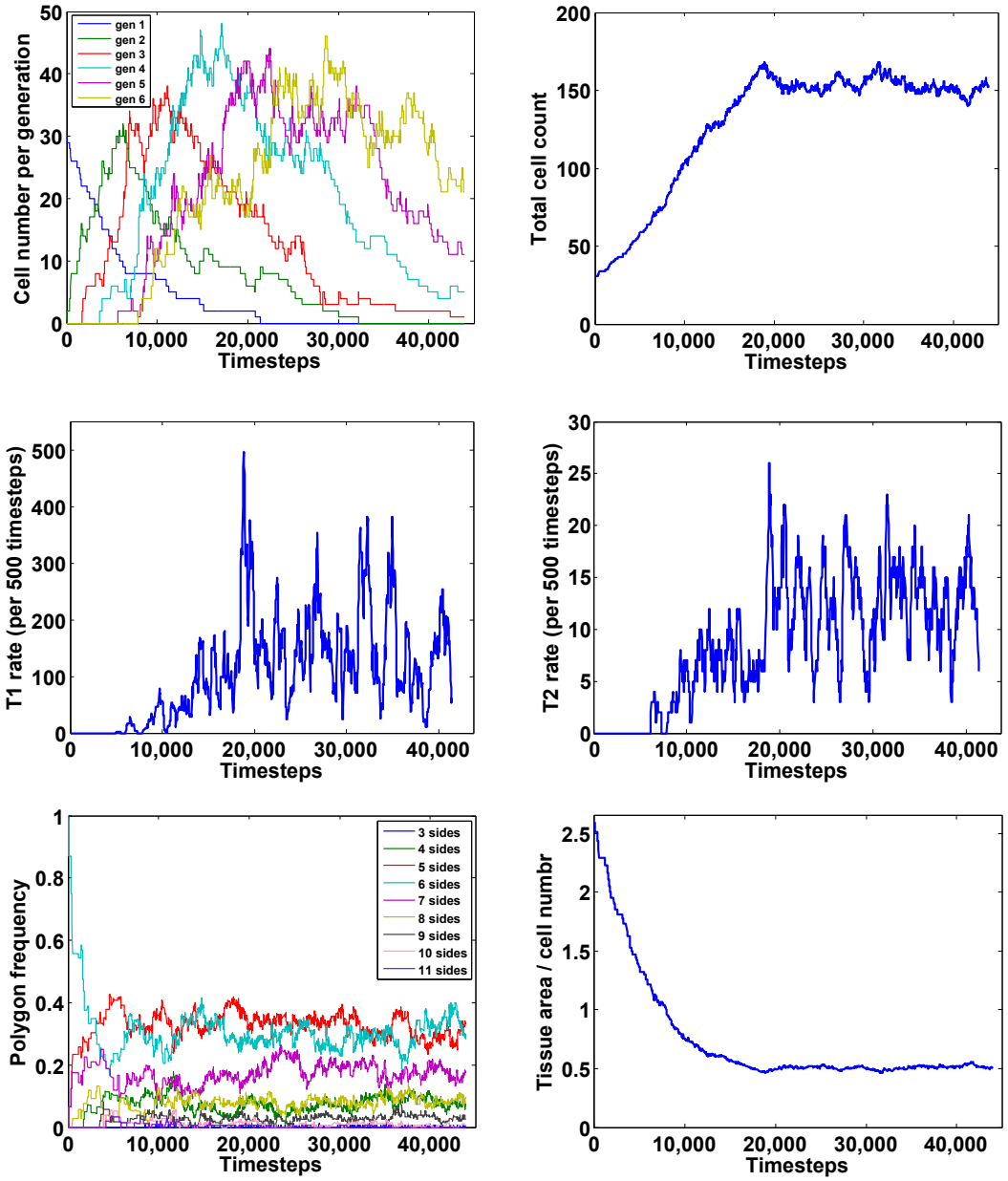

Figure 2.11: Graphs showing evolution of tissue of finite size with a uniform rate of cell division.

2.9.3 Growing tissue with co-ordinated cell division

We now simulate a tissue of unconstrained size. The total tissue area $A_{box} = x_{max} \times y_{max}$ is updated at every 5^{th} timestep using the same probabilistic rule as the one for vertex moves. The change

$$x_{max} \to x_{max} \times (1 + p_x)$$
$$y_{max} \to y_{max} \times (1 + p_y)$$

is accepted with the following probabilities:

$$\text{if} \quad W' < W, \text{ probability } 1,$$
$$\text{if} \quad W' \geq W, \text{ probability } e^{-\Delta W},$$

where $p_x = (r_1 - 0.5) \times P$ and $p_y = (r_2 - 0.5) \times P$ with $P = 0.01$, and r_1, r_2 random numbers between 0 and 1; W is the work function before the change, W' is the work function after the change, and $\Delta W = W' - W$.

As previously for the case of a tissue of fixed size, we study and compare the equilibrium states resulting from co-ordinated cell divisions and uniform cell divisions. The co-ordinated cell divisions are simulated using the same gamma-distributed probability of cell division used for the tissue of constrained size, as described in Section 3.9.1. The stills showing growing tissue with co-ordinated cell divisions are shown in Figure 2.12.

The most obvious distinction to the previously presented cases, where the tissue size is fixed, is that the total cell number for the growing tissue does not saturate, but keeps growing at a nearly exponential rate (Figure 2.13, Panel 2). Equally, the rates of T1 and T2 transitions increase with the increase in the total number of cells. They also exhibit a periodic trend, similar to the one observed for the co-ordinated cell division in a fixed tissue. However, the rate of T1 transitions per cell is significantly lower for the growing tissue when compared to the fixed tissue. There are more than 15 T1 transitions per cell in a fixed tissue for every T1 transition per cell in a growing tissue, as can be seen by comparing Panels 2 and 3 in Figure 2.9 with those in Figure 2.13. Similarly, there are fewer T2 transitions in the growing tissue than there are in the tissue of fixed size. There are around 10 T2 transitions in the tissue of fixed size for every T2 transition in the growing tissue, as can be seen by comparing Panels 2

and 4 in Figure 2.9 with those in Figure 2.13. This is consistent with the assumption that the fixed tissue with cell division experiences higher compression as the total number of cells increases and therefore mechanical forces favour T2 transitions as a means of reducing the total cell number and thus reducing the overcrowding.

The distribution of polygon types is shown in Panel 5 of Figure 2.13 and the equilibrium probability distribution in Figure 2.17, Panel 4.

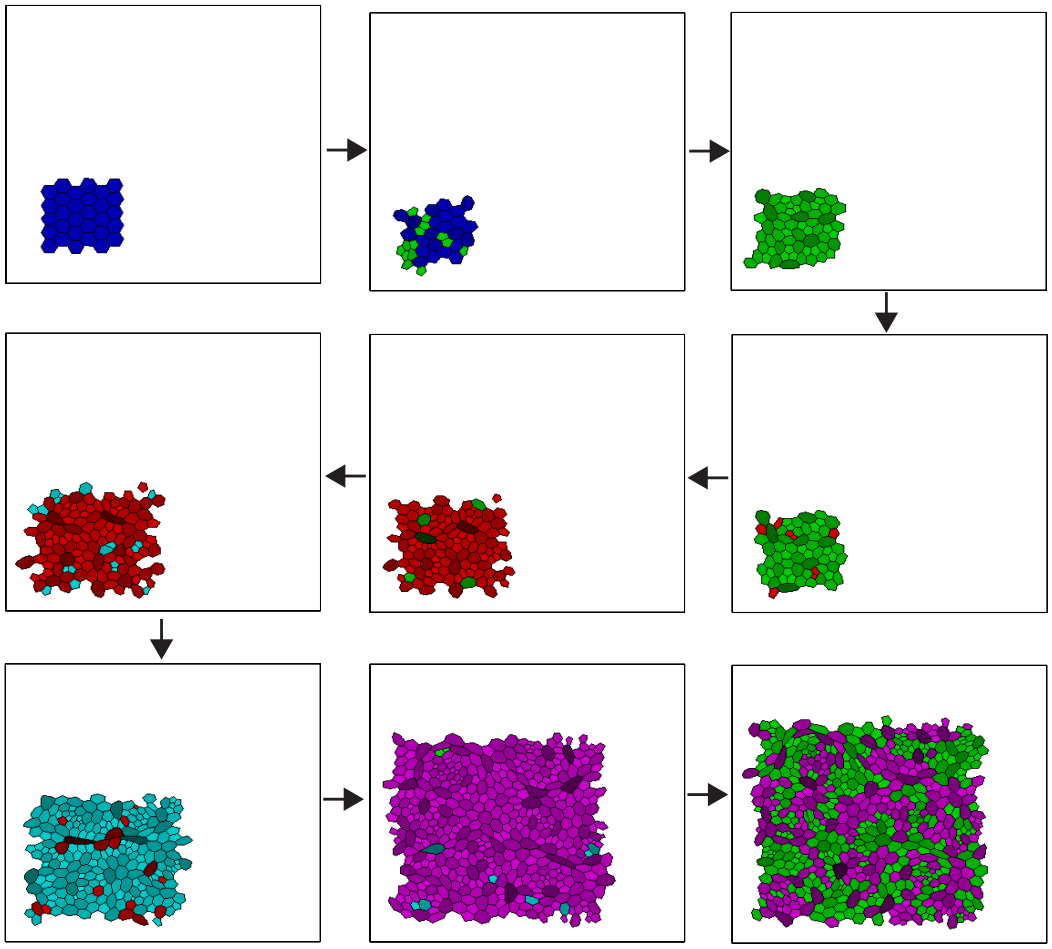

Figure 2.12: Stills showing evolution of growing tissue with co-ordinated cell division. Colour coding: Blue - generation 1; Green - generation 2; Red - generation 3; Turquoise - generation 4; Magenta - generation 5; Green - generation 6.

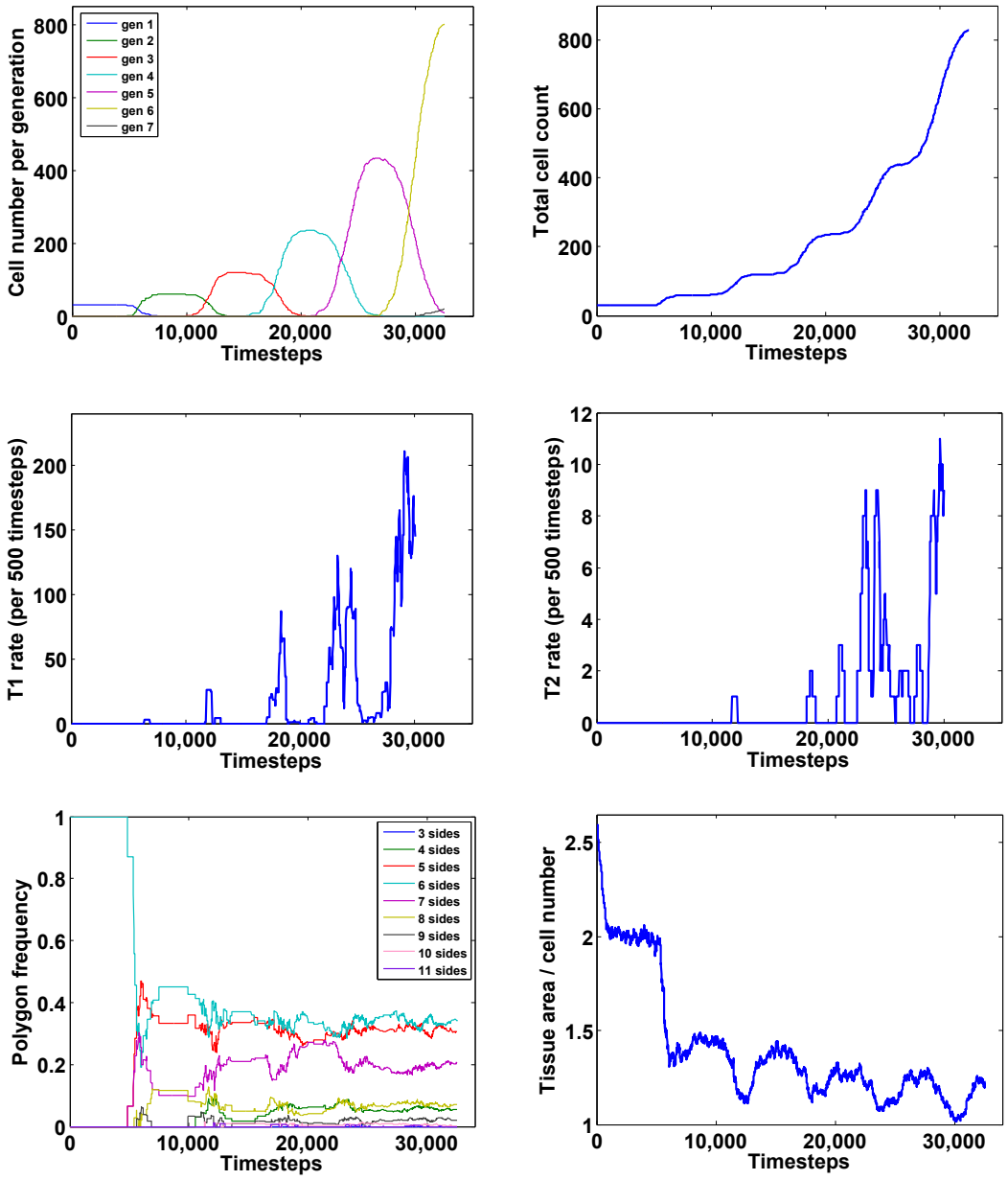

Figure 2.13: Graphs showing evolution of growing tissue with co-ordinated cell division.

2.9.4 Growing tissue with a uniform rate of cell division

Finally, in Figure 2.14, we show the simulation of a growing tissue with the uniform rate of cell divisions. The rule for the cell divisions is the same as the one described in Section 3.9.2., i.e. cell division events are modelled as a Poisson process. Figure 2.15 shows the characteristics of the equilibrium reached in this case, and Figure 2.17, Panel 4 shows the equilibrium polygon distribution.

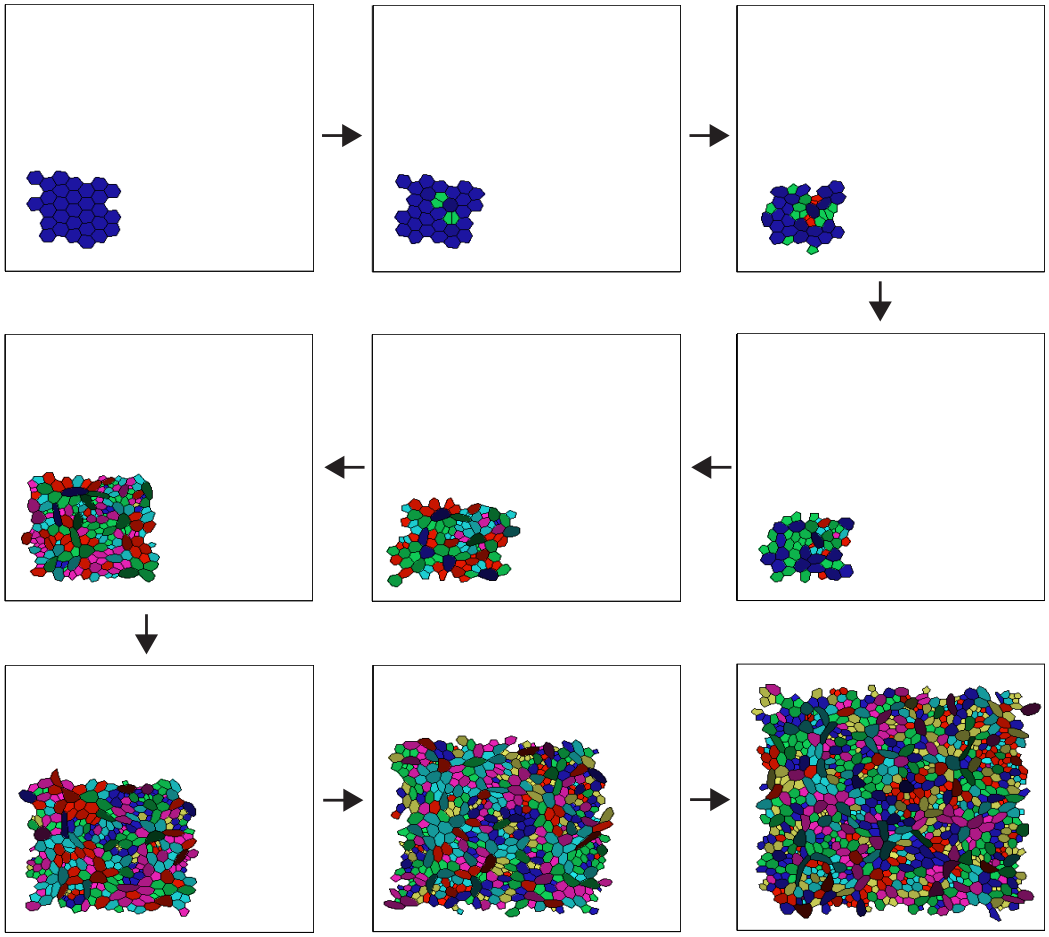

Figure 2.14: Stills showing evolution of growing tissue with a uniform rate of cell division. Colour coding: Blue - generation 1; Green - generation 2; Red - generation 3; Turquoise - generation 4; Magenta - generation 5; Green - generation 6; Blue - generation 7; Yellow - generation 8; etc.

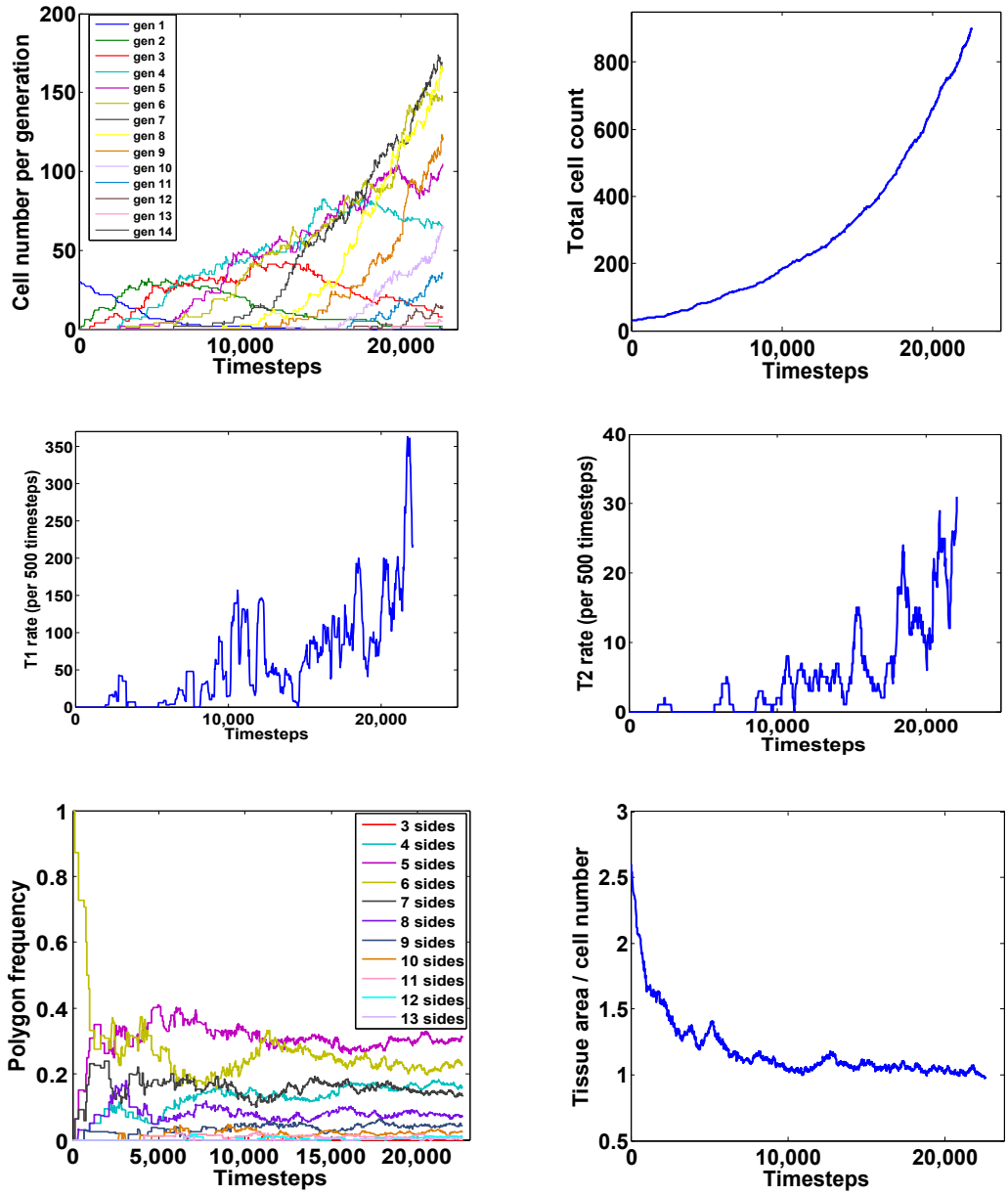

Figure 2.15: Graphs showing evolution of growing tissue with a uniform rate of cell division.

2.9.5 The effect of noise on tissue homeostasis

In order to check the possible effect of the level of noise on the polygon distribution and on the T1 and the T2 rates, we simulate a growing tissue with co-ordinated cell division with noise increased to 5 times the value used for the previous simulations (parameter values shown in Table 2.2).

Table 2.2: Parameters values for the higher noise simulation.

A_0	1.30
K	32.0
Λ	11.36
Γ	9.98

The results are shown in Figure 2.16 and in Panel 5 of Figure 2.17. It is interesting to note that higher noise leads to a more ordered tissue, as reflected by the low value of the variance of the equilibrium polygon distribution (Table 2.3). This could be because noise enables the T1 transitions that are required to redistribute edges amongst adjacent cells following a division event. Therefore, increasing noise corresponds to annealing the tissue. A low value of noise would forbid any vertex move that increases the value of the work function and the evolution would occur strictly in the direction of a decrease in the work function. Increasing the value of the noise corresponds to enabling the cell configuration to better explore the work function landscape and therefore leave local equilibria in order to find the global equilibrium. Since increasing the value of the noise leads to a more ordered tissue, we conclude that the entropic contribution of the noise is not significant to the equilibrium configuration, since the entropic contribution induces disorder with the increase in the value of noise. Hence, it is safe to assume that the equilibrium configuration depends predominantly on the mechanics of the tissue and on the rule for cell divisions and the choice of their timing, rather than on the value of the noise.

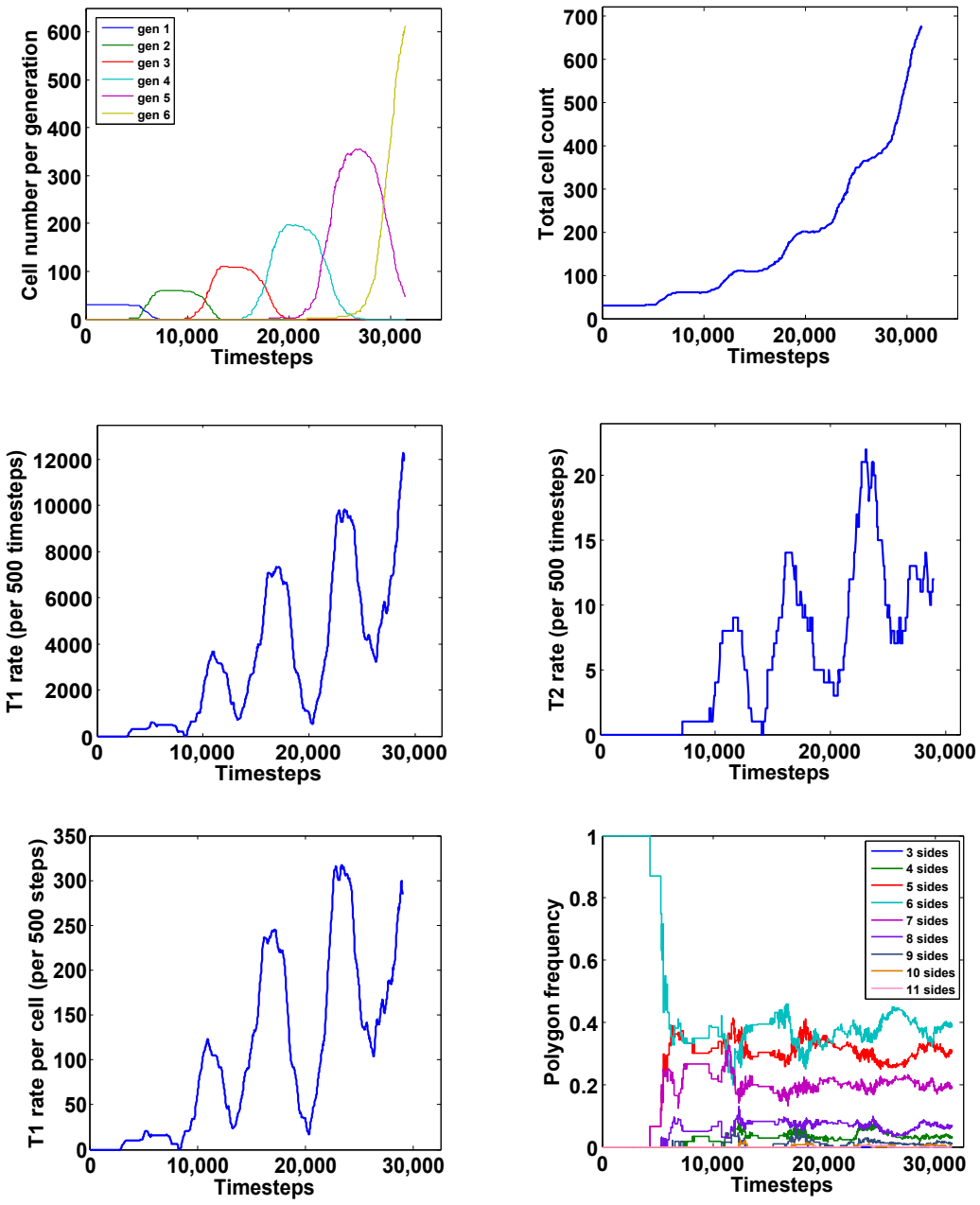

Figure 2.16: Graphs showing evolution of growing tissue with co-ordinated cell division with noise increased to 5 times the value used for the previous simulations.

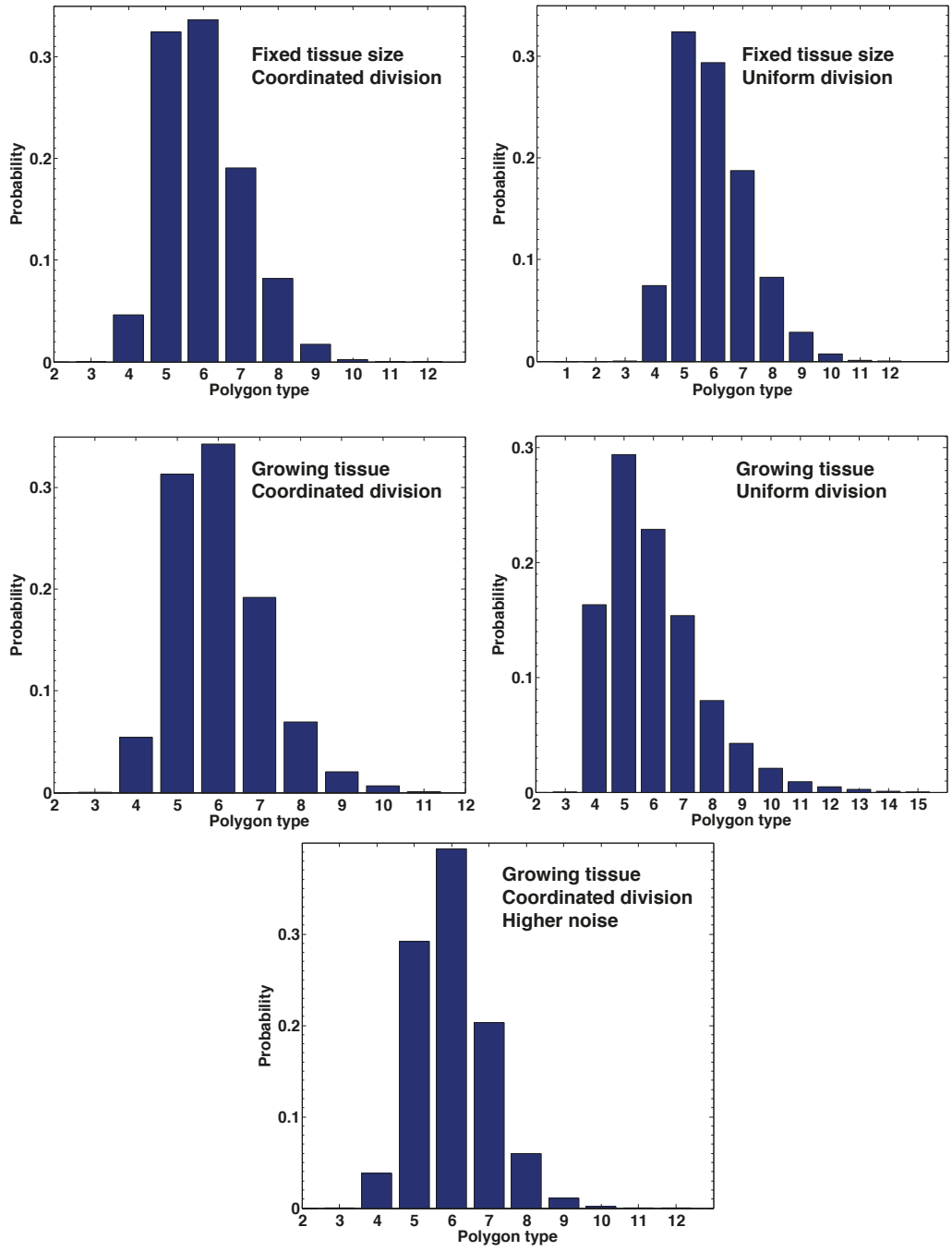

Figure 2.17: Probability distribution of polygon types for five different simulations.

Table 2.3: Probability distribution of polygon types for tissue of fixed size with coordinated and uniform cell division, and for the growing tissue with coordinated and uniform cell division, and a growing tissue with coordinated cell divisions with higher noise.

	EX	$Var(X)$
Box coord.	6.00	1.23
Box uniform	6.00	1.55
Free coord.	6.00	1.31
Free uniform	6.00	2.67
Free coord. noise	6.00	1.03

2.10 Discussion

Although this is a greatly simplified model of epithelial tissues, several interesting conclusions could be made based on the generic features of cell-cell networks.

It is interesting to note that the synchronized division clearly yields a lower variance than random division (Table 2.3). Presumably, the function of epithelial tissues as barriers would favour uniformity and order. Since coordinated cell division yields a lower variance and hence more unformity, the tissue would favour coordinated cell division to stochastic cell division. Indeed, cell division in the notum of the developing *Drosophila Melanogaster* is coordinated in that it takes place during defined time periods followed by quiescent periods in which no divisions occur.

We also see that the polygon distribution in the tissue with fixed size has a lower variance than the unconstrained tissue, both for the case of coordinated and uncoordinated cell division.

Furthermore, we see that increasing noise can produce a more regularly packed epithelium. Future research should focus on identifying the spectrum of the noise, since this my have an effect on equilibrium configurations.

Chapter 3

Live cell delamination as a novel homeostatic process

Author contributions: This chapter describes the results of a collaborative project with Eliana Marinari and Buzz Baum from LMCB, UCL. The experiments and data analysis were performed by E. Marinari under the supervision of B.Baum. The modeling and simulations were performed by me. The direction and the final conclusions of the project were the result of collective effort of E. Marinari, B. Baum, T. Duke and me during our numerous meetings in 2010 and 2011.

3.1 Introduction

Homeostasis is a general principle of functioning of living organisms. It refers to their ability to regulate their internal state in response to fluctuations in the external conditions, so as to stabilise their health and functioning. Homeostasis is believed to be achieved through a system of positive and negative feedback mechanisms. In tissue growth and development, as well as in adult tissue renewal and maintenance, cells respond to cues in their environment in an orchestrated manner, in order to achieve the desired tissue-level outcome. For example, in the case of cell apoptosis in an epithelial tissue, cells die and leave the tissue without disrupting the structural integrity of the epithelium. Since epithelia must provide tight barriers between the organs and tissues which they envelop, preserving epithelial structure amounts to ensuring that epithelial function is uninterrupted (Rosenblatt et al [52]), while individual cells are recycled and the tissue is renewed.

In general, understanding homeostatic mechanisms is important for understanding how tissues grow and develop and what their dynamics is in an adult organism. Since the disruption of homeostasis is linked to disease, most prominently to tumourigenesis, it is of central concern to dissect the details of healthy homeostasis as well as understand the transition to and the details of an unhealthy type of homeostasis. For example, recent work (Basan et al [53]) proposes to quantify the deviation from the equilibrium homeostatic tissue pressure as a parameter that directly affects the likelihood of metastases in tumours.

In this chapter, through a series of experiments supported by computational analysis, we believe to have identified a novel process of homeostasis whereby living cells leave an epithelial tissue in response to mechanical cues (Marinari et al [54]). This is one of the first direct demonstrations of the role of mechanics in tissue growth control.

3.2 The role of mechanics in tissue morphogenesis

In recent years, several researchers have proposed a role for mechanics in the regulation of tissue growth and in morphogenesis in general (Bittig et al [55], Landsberg et al [56], Ranft et al [57], Shraiman [50], Hufnagel et al [35], Solon et al [58], Solon et al [59], Aegerter-Wilmsen et al [60]).

The majority of published work focuses on the possible theoretical frameworks which would enable mechanical regulatory functions in tissues. Here, I review the most notable theoretical contributions.

Shraiman [50] proposes that uniform tissue growth could be the result of the negative feedback induced by *mechanical stress* in the tissue on the cell division rate. Hufnagel et al [35] propose a theoretical framework which would explain the arrest of tissue growth when an organ reaches the desired size. The regulation is effected through the coupling between cell division and growth rate on one hand, and tissue stresses and the Dpp morphogen concentration on the other.

Aegerter-Wilmsen et al [60] combine computational analysis with *in vivo* experiments to propose that mechanical stress induced by cell growth can have an effect on the cell division rate (and on the length of the cell cycle in general), and that this coupling would result in a predicted and observable deformation in tissue topology. They observe the predicted deformation in the *Drosophila* wing disc and conclude that

there is strong evidence to believe that cell growth is indeed coupled to the rate of cell divisions through mechanical feedback. This is an indirect experimental confirmation of the role of mechanics in the regulation of tissue growth.

Ranft et al [57] present a theoretical analysis showing that tissue at large scales effectively behaves as a viscoelastic fluid, where cell division and *apoptosis* are stress sources.

Through a combination of results from the continuum theory of fluids and aided by a discrete computational model of cells, Bittig at al [55] find that under fairly general assumptions, anisotropy in the orientation of cell division results in the accumulation of mechanical stress which would spontaneously shear the tissue.

Aigouy et al [61] establish the effect of anisotropic tension on tissue shape and cell orientation, whereby the tension affects cell elongation, cell rearrangements and cell divisions. The model system is the *Drosophila* wing in the pupal stage. The wing hinge contracts and induces anisotropic tension in the wing blade. This tension in turn affects cell division, cell elongation and cell movement, so that long range cell orientation and the planar cell polarity axis is aligned with the proximal distal axis.

The role of mechanics in tissue organisation and tissue growth has received considerable attention in the literature in the past few years. Here, we build on this body of work to look for the connection between mechanical stress in the tissue and the rate of cell delamination.

3.3 The role of apoptosis in tissue homeostasis and morphogenesis

Apoptosis is the process of programmed cell death. It involves the activity of many genes (Hengartner [62]), and it is essential for maintaining homeostasis in adult epithelia and for shaping a developing embryo.

In adult epithelia, cells are disposed of through apoptosis. Rosenblatt et al [52] show that a dying cell sends a signal to its neighbours, which mobilizes actin and myosin within the neighbours to form a ring surrounding the dying cell. A similar acto-myosin ring also forms within the dying cell too. This mechanical ring extrudes the dying cell from the tissue and the neighbours close the resulting gap with their

bodies. In this way, tissue function as a barrier is never compromised and dying cells do not expose gaps, as was confirmed by electrical resistance studies [52].

More recently, apoptosis was shown to play a role in tissue development too (Manjón et al [63]). Since apoptosis involves spatial rearrangements and the recruitment of acto-myosin, it is a force-generating process. This apoptotic force could conceivably be put to a good use, if organisms optimise the use of available energy sources. Remarkably, Toyama et al [64] show that apoptotic force does indeed help drive dorsal closure in *Drosophila* embryos, a morphogenetic process that requires mechanical pulling.

We study delaminating cells in the developing *Drosophila* notum where the relief of mechanical stress through cell delamination can play a role in tissue morphogenesis.

3.4 Cells in the midline delaminate more often than they do elsewhere

The notum is the future dorsal thorax of the fly. It forms when two opposing imaginal wing discs meet and merge in the region of the tissue called the midline (Figure 3.1, also Section 1.2).

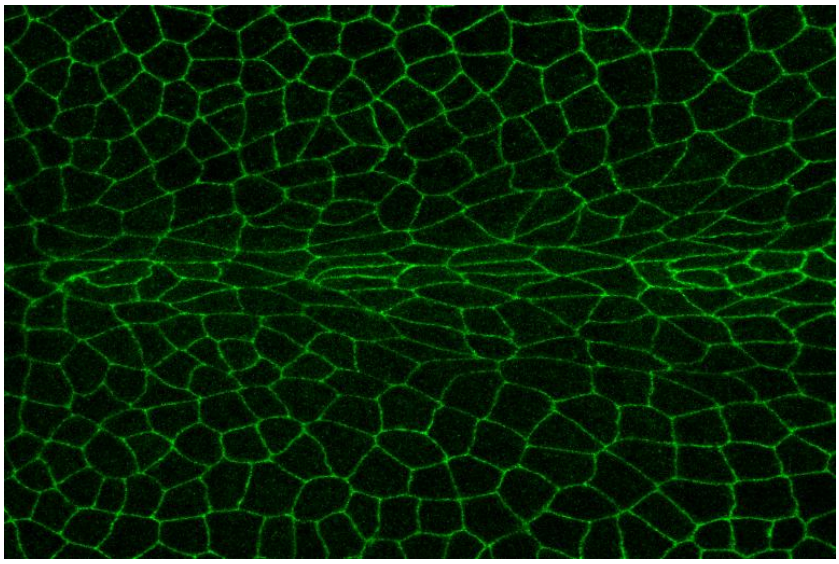

Figure 3.1: The midline of the notum has a different geometry from the rest of the tissue at the beginning of pupal development.

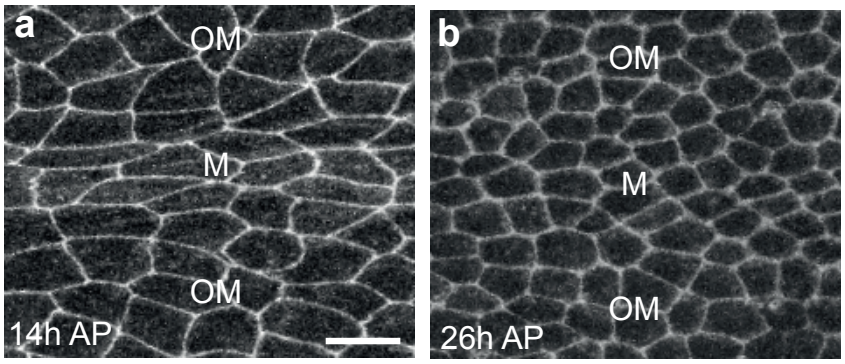

Figure 3.2: The cells in the midline at (a) the beginning and at (b) the end of pupal development.

During pupal development, the notum retains a fixed shape and constant size. However, there are significant internal changes that occur during this period. Most cells divide, some cells leave the tissue, the cells in the midline change shape and the overall packing of the cells becomes a lot more regular and isotropic towards the end of pupal development.

At the onset of pupal development, it is apparent that cells in the midline have a different shape than the surrounding cells. They appear elongated and squashed. As cells rearrange and the tissue organises, these anisotropies disappear (Fig 3.2).

Apart from the changes in cell shape which lead to the establishment of a homogeneous tissue throughout the notum, there is another striking feature of the midline pupal development. The cells in the midline leave the tissue much more often than do cells outside the midline. At the end of pupal development, during the period from $15h$ to $26h$ after pupa formation (APF), $32.5 \pm 13.6\%$ of cells in the midline have delaminated basally, in contrast to $0.5 \pm 0.3\%$ of cells in the surrounding tissue (mean $\pm$ s.d., $n = 4$ pupae), (Fig. 3.3, 3.4).

3.5 The spatial and the temporal patterns of delamination appear to be stochastic

In the experiments performed by E. Marinari and B. Baum, there were no discernible regular patterns of cell delamination. First, looking at different animals, the pattern

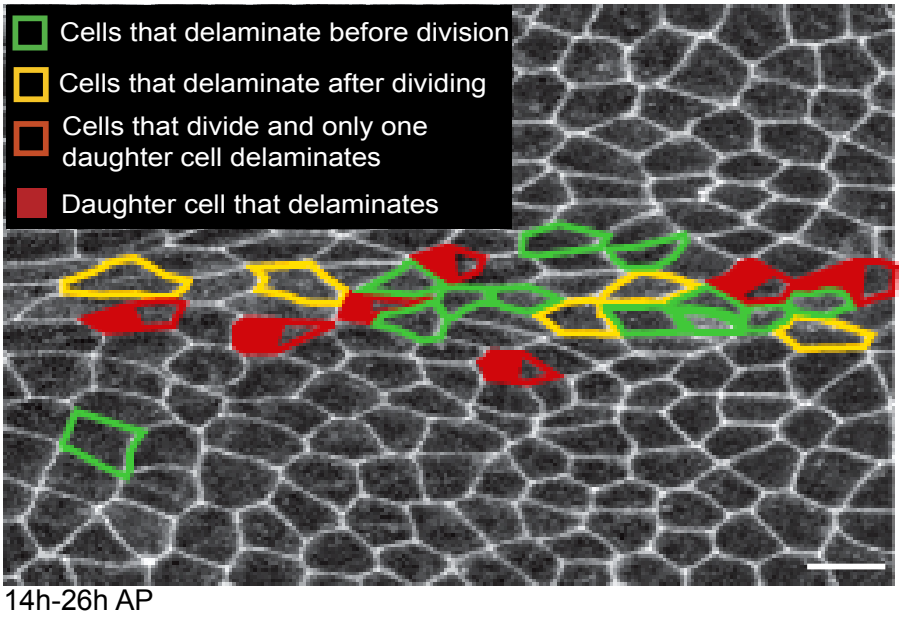

Figure 3.3: The cumulative percentage of cells that have delaminated in the midline and in the outside tissue at the end of pupal development.

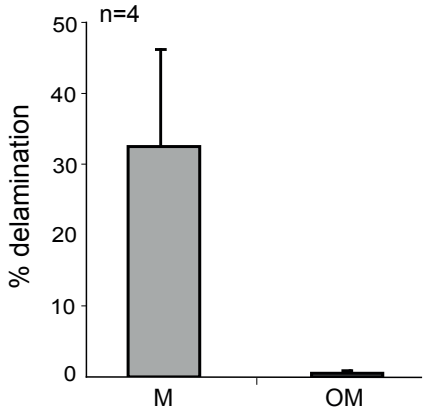

Figure 3.4: The cumulative percentage of cells that have delaminated in the midline and in the outside tissue at the end of pupal development.

of delamination varies. Second, there is no symmetry in the delamination around the midline. This rules out the roles of cell position or of developmental time as the causes of delamination. Third, cell delamination occured both before and after cell divisions, and the proportion of cells that delaminated before and after the division varies. Finally, it is common that only one of two sister epithelial cells delaminates. This rules out the role of cell lineage as the determinant of delamination.

Therefore, we conclude that it is highly likely that cell delamination is both temporally and spatially stochastic.

3.6 Tissue in the midline appears to be compressed by mechanical stress

Might it be that tissue stress were the main cause of cell delamination? Cells in the midline appear elongated, as if they are under compression. Before the onset of delamination, the aspect ratio of the cell in the midline was on average 2.7 times longer than it was wide, as measured along the antero-posterior axis of the body. However, their apical areas are not very different from those of the cells in the surrounding tissue ($48.5 \pm 14.2 \mu m^2$ in the midline and $51.3 \pm 12.7 \mu m^2$ outside). Furthermore, the junctions of the midline cells appear wiggly and irregular (Figure 3.6).

To further investigate whether the midline cells experience higher mechanical compression than the surrounding cells, experiments were done to see how cell nuclei are positioned along the apico-basal (or the z) axis. In the left panel of Figure 3.5, it can be seen that the nuclei of the cells in the midline are positioned more basally than the nuclei of the surrounding tissue. This suggests that these midline nuclei are pushed down by a compressive force, as would happen in a crowded environment. Moreover, the aspect ratio of the nuclei of the midline cells is elongated, with the long/short axis ratio of 1.9 ± 0.4. In comparison, the nuclei of the cells in the surrounding tissue are nearly round, with a long/short axis ratio of 1.1 ± 0.1.

Finally, laser cuts experiments reveal that junctions in the midline are under more tension than the surrounding cells. Following a laser nano-dissection of the junction, the junctions in the midline moved by $0.6 \pm 0.2 \mu m$ at $10s$ and $0.7 \pm 0.3 \mu m$ at $16s$. This is in clear contrast with the junctions outside the midline, which moved through

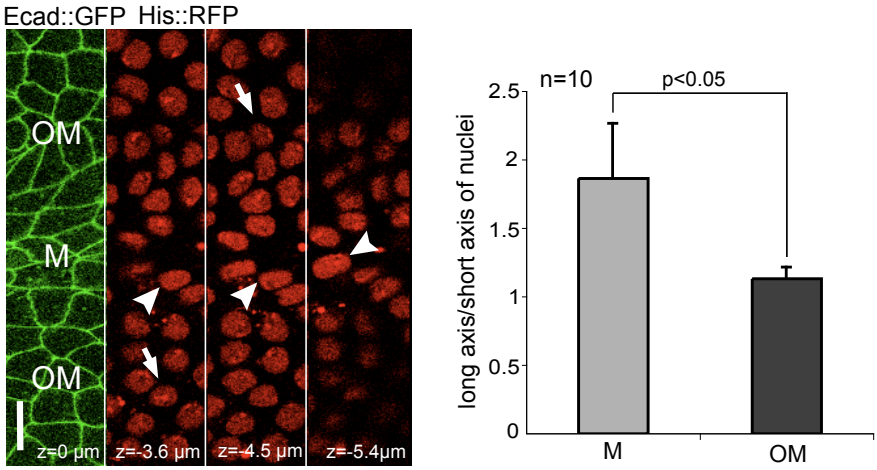

Figure 3.5: The tissue in the midline is compressed as indicated by the aspect ratio of the cell nuclei as well as the positions of the cell nuclei on the z-axis.

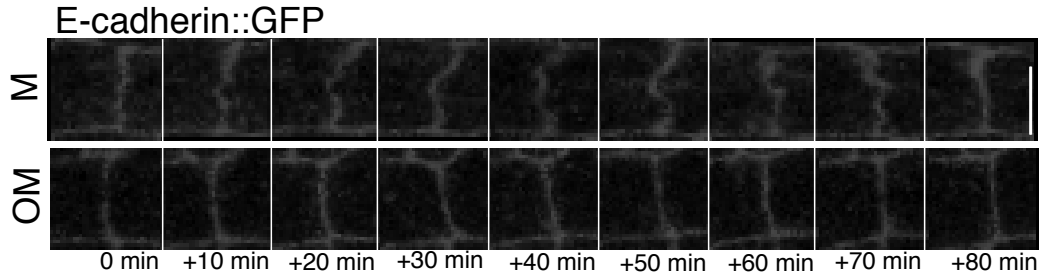

Figure 3.6: Junctions between cells in the midline of the notum are convoluted as if subject to compression. Timelapse of junctions in the midline (M) and outside the midline (OM), visualized with E-cad::GFP. Scale bar, $5\mu m$.

only a third of that displacement, namely by $0.2 \pm 0.3\mu m$ at $10s$ and $0.3 \pm 0.2\mu m$ at $16s$, following the laser cut.

Significantly, at the end of pupal development, by 26h APF, this difference in junctional tension disappears. The measurements of $1.19 \pm 0.6\mu m$ for junctions within the midline region and $1.19 \pm 0.5\mu m$ for those outside of the midline at $10s$ after laser cutting ($1.6 \pm 0.5\mu m$ and $1.7 \pm 0.8\mu m$ respectively at $16s$) show that isotropy is established. This indicates that the variation of the mechanical stress across the tissue disappeared and the tissue reached a mechanical equilibrium. Wiggly junctions have disappeared too, and the junctional tension is higher than it was for the early pupae. Also, the nuclei are no longer compressed.

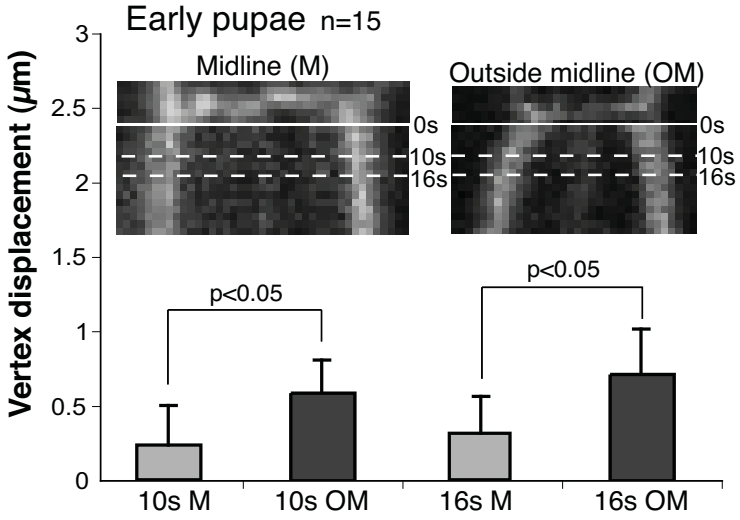

Figure 3.7: Quantification and kymograph analysis of vertex displacement after laser ablation for early pupae (14h-16h AP). Images show the junction before the cut and the kymograph after the cut (0s). Dotted lines indicate 10s and 16s after cutting. Scale bar, $10\mu m$.

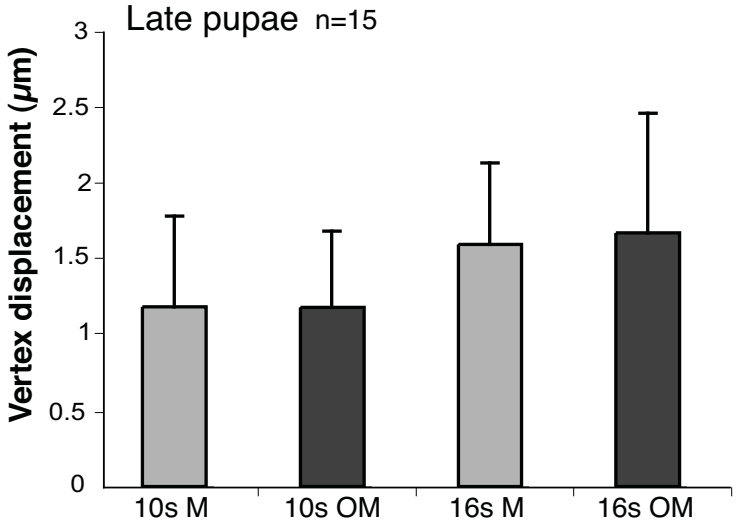

Figure 3.8: Quantification of the vertex displacement of single junctions after laser ablation for late pupae (24h-26h AP).

These results suggest that cell delamination may be a mechanism through which the tissue releases excess stress in order to reach isotropy and mechanical equilibrium.

3.7 High compression in rapid growth mutants increases cell delamination

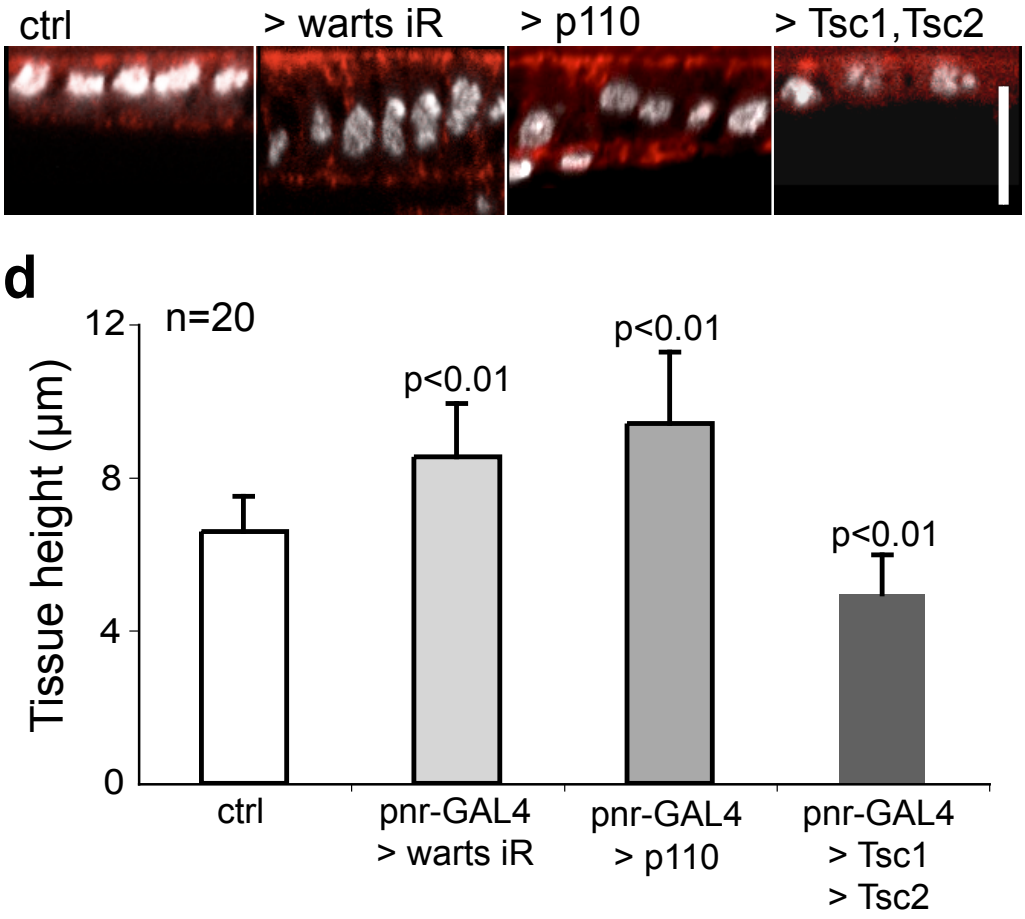

Figure 3.9: The height of an epithelium correlates with the growth rate. Average tissue height (n=20 different regions from 4 different pupae) for control, tissues expressing p110 PI3K (inducing high growth), Tsc1 and Tsc2 (inducing low growth), and RNAi targeting Warts (inducing high growth). Scale bar, $10\mu m$.

In order to test the role of compression in inducing cell delamination, a series of experiments were performed. By creating suitable mutant animals in which growth

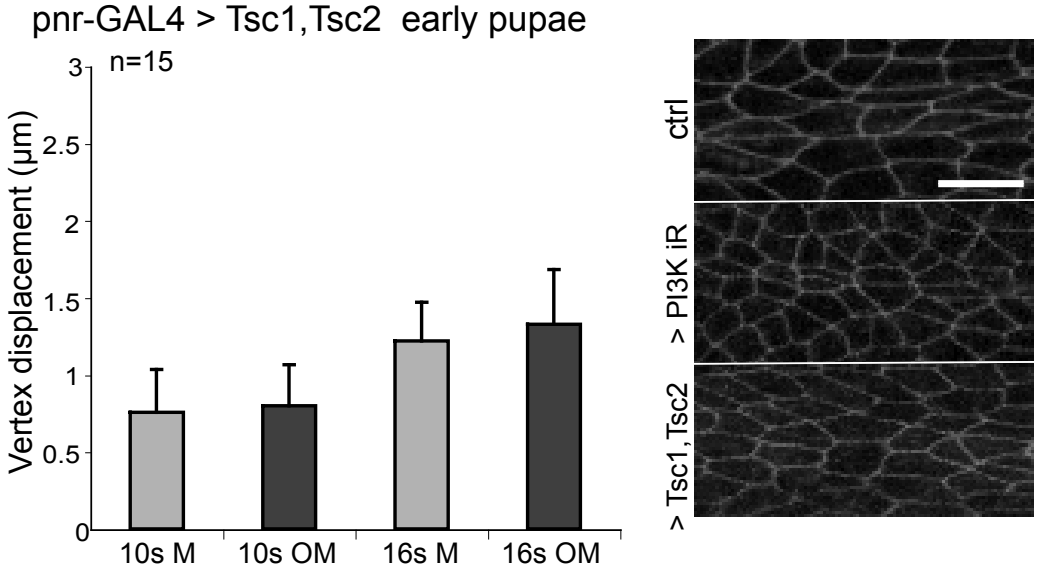

Figure 3.10: Junctional tension as measured by vertex displacements upon laser ablation in animals expressing high levels of Tsc1 and Tsc2 is uniform across the whole tissue. Scale bar, $10\mu m$.

is manipulated in order to produce tissues with varying amounts of compression, it is possible to test the hypothesis that compression induces delamination.

Mutants were created with:

1. high growth (p110 PI3K expression, Warts RNAi, PTEN RNAi)
2. low growth (Tsc1, Tsc2 expression, p110 PI3K RNAi)
3. inhibited cell division (Cdc25 RNAi).

To this end, ectopic gene expression and RNAi were used to target components of the PI3K and hippo pathways within the pnr expression domain.

The mutant tissue p110 exhibits *more growth* as measured by a 1.5 fold increase in cell height as shown in Figure 3.9. This increase in growth and overcrowding is accompanied by a significant increase in cell delamination within the midline, as seen in Figure 3.11 and 3.12. It is telling that the enhanced growth also induced higher rates of cell delamination in the surrounding tissue. Moreover, in these high growth mutants, tissue appears to buckle in regions around the midline. As seen in Figure

3.13, cell delamination is particularly high around these folds, which appear crowded and where mechanical stress is likely to be high.

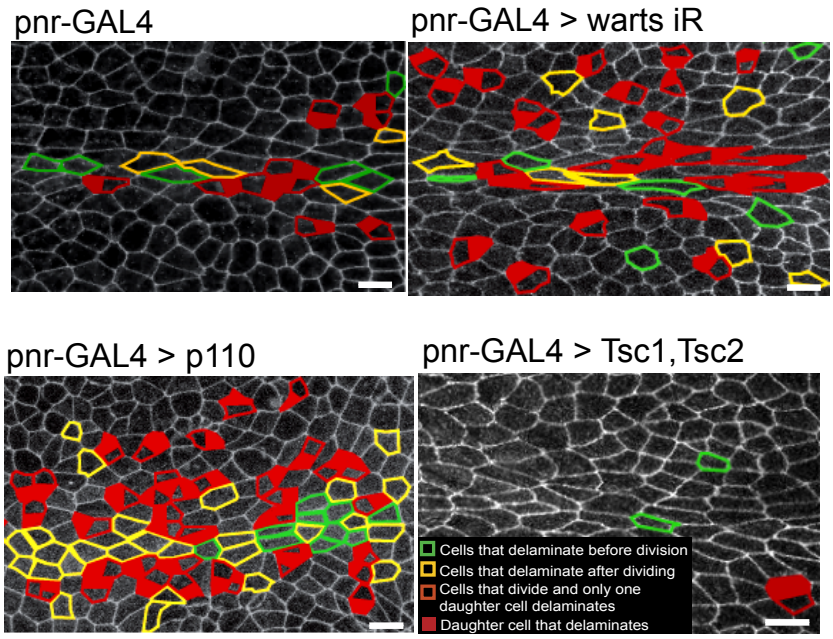

Figure 3.11: Cell delamination rate correlates positively with the rate of cell growth in mutants with high and low growth. Cells that delaminate are marked with colours. Scale bars $10\mu m$.

Now, considering a reverse situation, where growth is reduced, we observe a similar impact on delamination. Animals expressing PI3K RNAi and also both Tsc1 and Tsc2 have lower cell growth as seen from inspecting tissue height, Figure 3.9. Growth was entirely absent in animals that survived the expression of RNAi targeting a subunit of the 5S ribosome. Cell delamination is indeed lower in these low growth mutants (Figure 3.11), which is consistent with the hypothesis that delamination depends on compression.

Junctional tension was measured in the case of low growth animals (Figure 3.10). Consistently with the hypothesis, junctional tension correlates with the changes in growth rates, and in the case of low growth and low delamination mutants, the tension is uniform across the whole tissue.

Finally, to check whether cell delamination depends on cell division, mutants with

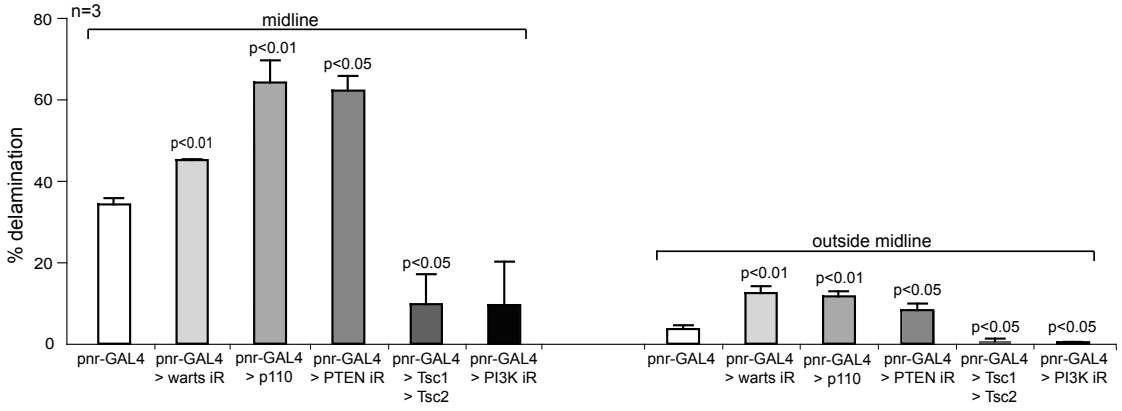

Figure 3.12: The rate of delamination in rapid growth mutants, and in the suppressed growth mutants, compared with the wild-type tissue. Average rates of delamination (n=3 pupae) for cells in the midline and outside midline in control animals, in tissues where growth was increased (p110 PI3K expression, PTEN RNAi, Warts RNAi) and in nota with reduced growth (p110 PI3K RNAi, Tsc1 and Tsc2 expression).

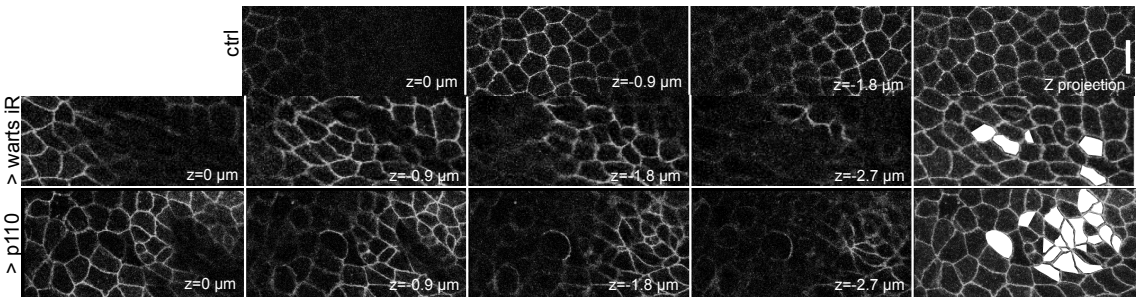

Figure 3.13: Tissue buckles under lateral compression. Scale bar, 10μmu.

inhibited cell division (expressing RNAi for Cdc25) were produced. As shown in Figure 3.14, cells in the midline continue to delaminate.

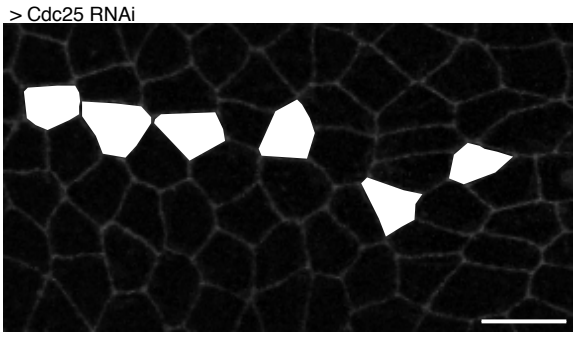

Figure 3.14: Z projection of Ecad::GFP tissue expressing RNAi for Cdc25. Although division is inhibited, local cell delamination in the midline region continues (labeled in white) over a period of 135 min. Scale bar, $10\mu m$.

3.8 Modeling the midline mechanics

Having thus narrowed down the options for the primary cause of cell delamination, by excluding the role of cell lineage, positional information or developmental time information, it is sensible to consider the effect of mechanical stress in the epithelial sheet. To this end, we use our vertex model of tissue mechanics, suitably adapted for studying the notum.

The first test we consider concerns the *anisotropy* of the tissue in the midline. On quick inspection, it is clear that the tissue in the midline is not in a state of mechanical equilibrium as defined by the work function of the model. Cells are elongated with an average aspect ratio of 2.7:1, and since the work function has no inbuilt asymmetry or anisotropy, this must be an out-of-equilibrium configuration. Therefore, as tissue evolution would proceed towards minimising the free energy, this would induce tissue rearrangements towards an isotropic configuration.

In preparation of the initial conditions, the parameter values are chosen to result in distributions of cell size and junction number that reflect realistic tissue configurations, as described by Farhadifar et al [36]. The parameter values are displayed in Table

3.16. Although our work function expression differs from that in [36], we believe that the effect of this change on the resulting equilibrium configuration is not large.

To be more exact, the polygonal distribution of the cellular network in the initial condition we use is shown in Figure 3.15. This polygonal distribution is thought to closely reflect the equilibrium tissue configuration *in vivo*, as studied by Gibson et al in [41], reproduced in Figure 3.15.

We prepare the initial condition by starting with the regular hexagonal lattice with $N = 120$ cells, and let it evolve through 5 rounds of cell divisions. The crowding of the tissue resulting from cell divisions is accompanied by T2 transitions, and the cell number eventually equilibrates at $N_0 = 240$. The rectangular area is fixed at $A_{tissue} = N_0 A_0$.

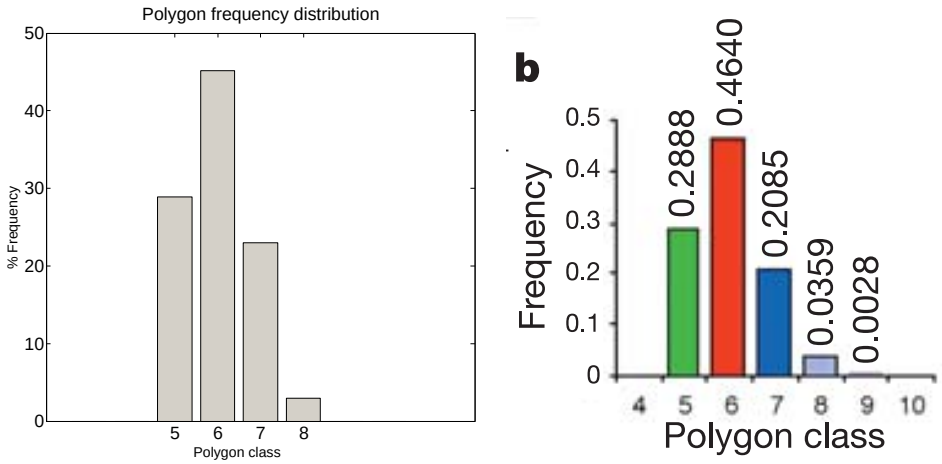

Figure 3.15: **a.** The distribution of polygons for the initial condition; Cell number=240. **b.** Theoretical equilibrium distribution (Adapted from Gibson et al [41]).

Uncompressed tissue	Compressed tissue
$A^0 = 1.30$	$A^{0\prime} = \gamma A_0$
$K = 160$	$K' = \gamma^{-2} K$
$\Lambda = 14.2$	$\Lambda' = \gamma^{-1/2} \Lambda$
$\Gamma = 49.9$	$\Gamma' = \gamma^{-1} \Gamma$

Figure 3.16: Parameter values for uncompressed and compressed tissue.

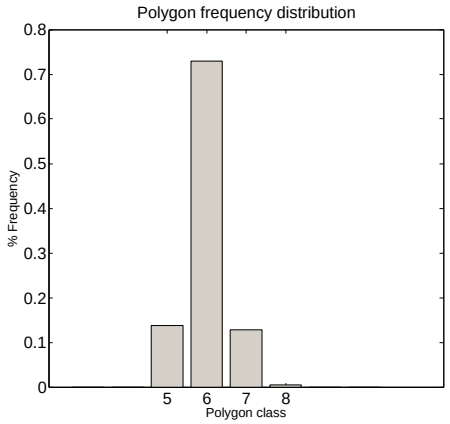

Figure 3.17: The distribution of polygons for the final configuration; Cell number, 196.

3.9 Anisotropy and cell delamination

The first set of simulations tests whether there is a correlation between anisotropy and higher cell delamination. To model anisotropy, the initial condition is affinely scaled in such a way to produce the average cell aspect ratio of 2.7:1, as measured in live tissue (see Figure 3.18). The total area of the tissue, as well as the individual cell areas are invariant under this transformation.

Figure 3.19 summarises the results of this set of simulations. We find that the tissue which starts in an anisotropic state experiences more cell delamination. Furthermore, as cells rearrange and delaminate, the tissue evolves towards an isotropic geometric state. The topology also changes - as can be seen from Figure 3.17. The polygonal distribution changes towards a more regular hexagonal network. This is consistent with the ground state of the work function, which is the hexagonal lattice for the chosen parameter values (as studied in [36]).

To summarise the effects of cell mechanics:

1. If a tissue is undisturbed (by cell divisions, for example), it evolves towards a hexagonal network.

2. However, cell divisions increase the work function of the junctional network and this drives the tissue away from the equilibrium configuration. For this reason, tissues with ongoing cell division are expected to have a polygonal distribution similar to that in Figure 3.15.

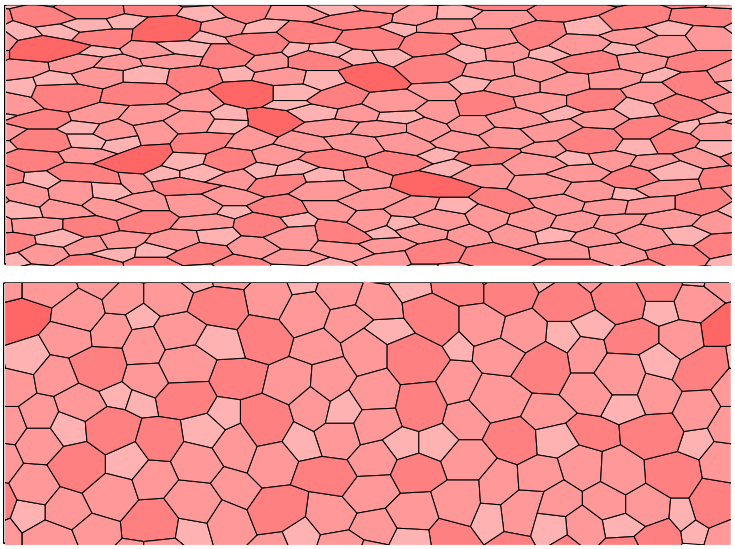

Figure 3.18: Tissue evolves towards an isotropic state; Stills show initial and final cell configurations for the midline simulation.

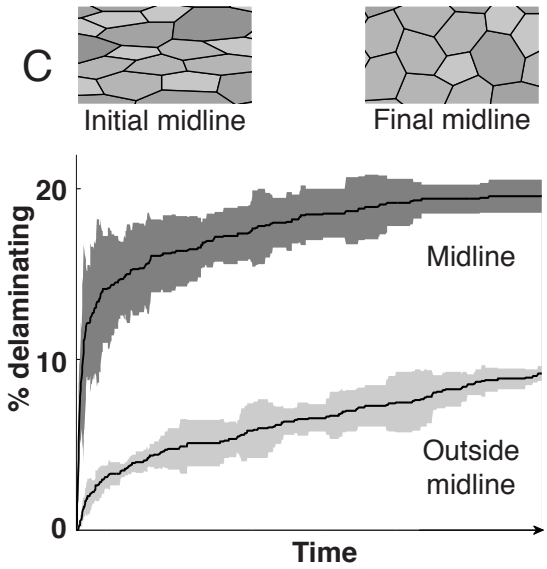

Figure 3.19: The effect of cell geometry on delamination. Stills show initial and final cell configurations for the midline simulation; values of parameters correspond to the wildtype tissue.

The more uniform the spatio-temporal pattern of cell division, the more the junctional network should resemble the equilibrium configuration in Figure 3.15.[1] Tissues in which cell division is absent are expected to evolve towards a hexagonal lattice, as illustrated by the polygonal distribution in Figure 3.17.

3.10 Tissue compression and cell delamination

The next set of simulations tests if there is a correlation between compression and higher cell delamination. In the *in vivo* system, compression may be caused by external forces, or by overcrowding of the tissue due to fast cell growth.

We quantify the degree of compression by a parameter γ. Compressed tissue is modeled by changing the values of the parameters as indicated in Table 3.16; these new parameter values correspond to a tissue that would have the same value of the work function, and hence the same equilibrium configuration, were it free to expand so that its total area was larger by a factor of γ. In Figure 3.20, simulations are performed for the case of high compression corresponding to $\gamma = 4$, for the wildtype corresponding to $\gamma = 2$, and for the no compression case for which $\gamma = 1$.

In these simulations, high compression resulted in high delamination, while low growth rates reduced delamination.

Finally, we combined the two effects in a single simulation, where we compare an anisotropic and highly compressed tissue as in the midline and an isotropic tissue with the wildtype value of compression, as in the surrounding tissue. The total delamination count is shown in Figure 3.21, and it correctly describes the *in vivo* cell behaviour.

Thus, mechanical delamination provides a way to:

1. decrease anisotropy across the tissue

2. decrease the pressure which arises from cell growth.

[1] In fact, the precise values for the equilibrium frequencies depend on the details of cell division, such as the orientation of the mitotic spindle (Nagpal et al [65] and Patel et al [66]). The orientation of the mitotic plane may however depend on the mechanical properties of the neighbouring cells (Théry et al [67]).

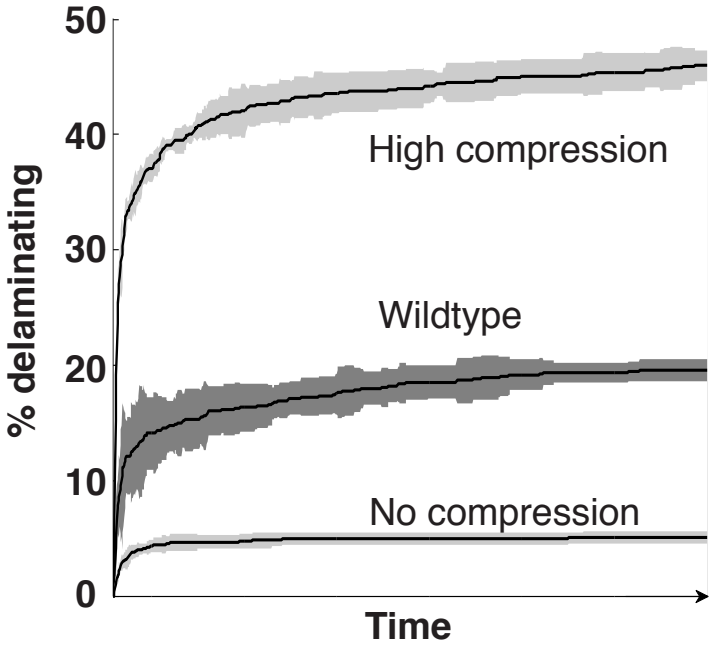

Figure 3.20: Cumulative proportion of cells delaminating from wildtype tissue (midline) and a tissue with high or low growth as a function of time. Data was averaged over 6 simulations.

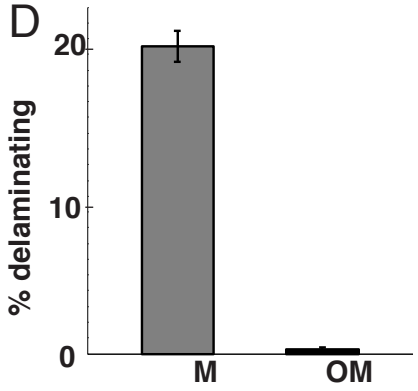

Figure 3.21: Combined effects of compression and anisotropy

3.11 The novel mechanism of cell delamination, induced by mechanical forces

At this stage, it is in order to ask whether compression-dependent cell delamination is perhaps a type of apoptosis. To learn the details of the process of delamination and why it responds to mechanical cues so strongly, a series of experiments were performed.

Firstly, DIAP1 was used to suppress apoptosis in the tissue. This resulted in a small but reproducible decrease in the number of delaminating cells, as shown in Figure 3.22. The effect was seen both in the midline region, and in the surrounding tissue. This implies that the majority of delaminating cells do not in fact undergo apoptosis, but leave the tissue triggered by something else. Further experiments confirm that delamination occurs even when apoptosis is blocked, as seen in Figure 3.23.

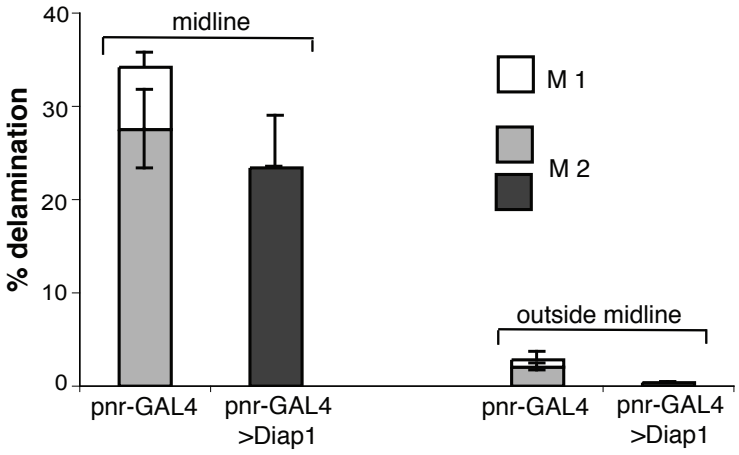

Figure 3.22: Blocking apoptosis results in a decrease of the delamination rate.

Interestingly, on closer look of the details of cell delamination, two distinct patterns can be identified. As seen in Figure 3.24, cells can behave quite differently. In the first panel, the cell leaves the tissue by progressively losing junctions. It starts off as a 7-sided cell, and it gradually loses neighbours with the concurrent decrease of its area. After about 30 min, it has only 4 neighbours and a small area, and this is when it begins to leave the tissue. It takes further 10 min for it to be fully extruded basally.

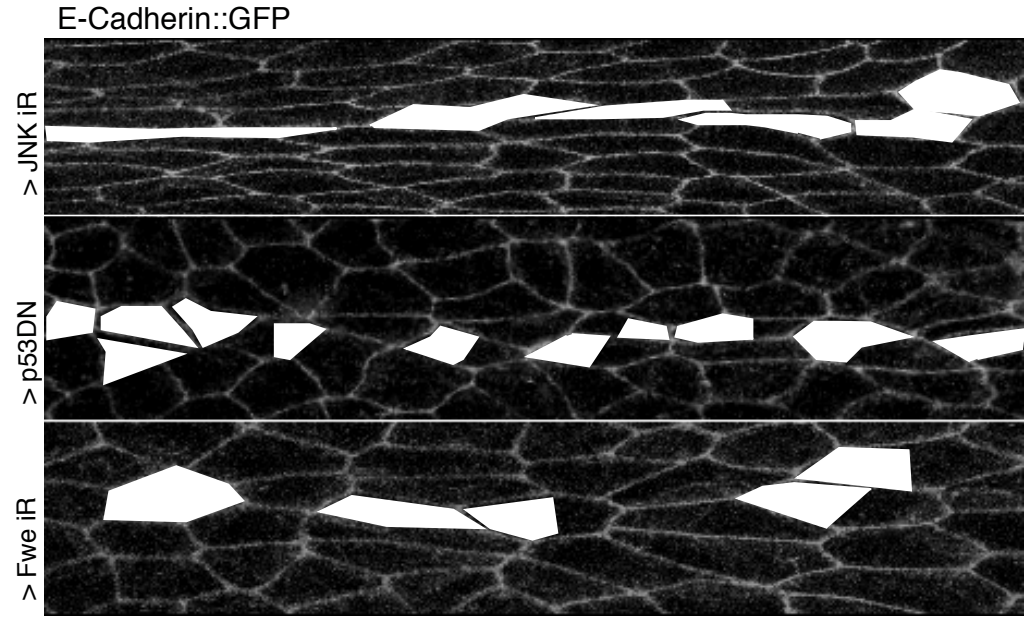

Figure 3.23: As expected for a process independent of apoptosis, delamination from the midline continued unabated in nota expressing RNAi targeting JNK, p53 and Flower. Z-projection of midline region from JNK RNAi, p53DN and Fwe RNAi expressing tissues. Cells delaminating over 12h are colored in white.

In the second and third panels, the delaminating cell does not lose junctions until their area is only a small fraction of the initial area. It is squeezed out of the tissue over a timeframe of 40 min, and this happens without neighbour exchanges. The signature topology of this type of delamination is the formation of a rosette - a vertex where more than 3 cells meet, following full cell extrusion.

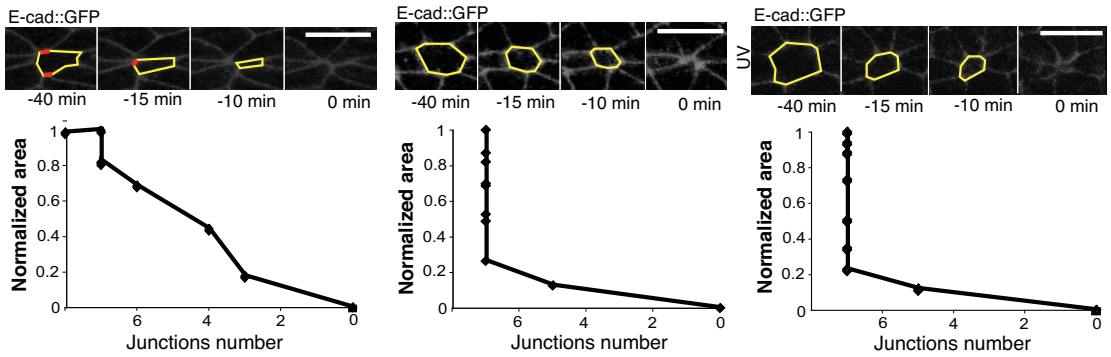

Figure 3.24: Two modes of epithelial delamination, Scale bars, $10\mu m$.

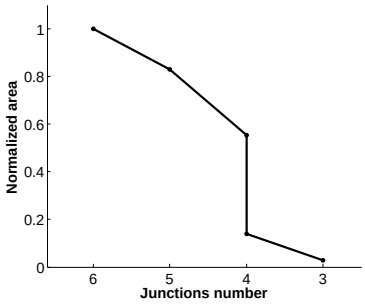

Figure 3.25: Mechanically induced epithelial delamination in the model.

To further probe into the details of this process, the tissue was irradiated with UV rays. This resulted in a dramatic increase in cell delamination. Moreover, it was the rosette-forming type of delamination that was increased, as seen in Figure 3.26. Therefore, the rosette-forming type of delamination is cell death related extrusion, whereas the junction-losing type of delamination is independent of cell death. Considering all the presented data on the dependence of cell delamination rate on the strength of the mechanical forces, the junction-losing type of delamination could be driven by the mechanical forces.

In the vertex model, junctions randomly shorten and lengthen, and as a result of this, cells exchange neighbours. Some cells spontaneously lose junctions and delaminate - purely in response to mechanical forces. For the tissue under compression, this releases overcrowding and the delamination rate decreases and eventually stops as the tissue reaches equilibrium.

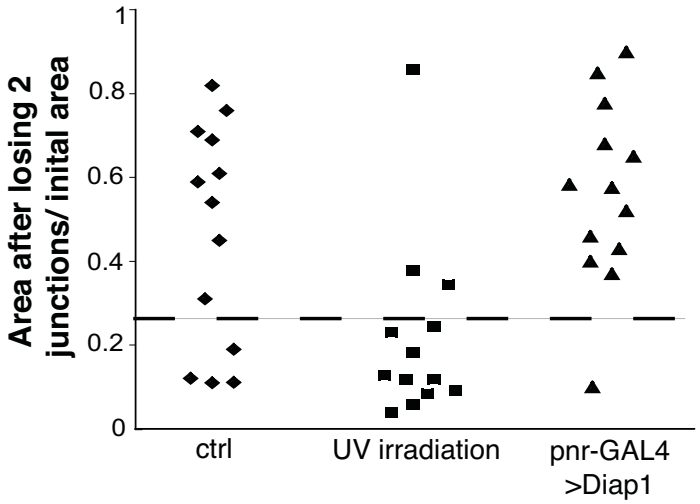

Figure 3.26: Two modes of epithelial delamination

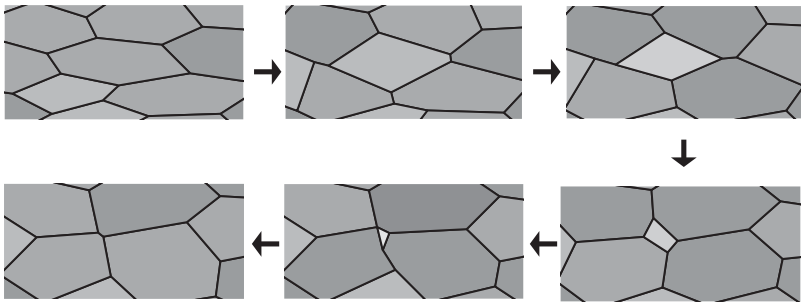

Figure 3.27: As a cell is extruded, it progressively loses junctions as its apical area diminishes.

Interestingly, the junction-losing type of delamination *in vivo* is very similar to the type of cell delamination seen in the mechanical model. First in crowded regions of the notum cells lost individual junctions via a series of neighbour exchanges followed

by the concurrent loss of apical cell area over an extended and variable period, as seen in simulations in Figure 3.27. Data is shown in Figure 3.28 and the correlation between junction number and cell area for a cell in the model is shown in Figure 3.25. However, although the time that it took cells to lose neighbours was variable, once they had fewer than 5 neighbours and an apical area smaller than 25% of the initial apical area, all cells underwent a similar process of extrusion within a short and reproducible timeframe of 10 min.

It is telling that this transition from a variable phase of junctional loss to rapid basal extrusion happens simultaneously with the recruitment of Myosin-II to form a ring within the neighbors of the delaminating cell, as shown in Figure 3.29.

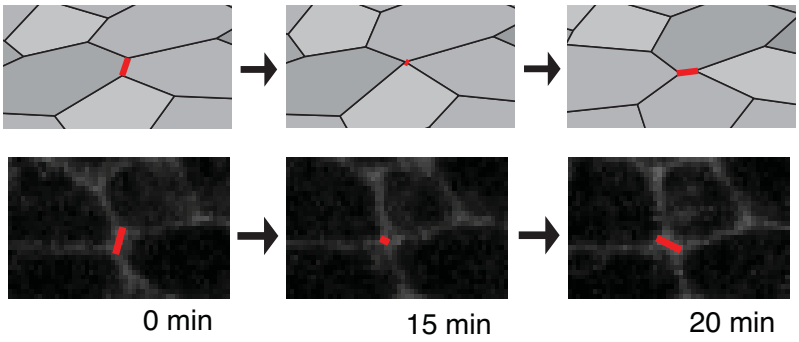

Figure 3.28: The process of neighbour exchanges is a necessary step in cell rearrangements that lead to tissue organisation.

Therefore, we find that most cells delaminate from the tissue while still alive and that *cell death is a consequence, and not a cause of their delamination.* After they have been extruded basally, first by a series of neighbour exchanges, simultaneous with the loss of apical area, and followed by rapid extrusion through recruited Myosin-II, the cells start to die underneath the epithelium. It is important to stress that cell nuclei become visibly condensed and pyknotic only after they have lost their entire apical domain, as seen in Figure 3.30. They are subsequently engulfed by circulating macrophages, as seen in Figure 3.31.

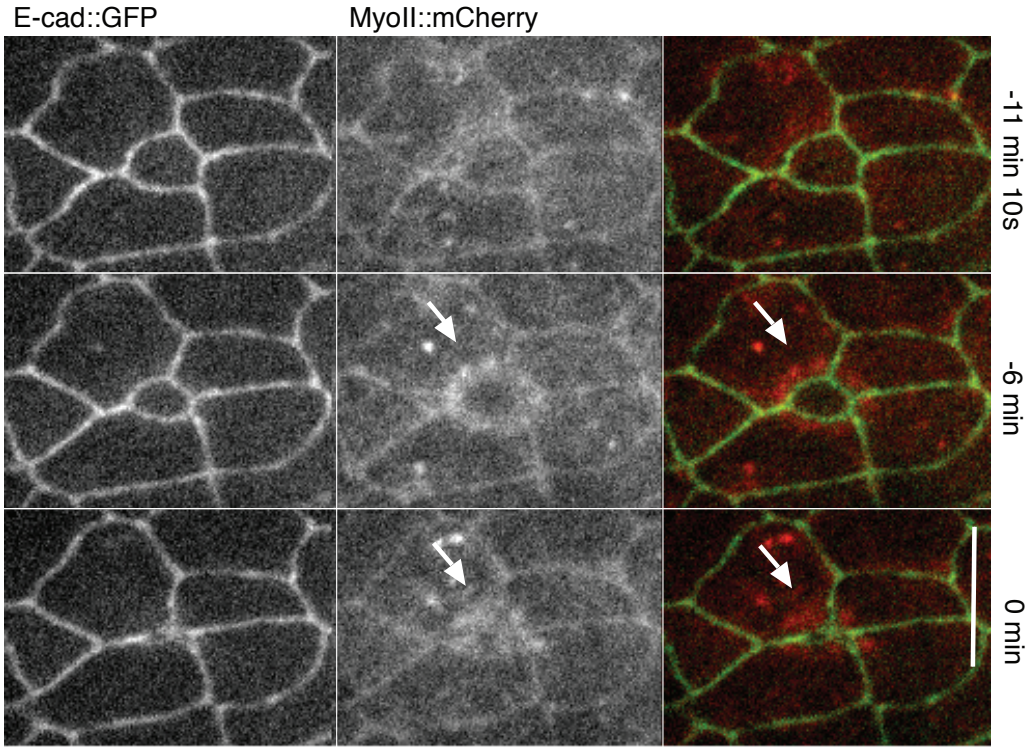

Figure 3.29: Tissue marked with E-Cadherin::GFP and MyoII::Ch. MyosinII ring is indicated by the arrows. Scale bar $10\mu m$.

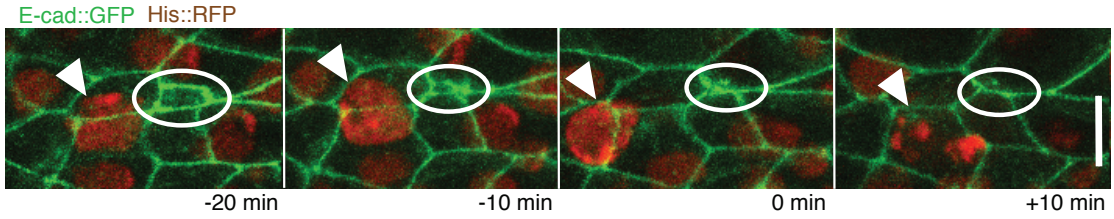

Figure 3.30: The image shows a delaminating cell marked with E-Cadherin::GFP and His::RFP. Its apex (white circle) and nucleus (arrowhead) are indicated. Scale bar $10\mu m$.

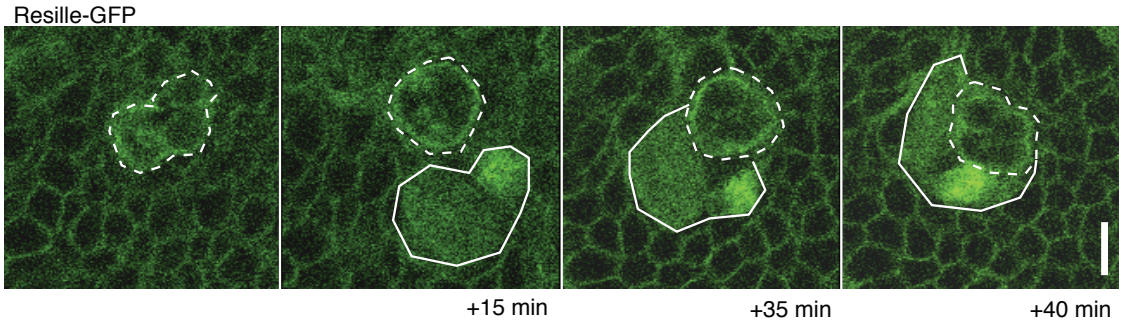

Figure 3.31: Delaminated cells are rapidly phagocytosed by circulating macrophages from the basal side of the epithelium. Timelapse of basal side of the tissue imaged with Resille::GFP. A cell extruded from the tissue is blebbing (indicated by the dashed line). The cell is phagocytosed by a circulating macrophage (indicated by the white line). Scale bar, $10\mu m$.

3.12 Discussion

This study presents definitive evidence of the role of mechanics in tissue homeostasis. Aegerter-Wilmsen et al ([60]) demonstrate a link between epithelial topology and the effect of mechanical force on the rate of cell division. Hence, even though there is a significant amount of work indicating the role of mechanics in epithelial growth and homeostasis, our work is, to our knowledge, possibly the first to show directly that mechanical stress is involved in maintaining homeostasis.

Furthermore, this study identifies a novel homeostatic process - live cell delamination driven by mechanical stress in the tissue and effected through a series of neighbour exchanges. Cells in overcrowded regions of the tissue are subject to stronger compressive force, and cell competition for space drives some of them to lose neighbours. When a cell has fewer than 5 neighbours and a small apical area, the tissue quickly extrudes it through the mobilisation of a myosin ring in its nearest neighbours. In this way, cell density can be tuned through a type of negative feedback process, and persistent overcrowding is avoided. Therefore, tissue growth is buffered against excessive variation in cell density, providing for a robust control of tissue organisation on possibly large scales. Hence, although mitotic rates may not be perfectly tuned to produce an isotropic and homogeneous tissue, tissue stresses may be sufficient to effectively anneal the tissue and ensure robust growth and homeostasis. Since local variations in cell density are detrimental to the accuracy of a variety of tissue pattern-

ing mechanisms, such as those mediated though Delta - Notch signalling (Cohen et al [68]), it is paramount for an epithelial tissue to have efficient control over variations in local cell environment, and live cell delamination induced by compression is an energetically cheap and effective such mechanism.

Chapter 4

Junctional Contractility as an Agent of Tissue Organisation

4.1 The reduced area as a proxy for describing the order of tissues

Tissue order is the triumph of self-organising processes directing growth and development. It is still unclear how tissue order arises and how it is maintained throughout the lifetime of the epithelium. This chapter presents a theoretical study of tissue order within the formalism of the vertex model. During pupal development, the morphology of the ventral mesothorax of Drosophila Melagonaster changes. One feature is that there are several rounds of divisions during this period, resulting in an increase in the total number of cells. The overall size of the tissue remains fixed. As a result of this, the apical surface of the cells decreases. Quite a few cells leave the tissue to be recycled underneath the epithelial layer. However, the number of cells that leave the epithelium is small in comparison to the number of cells that divide, and therefore the overall number of cells in the tissue increases.

The second striking feature of pupal development is that the cell packing changes. As time passes, the apical view of the cells start to resemble a regular hexagonal lattice. It is an open question so as to how this is orchestrated and achieved.

In [44], the authors show that the level of "order" in a network of polygons[1]

[1]A network of polygons is a simplification of the cell shape commonly used to study epithelial tissues.

is strongly related to the geometric properties of individual polygons. They point to a relationship between a single geometric parameter and the polygonal packing. Defining the *reduced area* of a polygon as follows:

$$a = \frac{4\pi A}{L^2}, \tag{4.1}$$

where A is the polygon area and L is the polygon circumference, they find that the increase in a forces the polygonal network to become 'more ordered'. At $a = a_c = 0.865$, the system undergoes a disorder-order transition, so that for $a > a_c$, the network becomes a regular hexagonal lattice. For $a < a_d = 0.785$, the network is disordered, and the frequency of a given polygon weakly depends on a. For the intermediate values $a_d < a < a_c$, the frequency of hexagons is increasing with the increase in a.

Linking a to the physical parameters Λ and Γ used to describe tissues in physical models (lattice models [6] and vertex models [36] as well our vertex model) provides an insight into a possible mechanism of organisation during tissue development.

4.2 A link between cell division and the ordering of tissues

There are several rounds of cell divisions in the notum during the course of pupal development. The notum does not grow during this process and the apical area of the daughter cells is generally equal to the half of the parent apical area. What does this scaling mean for the organisation and the ordering of the tissue?

As cells divide within a tissue of a fixed size, the average cell area decreases, as well as the average junction length. Since we have seen that the dimensionless ratio of cell area and the square of the perimeter length indicates the level of order within the tissue, it is interesting to consider what happens to the reduced area a as cells divide.

The equation for the work function defines the **lengthscale** $l_0 = -\frac{\Lambda}{\Gamma}$:

$$W = \sum_{\alpha} \frac{K}{2}(A_\alpha - A_0)^2 + \sum_{ij} \frac{\Gamma_{ij}}{2}(l_{ij} - l_0)^2.$$

We will also explore how the work function should be adjusted so that the lengthscale

l_0 is appropriate for both the parent and the daughter cells.

4.2.1 Tissue at $a_{target} = a_6$

The fixed size of the tissue may have an effect on equilibrium tissue properties. We monitor the state of the tissue with the target reduced area a_{target} equal to the reduced area of the regular hexagon $a_6 = 0.907$, and release the constraint for the finite size of the tissue. Hence initially $A_{tissue}(0) = A_0 \times N_{cell}$, but afterwards $A_{tissue}(t)$ is allowed to vary according to the Metropolis algorithm (as described in Chapter 2, Section 2.9.3). The stills showing the evolution are shown in Figure 4.1.

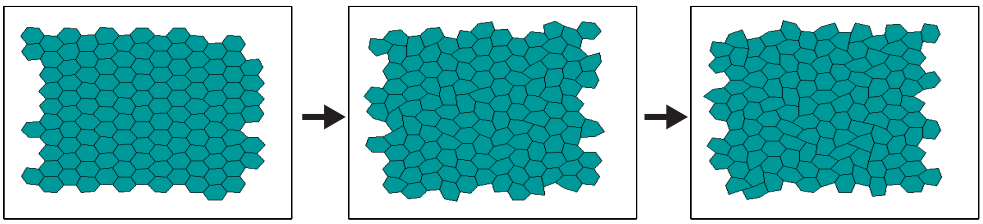

Figure 4.1: Evolution of the tissue with a free boundary.

We can conclude that releasing the constraint of fixed tissue size has a minimal impact on the size and the shape of the tissue. Therefore we continue with the study of equilibrium states calculated for the unconstrained tissue, whilst we constrain the size of the tissue, assuming that the fixed size of the tissue in itself does not have a strong impact on equilibrium states. Therefore, we assume that the phase diagram obtained for the unconstrained tissues (Figure 2.2) is a good approximation for the phase diagram of the constrained tissues.

4.2.2 A single round of divisions with no change in Λ and Γ

We study the tissue undergoing a single round of cell divisions, with the following rule for the change in parameters:

$$A_0^{daughter} = \frac{1}{2} \times A_0^{mother} \tag{4.2}$$

$$\Lambda^{daughter} = \Lambda^{mother} \tag{4.3}$$

$$\Gamma^{daughter} = \Gamma^{mother} \tag{4.4}$$

Therefore, the target reduced area of the daughter cells can be calculated as follows:

$$a_{target}^{daughter} = a_{target}^{mother} * \frac{\frac{1}{2}}{1} = a_{target}^{mother} \times 0.5,$$

since the target junction length for an edge with parameters Λ and Γ is equal to $\frac{-\Lambda}{\Gamma,}$ and every daughter cell have 6 junctions, on average. It will have 5 sides created after division, on average, and it will gain 1 side, on average, from the divisions of its nearest neighbours. This is Lewis' law (Lewis [69], Lewis [70], Graustein [71]) which states that the average polygon number in a polygonal tiling obtained from a regular hexagonal tiling through cell divisions is 6.

Thus we conclude that the target reduced area of the daughter cell is smaller than the target reduced area of the mother cell by a factor of 0.5. Referring back to Figure 1.13, and noting that a decrease in a results in the increase in tissue disorder, we expect to see an increase in disorder even after a single round of divisions. We simulate this situation by setting the parameters as in Equations 4.2 - 4.4. As seen from the stills shown in Figure 4.2, disorder does indeed increase as cell divisions proceed, for these values of daughter cell A_0, Λ and Γ.

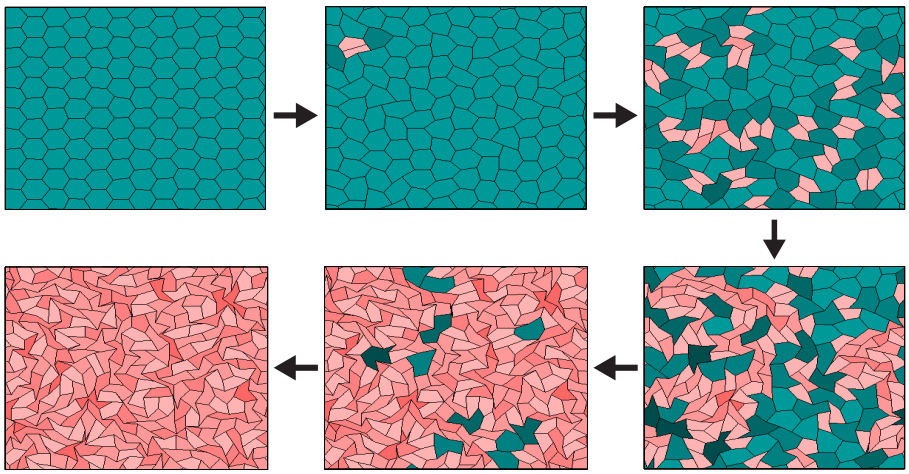

Figure 4.2: A single round of cell divisions with $\Gamma^{daughter} = \Gamma^{mother}$.

4.2.3 Mechanical scaling of Λ and Γ

Next, we check how Λ and Γ are in fact expected to scale with junction length, on physical grounds. Since the work function is linear in line tension Λ, the instantaneous force due to line tension is equal to Λ and it does not depend on junction length. Therefore, we expect Λ to be the same for junctions of different lengths, and it should only depend on the structural properties of cell-cell contacts such as the density of adhesive junctions, and not on the total length of the junction. Hence:

$$\Lambda^{daughter} = \Lambda^{mother}.$$

On the other hand, contractility Γ should depend on the junction length. Since in the model, the contractility of the junctions is described by Hooke's law for elastic springs, if we take this analogy further, we expect that the spring constant Γ scales inversely proportionally with the spring length.[2] Therefore:

$$\Gamma^{l/2} = \frac{1}{2}\Gamma^{l}.$$

Figure 4.3 shows the idealised situation of a regular hexagonal polygon dividing into two "daughters" according to the cell division algorithm used in our model. The junction length of the hexagon is l and its area is $A = \frac{3\sqrt{3}}{2}l^2$, giving the reduced area $a = 4\pi\frac{A}{(6l)^2} = 0.907$.

The daughter cell area is equal to a half of the mother area, and the daughter perimeter is equal to $\frac{3l+l\sqrt{3}}{6l} = \frac{3+\sqrt{3}}{6}$ of the mother perimeter, as seen from the diagram.

Since the total perimeter of the daughter cell is initially, on average, equal to $\frac{3+\sqrt{3}}{6}$ times the perimeter of the mother cell (as seen from the diagram in Figure 4.3), so the average "spring constant" of the junctions Γ should scale by the inverse of this factor:

$$\Gamma^{daughter} = \frac{6}{3+\sqrt{3}}\Gamma^{mother} = 1.268 \times \Gamma^{mother}.$$

[2]Compare, for example, the law for springs connected in series $1/k_1 + 1/k_2 = 1/k_{series}$.

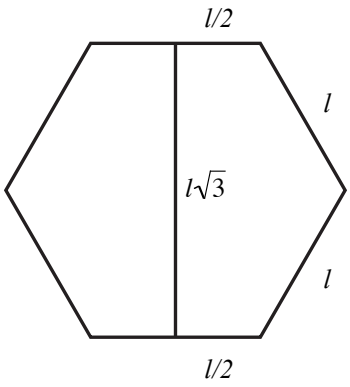

Figure 4.3: The perimeter of the daughter cell is equal to $\frac{3+\sqrt{3}}{6}$ times the perimeter of the mother cell.

Therefore, the next natural scaling of the parameters A_0, Λ, Γ to consider is:

$$A_0^{daughter} = \frac{1}{2} \times A_0^{mother} \quad (4.5)$$

$$\Lambda^{daughter} = \Lambda^{mother} \quad (4.6)$$

$$\Gamma^{daughter} = 1.268 \times \Gamma^{mother} \quad (4.7)$$

The target reduced area scales as follows:

$$a_{target}^{daughter} = a_{target}^{mother} * \frac{\frac{1}{2}}{\left(\frac{3+\sqrt{3}}{6}\right)^2} = a_{target}^{mother} \times 0.804.$$

Since the target reduced area decreases in this case as well, we again expect to see an increase in tissue disorder after a single round of cell divisions, although to a lesser degree than the disorder in the previous case, as a here decreases only by 0.80, compared to the previous decrease by 0.50.

We simulate this situation (parameters given by Equations 4.5 -4.7) and the stills are shown in Figure 4.4. It can be seen that the tissue does indeed disorder, but also does so to a lesser extent than it did in the previous case (cf. Figure 4.2).

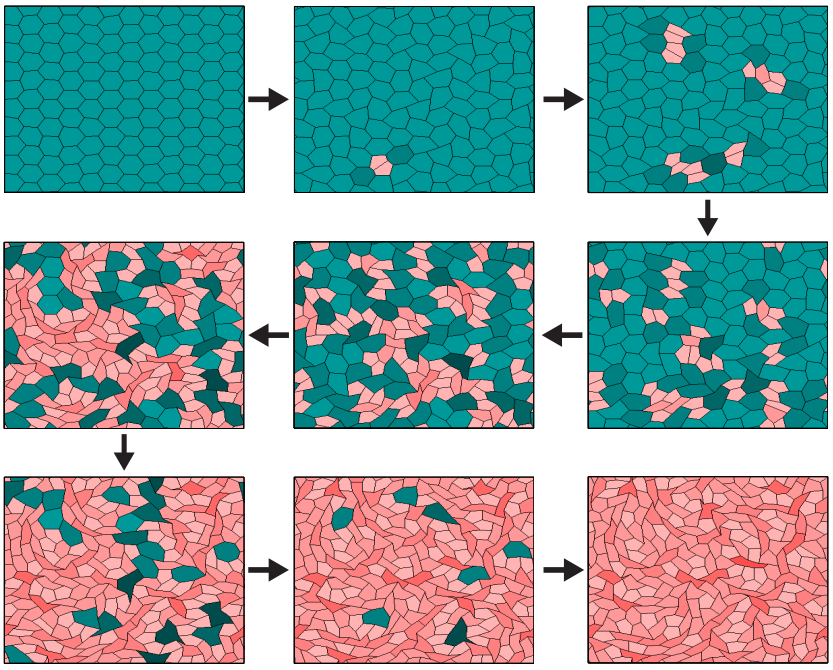

Figure 4.4: A single round of cell divisions with $\Gamma^{daughter} = \frac{6}{3+\sqrt{3}} * \Gamma^{mother}$.

4.2.4 The scaling of Λ and Γ required to maintain order

In order to keep the reduced area invariant under cell division, which is to say, in order to keep the equilibrium level of order within the tissue constant as cells divide, the parameters should scale as follows:

$$\begin{aligned} A_0^{daughter} &= \frac{1}{2} \times A_0^{mother} \\ \Lambda^{daughter} &= \Lambda^{mother} \\ \Gamma^{daughter} &= \sqrt{2} \times \Gamma^{mother}. \end{aligned}$$

In this way, the reduced area of the daughter cells remains the same as the reduced area of the mother cell:

$$a_{target}^{daughter} = a_{target}^{mother} * \frac{\frac{1}{2}}{(\frac{1}{\sqrt{2}})^2} = a_{target}^{mother}.$$

It is important to stress that the tissue order as understood in this chapter is the **equilibrium tissue order**. That is to say, cell divisions are expected to induce

disorder in the tissue under any circumstances, since they disturb the tissue away from the equilibrium by actively inputting energy. However, cell divisions disturb the tissue only temporarily, since the values of the physical parameters ultimately determine the equilibrium states. Therefore, cell divisions temporarily disturb the tissue from equilibrium, but the mechanical forces eventually return it to the state of mechanical equilibrium. It is this mechanical equilibrium state that we are referring to when we measure the order of the tissue as predicted by the target reduced area. Therefore, for the tissue for which $a_{target}^{daughter} = a_{target}^{mother}$, the mechanical equilibrium states should be **identical** before and after the cell divisions, provided the tissue has had enough time to equilibrate. Clearly, there will be a lot of intermediate disordered states as cell divisions proceed, however, the final equilibrium state is identical to the initial equilibrium state. This is in contrast to the tissue for which the target reduced area changes as cell divisions proceed. For these tissues, transient disorder induced by cell divisions is only partially removed when the tissue equilibrates. The new mechanical equilibrium will be different from the initial mechanical equilibrium, because the new reduced area is not the same as the initial reduced area. In this case, cell divisions have induced a permanent change in the parameter space in the phase diagram in Figure 2.2, and the new equilibrium state is different. In this way, cell divisions can cause the tissue to "travel" in parameter space.

To illustrate the point that the change in Γ between the mother cell and the daughter cell determines the equilibrium states of the tissue, another simulation was run with the following parameters:

$$\begin{aligned} A_0^{daughter} &= \frac{1}{2} \times A_0^{mother} \\ \Lambda^{daughter} &= \Lambda^{mother} \\ \Gamma^{daughter} &= 2 \times \Gamma^{mother}. \end{aligned}$$

In this case, the contractility of the daughter cell increases *more* than it should if junctions are simply assumed to behave as elastic springs. This could be due to many factors, such as the non-obvious scaling relationship between junctional contractility and the concentration of myosin, size of the cell, presence of medial myosin.

In this case, the target reduced area increases as cells divide, by a factor of 2. Stills illustrating this situation are shown in Figure 4.5. The induced transient disorder is

markedly less pronounced than it is in the previous two cases (Figure 4.2 and 4.4).

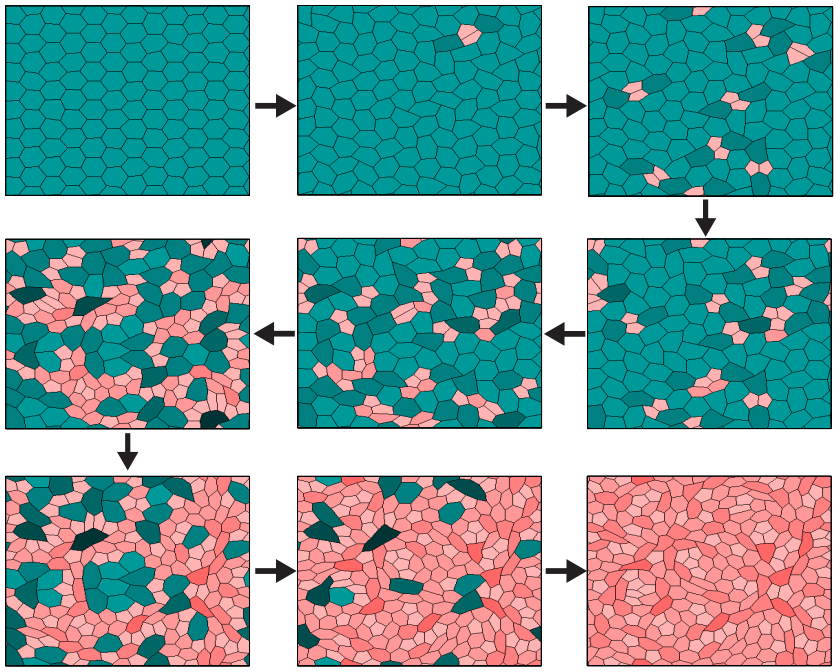

Figure 4.5: A single round of cell divisions with $\Gamma^{daughter} = 2 * \Gamma^{mother}$.

Finally, the message of this study is that tissue order depends strongly on how junctional contractility changes with junction length and with cell generation. If junctions behave as simple elastic springs, so that the spring constant of a half a junction is equal to twice the spring constant of the whole junction made of the same material, we see that the tissue would disorder as cell divisions occur. This disorder would change the point in the parameter space, so that the equilibrium states of the tissue would permanently change towards more disordered states.

The situation in the Drosophila notum during pupal development is different. The notum goes through several rounds of cell divisions and the cell packing refines and the tissue becomes more ordered towards the end of pupal development. This should be the case if contractility of daughter cells is greater than $\sqrt{2}$ times the contractility of the mother cells. Looking at data in Figure 3.7 and 3.8, we see that junctional tension changes by a factor of 2 when comparing cells in early pupal development and in late pupal development. This increase in contractility is consistent with the fact that the tissue orders during this period, even as two rounds of cell divisions occur.

4.3 Discussion

It was previously suggested (Farhadifar et al [36]) that a growing Drosophila wing disc is in a state of polygonal disorder throughout most of its development. Towards the end of its larval development, this tissue undergoes a process of repacking and reordering, in order to emerge in an ordered state closely resembling the regular hexagonal lattice. It was also suggested that this occurs concurrently with the onset of activity of the planar cell polarity pathway.

Since the presented study illustrates how changes in junctional contractility modulate tissue order, it would be very interesting to check whether the activity of the planar cell polarity pathway has a direct effect on junctional contractility, and thus whether it increases tissue order by tuning the target reduced area.

Chapter 5

Convergent Extension

5.1 Introduction

Convergent extension is a morphogenetic event during which a tissue extends in length and narrows in width (Baum [72]). It is a conserved event which occurs during gastrulation, neurulation, axis elongation and organogenesis in both vertebrate and invertebrate embryos, and it generates one of the most interesting features of embryonal development: the elongated body axis.

Convergent extension is achieved through coordinated rearrangements of cells, more specifically, through a process termed *cell intercalation* (Irvine and Wieschaus [73]). Intercalating cells change positions relative to each other in a coordinated way, which results in the lengthening and narrowing of the whole tissue. Intercalation is effected through a series of coordinated T1 transitions, as shown in Figure 5.1.

It is believed that spatial clues that direct cell movements during intercalation come from local cell-cell contacts (Lecuit and Lenne [74], Lecuit [75]). Internal cellular architecture becomes polarised during convergent extension. In particular, proteins which affect adhesion and contractility enrich in specific cortical domains. (Bertet et al [76], Zallen and Wieschaus [77], Kasza and Zallen [78]).

Intriguingly, intercalating cells in the *Drosophila* germband form rosette-like structures, as reported by Blankenship et al [79], and shown in Figure 5.2. Moreover, the direction of rosette formation and resolution is not random, but biased in a way that leads to tissue elongation.

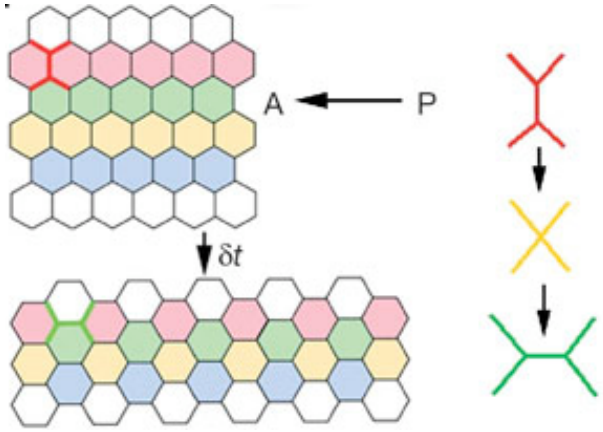

Figure 5.1: Cells exchange neighbours in a defined direction, and this results in a change in tissue aspect ratio. This process is called *cell intercalation* (Adapted from Bertet et al [76]).

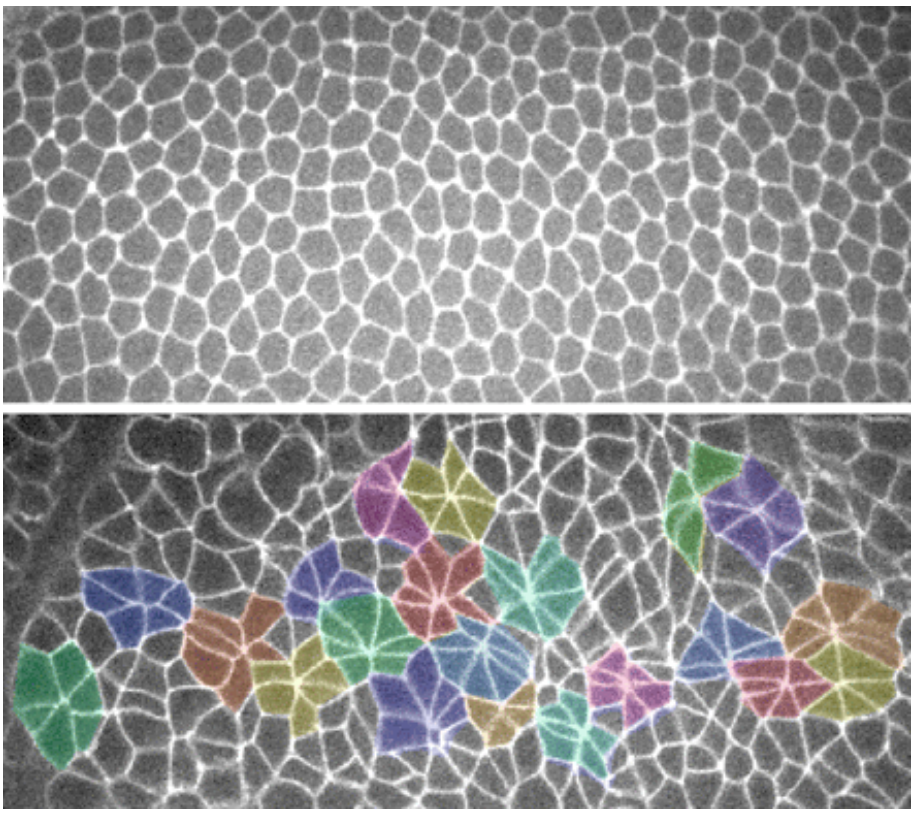

Figure 5.2: A *Drosophila* epithelium before and during embryonic elongation. Rosettes comprising several cells (shown in colours) form during elongation. (Adapted from Blankenship at al. [79].)

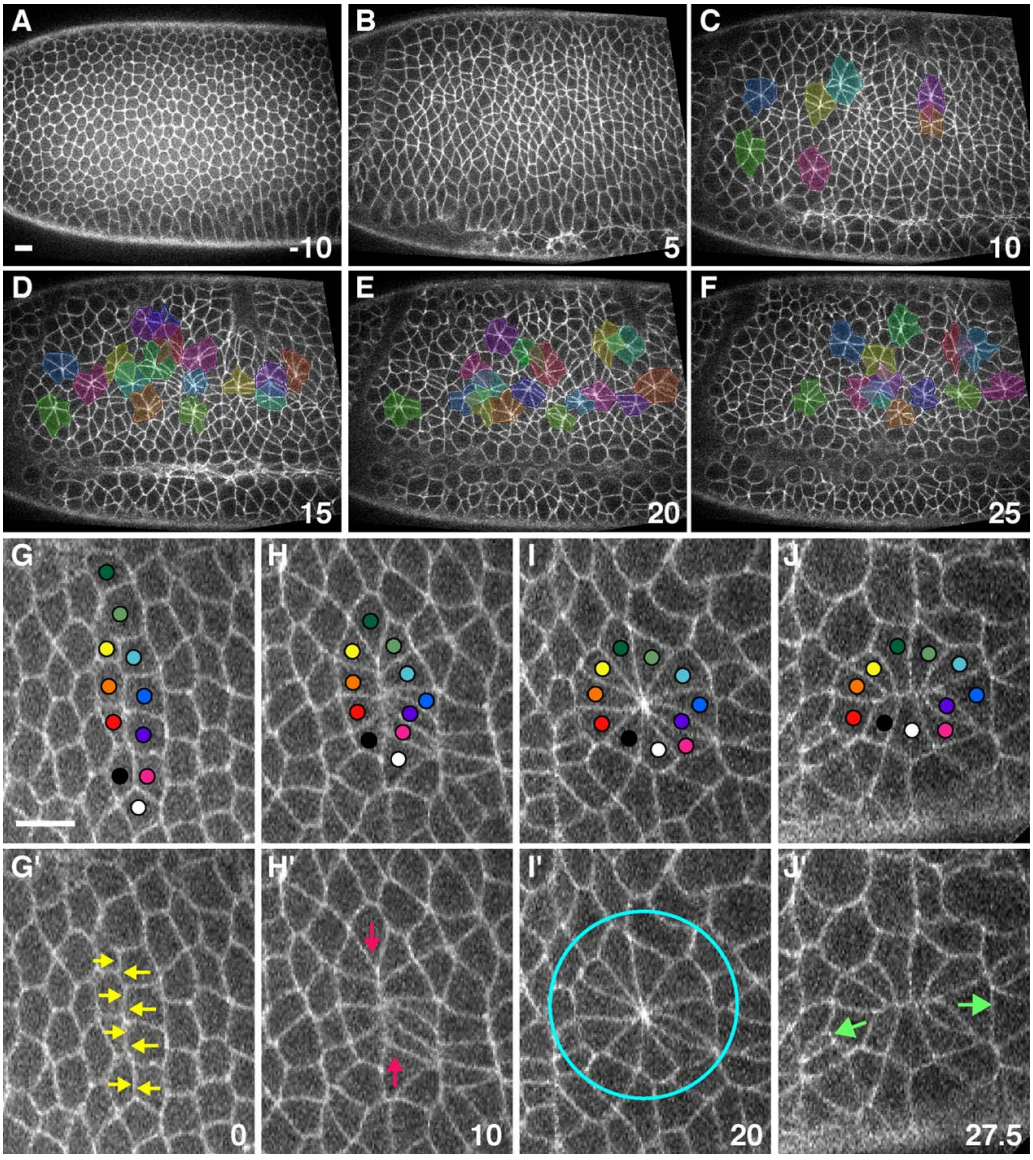

Figure 5.3: Rosettes form as vertical junctions shrink to a vertex shared by several cells, and rosette vertices resolve horizontally. (Adapted from Blankenship et al [79].)

Previous models of convergent extension (Zajac et al [81]) have focused on showing that an anisotropy in cell-cell interface tension is sufficient to drive a change in tissue shape. We examine whether mechanical forces associated with the polarised proteins can account for both the formation and the resolution of the rosettes. Our approach is to study the plausibility of the proposed mechanical scenario, in order to compare it to experiment and decide how well it fits the *in vivo* realisation.

5.2 Cells polarise during convergent extension

During convergent extension, Myosin II is polarised so that its concentration is higher on dorsal-ventral-oriented junctions (Blankenship et al [79], Bertet et al [76]), which are the vertical junctions in the presented figures. Force is generated by Myosin-II motors on actin filaments producing junctional contractility in the vertical direction. These junctions shrink in response to an increase in vertical contractility. Typically, this shrinkage results in the formation of rosette-like structures, in which multiple neighbouring vertical junctions shrink into a single vertex which is shared by as many as 10 cells, as illustrated in Figure 5.3 as reported by Blankenship et al [79]. Furthemore, the authors also report that supra-cellular actin-myosin cables form and align across multiple cells, providing directional information to collections of neighbouring cells.

Rauzi et al [80] study the details of Myosin II enrichment on vertical junctions. Studying the timescales of Myosin II concentration profile changes, they find that the enrichment of junctional Myosin II is gradual and results from the flow of medial Myosin II in the direction of vertical junctions. Furthermore, they suggest that the shrinkage of vertical junctions is effected by medial Myosin and subsequently stablised by the anchoring of inflowing medial Myosin II onto vertical junctions. The relative positions of junctional and medial Myosin is illustrated in Figures 5.4 and 5.5.

5.3 A physical model of convergent extension

We model an epithelial tissue in which Myosin-II gradually recruits on the vertical junctions. Myosin flows towards the vertical junctions and in the process, it shortens the vertical junction lengths (Rauzi et al [80]). Specifically, Myosin-II flows in pulses. However, here we test a simplified scenario in which Myosin-II concentration is grad-

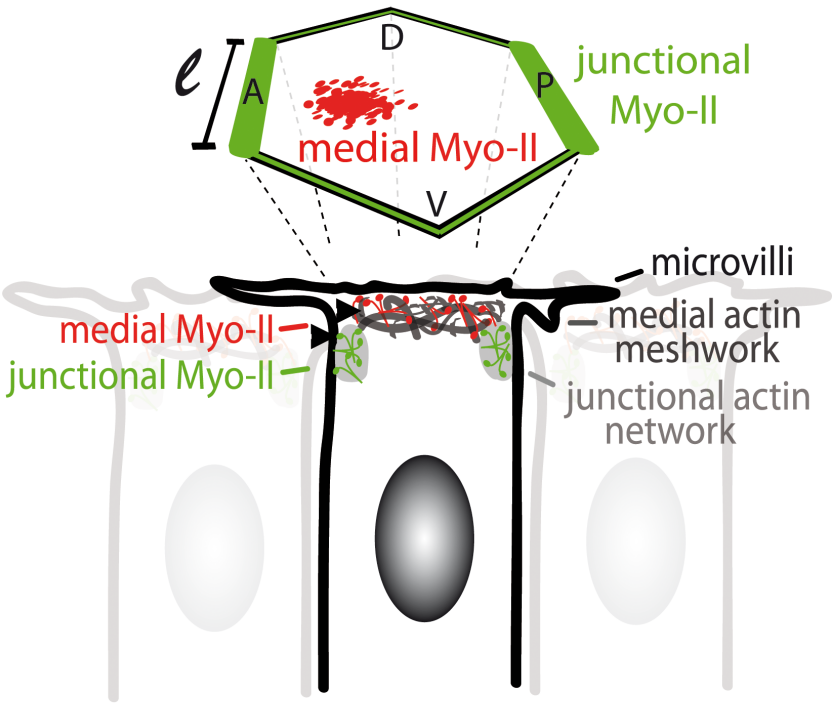

Figure 5.4: Medial and junctional myosin location in the cell. (Adapted from Rauzi et al [80]).

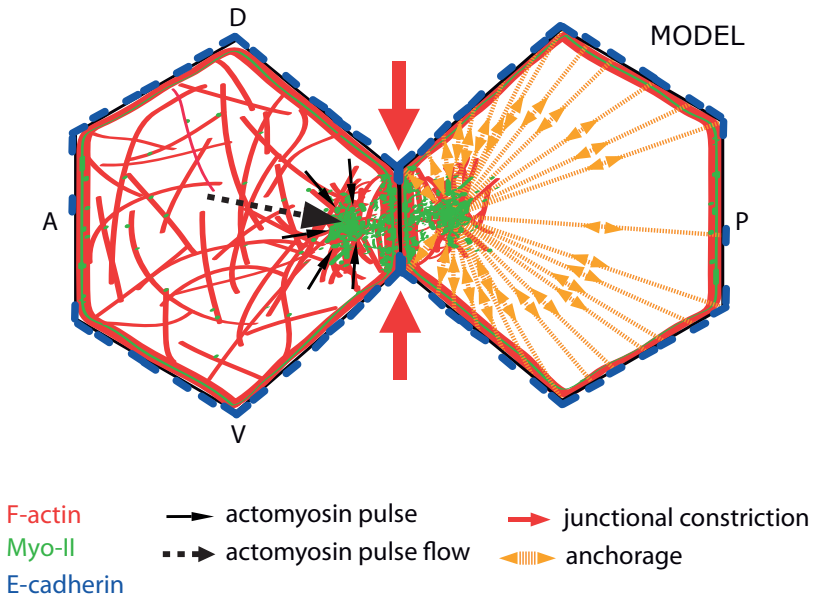

Figure 5.5: Vertical (dorsal-ventral) junctions shrunk by medial myosin and stabilised by junctional myosin. (Adapted from Rauzi et al [80]).

ually increased on the vertical junctions. Simultaneously, Myosin-II is depleted from the horizontal junctions, with the same rate with which it is enriched on the vertical junctions.

We implement the following rule for the change in junctional contractility Γ, which is directly influenced by the concentration of Myosin II:

$$\Gamma_{i+1} = \Gamma_i - \delta\Gamma\cos(2\theta), \text{ if } \Gamma_{min} < \Gamma_i < \Gamma_{max} \quad (5.1)$$

$$= \Gamma_{min} \qquad \text{if } \Gamma_i < \Gamma_{min} \quad (5.2)$$

$$= \Gamma_{max} \qquad \text{if } \Gamma_i > \Gamma_{max} \quad (5.3)$$

Γ_{min} is the lower threshold below which we don't allow the contractility to decrease for any of the junctions, $\delta\Gamma$ is a parameter which determines how fast the recruitment occurs, and θ is the angle which the junction subtends with the horizontal axis. The orientation is such that the x-axis corresponds to the A-P axis and the y-axis corresponds to the D-V axis. We chose this dynamics to mimic the gradual, time-dependant enrichment of myosin on vertical junctions.

We set out to answer the following questions:

1. Is the enriched acto-myosin on the vertical (D-V) junctions sufficient to reproduce rosettes?

2. Does the tissue as a whole change its aspect ratio in reponse to the polarised enrichment?

3. How do the rosettes resolve? Specifically, is an active process necessary to drive the resolutions of the rosettes? Or perhaps junctional contraction elsewhere could cause rosette resolution in the horizontal (A-P) direction?

We define rosettes to be any structures which comprise cells that join at a vertex of order 4 or higher, and have a sufficiently high concentration of acto-myosin at the vertex, such that Γ is greater than a threshold value Γ_{ros}.

Blankenship at al [79] show that Myosin-II accumulates at the shortening vertical junction and remains temporarily at the vertex of a rosette. To take this into account, we assume that the junction which decreased to zero length will keep the high concentration of Myosin-II until this is recycled elsewhere. Therefore, we impose

the following condition on the rosette junctions: The zero-length junction dissipates Myosin-II, and therefore its Γ decreases. The decrease is implemented with the same rule for the change of Γ (Equations 5.3 and 5.3), with the assumption that the zero-length junction has the rate of decrease of Myosin-II equal to that of a horizontal junction. Furthermore, the resolution of a rosette is delayed until some of the Myosin-II has dissipated. This is because we suspect that Myosin-II may be preventing the flipping of the junctions in order to complete the T1 transitions and the data shows that the rosette junctions don't resolve momentarily, but rather tend to persist for several minutes. We impose a lower threshold on Γ of a zero-length junction which must be reached before the rosette vertex is allowed to resolve. We effectively block the movement of the vertices forming the rosette, until the Myosin-II dissipates below the threshold Γ_{ros}. As soon as the Γ of the zero-length junction reaches the threshold, the vertices evolve according to the usual Boltzman dynamics and are free to resolve in any direction.

5.4 Results

Mechanical parameters are set to the same values used in Chapters 2 and 3, and the parameters relating to polarised contractility are shown in Table 5.1. Stills in Figure 5.6 illustrate how tissue evolves.

Table 5.1: Parameters values for the simulation of convergent extension.

A_0	1.30
K	160
Λ	56.8
Γ_{ref}	49.9
Γ_{max}	$4 \times \Gamma_{ref}$
Γ_{min}	0
$\delta\Gamma$	$\Gamma_{ref}/40$
Γ_{ros}	Γ_{ref}

The tissue extends in length and shortens in width, as shown in the stills and quantified by the changing aspect ratio shown in Figure 5.7. The aspect ratio initially increases to about 4 times the initial value, after which it reaches a plateau which could be called equilibrium aspect ratio.

Interestingly, cells change shape to become elongated along the horizontal junctions. Comparing the number of cells in rows and columns at the start and at the end of the simulation, we can conclude that there was not a significant number of intercalation events and the tissue elongation is driven mainly by individual cell elongation in response to differential values of junctional contractility along the vertical and horizontal axes.

The rosette count (Figure 5.7) is very low compared to the *in vivo* tissue (Figure 5.3). The total number of T1 transitions is 250, which is very low compared to the more active tissues studied in Chapter 2 and Chapter 3 (Figure 5.8). Remarkably, there was no single cell delamination event (Figure 5.8). From the equilibrium polygonal distribution (shown in Figure 5.9) we see that the tissue settles into an equilibrium and does not fluctuate at all.

We can conclude that this simulation does not faithfully capture the dynamics of cell intercalation and rosette formation and resolution during convergent extension is *Drosophila*. Directional bias in contractility does indeed drive tissue elongation, but this is mainly the result of individual cell elongation and perhaps related better to the dynamics of vertebrate convergent extension (Concha and Adams [82]) where cell elongation does occur. The tissue is not dynamic enough to allow for varied cell rearrangements observed in the *Drosophila* embryo. This could be because the tissue settles too quickly into a local equilibrium, without exploring the rest of the parameter space.

5.5 High noise

We next study a tissue with an increased level of noise, whilst keeping all the other parameters the same. Higher noise in general allows the system to overcome work function barriers and escape local minima. Parameter values are shown in Table 5.2. In this case, markedly different cell behaviour is observed.

Stills are showing tissue evolution in Figure 5.11. The first difference to note is that in this case the aspect ratio does not plateau, but keeps growing until the layer of cells is 2-3 cells thin, and the model cannot handle further evolution (Figure 5.12), at which point the aspect ratio is greater than $20:1$. We observe signature behaviour of cell intercalation: the number of cells in 'columns' decreases, while the number of cells in 'rows' increases, since the cells exchange neighbours in a coordinated fashion.

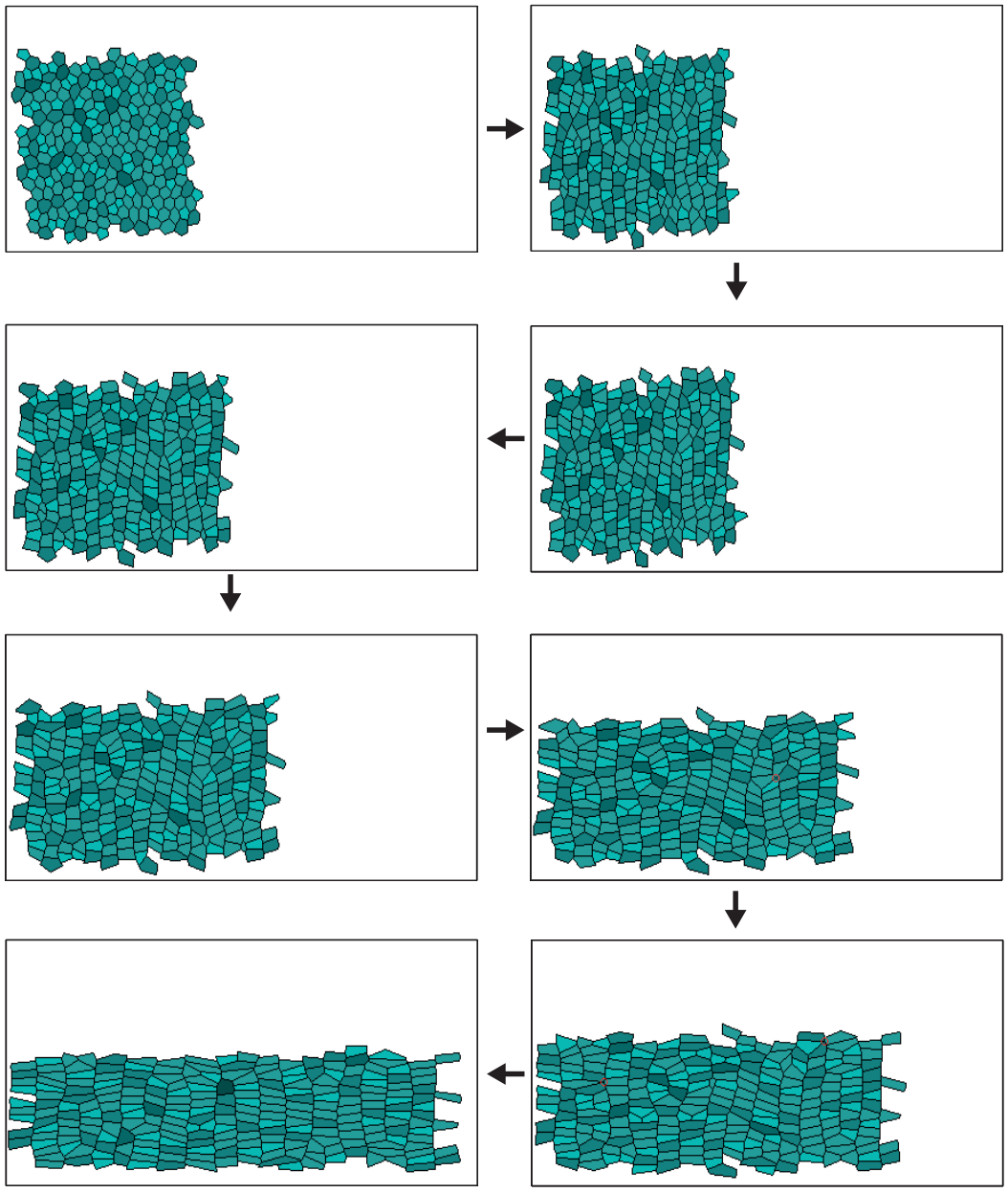

Figure 5.6: Stills showing evolution of tissue with low noise. Tissue aspect ratio changes to approximately 4 : 1. Individual cells elongate. Rosettes form only rarely (encircled in red).

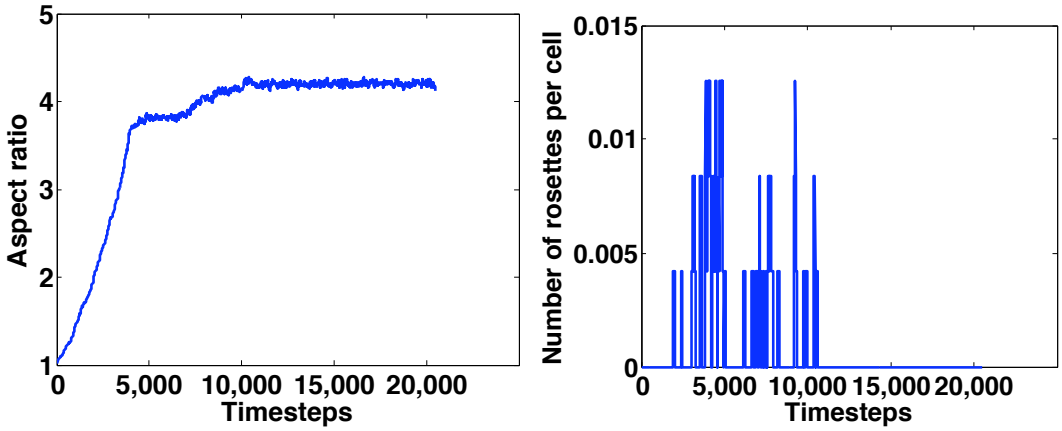

Figure 5.7: (Left) The aspect ratio changes as the tissue elongates when a directional bias in contractility Γ is introduced. (Right) Very few rosettes form in the process.

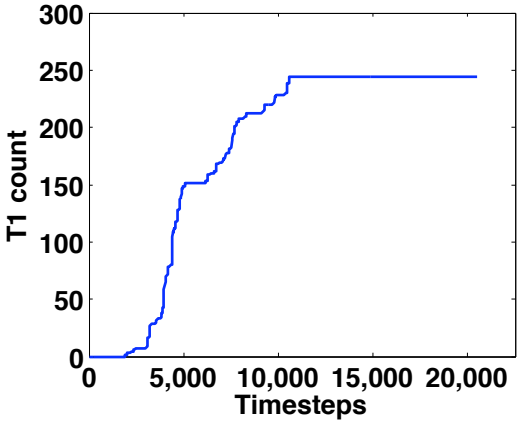

Figure 5.8: Cumulative distribution of T1 transitions. No T2 transitions occur during evolution of tissue with low noise.

Table 5.2: Parameters values for the high noise simulation of convergent extension.

A_0	1.30
K	16.0
Λ	5.68
Γ_{ref}	4.99
Γ_{max}	$4 \times \Gamma_{ref}$
Γ_{min}	0
$\delta\Gamma$	$\Gamma_{ref}/40$
Γ_{ros}	Γ_{ref}

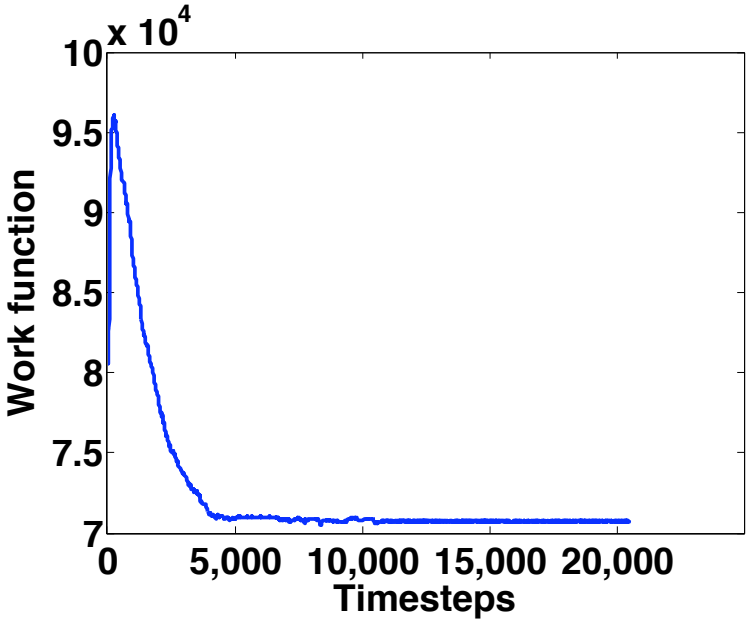

Figure 5.9: The work function first increases as Γ is increased according to Equations 5.1 and 5.3, and it decreases thereafter as the tissue relaxes through elongation.

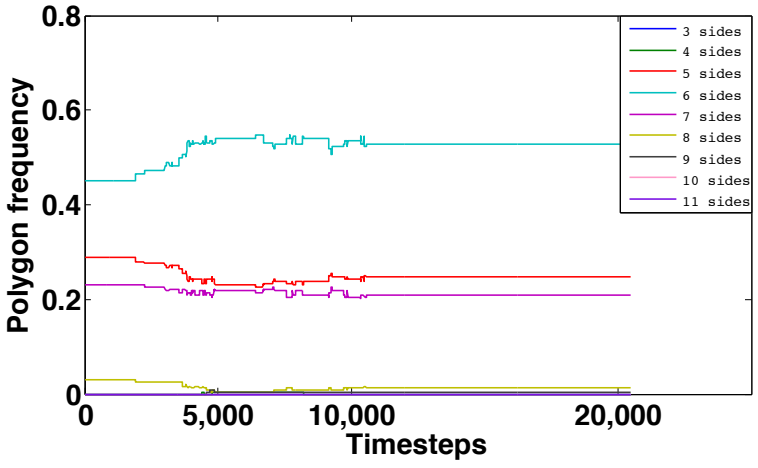

Figure 5.10: The polygonal distribution reaches a new steady state.

Secondly, the number of rosettes in much higher in this case (Figure 5.12). Interestingly, rosette number normalised by the total number of cells in the tissue reaches a dynamic equilibrium.

The total number of T1 transitions is more than two orders of magnitude higher than the T1 rate with the lower noise and importantly, it does not saturate as it did in the low noise scenario (Figure 5.13). This means that the tissue remains active and does not fall into a 'deep' local minimum. As shown in Figure 5.13, several cells delaminate as a result of cell rearrangemets. Work function and the polygonal frequency graphs are shown in Figure 5.14, and indicate that the tissue reaches some sort of dynamic equilibrium, in which constant cell rearrangements drive further elongation. This corresponds to the scenario in which there are several rounds of cell intercalations as is the case in *Drosophila* germband.

Finally, as an illustration, junctions with a high value of contractility Γ are coloured yellow in Figure 5.16. It is instructive to note that the resulting pattern of high contractility cables resembles the supracellular actin cables described by Blankenship et al ([79]). It is therefore possible that the observed actin cables emerge as a result of the alignment of neighbouring cells driven by high contractility, and that no additional cross-cellular signaling is required for their formation.

5.6 Discussion

The results of this computational study hint at the possibility that noise in a biological system is not always a hindrance to the proper proceeding of developmental processes, but it can have precisely the opposite role: noise can be a key ingredient in a morphogenetic event.

As shown by the simulations in this chapter, tissue evolution can be vastly different if only the level of fluctuation in the mechanical properties is changed. For the low value of noise, the tissue extends in length in response to the directional bias in contractility, but mainly through the lengthening of individual cells (Figure 5.6). Importantly, the process of extension ceases once the individual cells have reached a certain cellular aspect ratio beyond which any further extension is presumably prevented by an unacceptable increase in the work function. There is little cellular rearrangement by way of neighbour exchanges, which is in clear contrast to the intercalating cellular

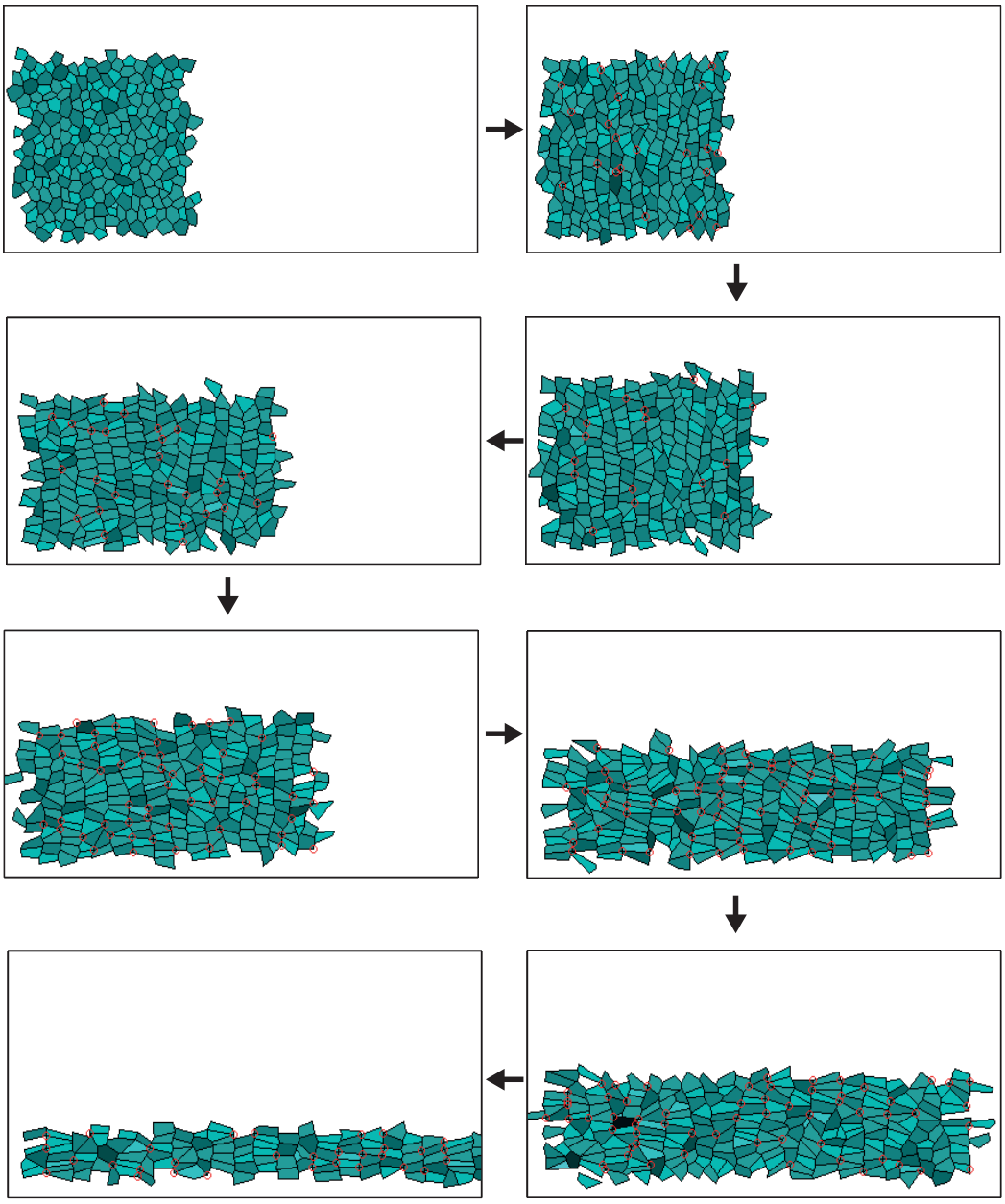

Figure 5.11: Stills showing evolution of tissue with high noise. Tissue aspect ratio changes to approximately 24 : 1. Individual cells both elongate and intercalate. Rosettes form much more often than in the simulation with low noise (encircled in red).

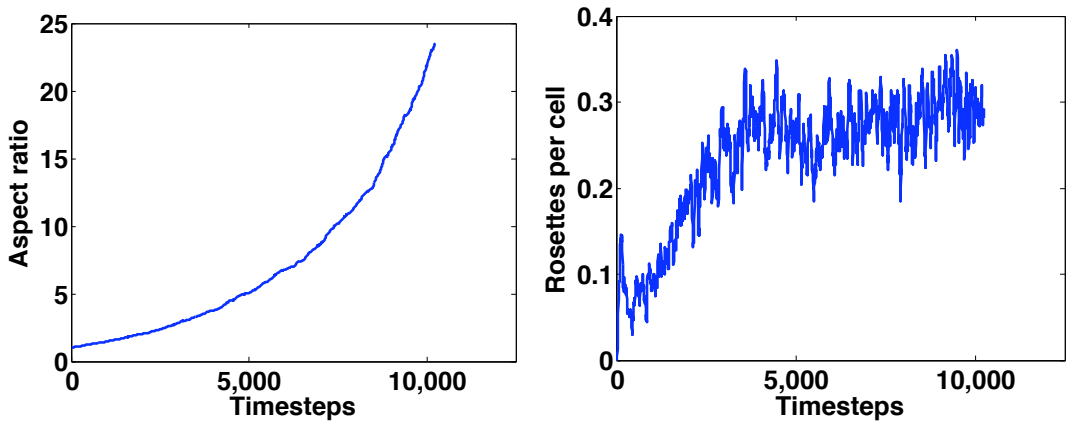

Figure 5.12: (Left) The aspect ratio changes as the tissue elongates when a directional bias in contractility Γ is introduced. (Right) Numerous rosettes form in the process.

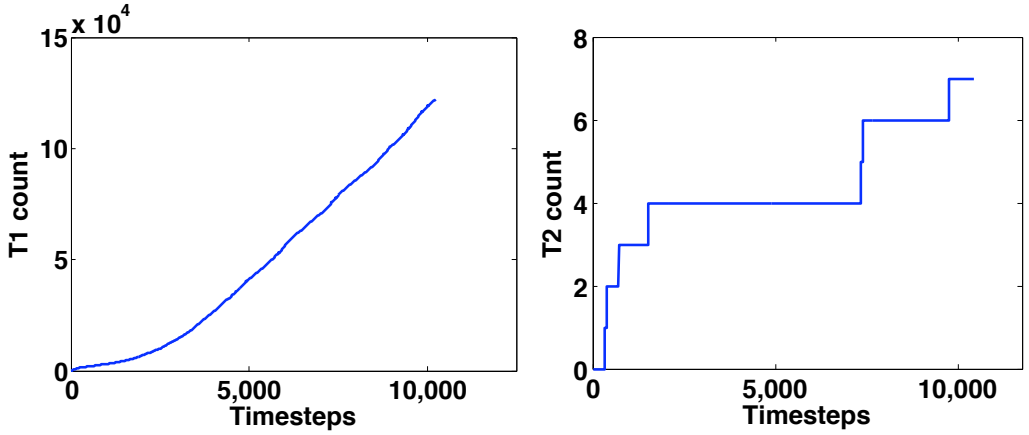

Figure 5.13: Cumulative distribution of T1 and T2 transitions.

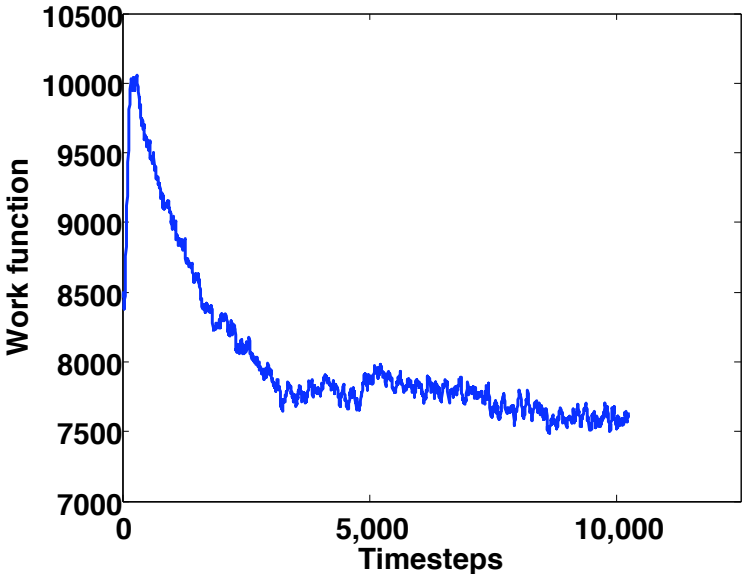

Figure 5.14: The work function first increases as Γ is increased according to Equations 5.1 and 5.3, and it decreases thereafter as the tissue relaxes through elongation and cell intercalation.

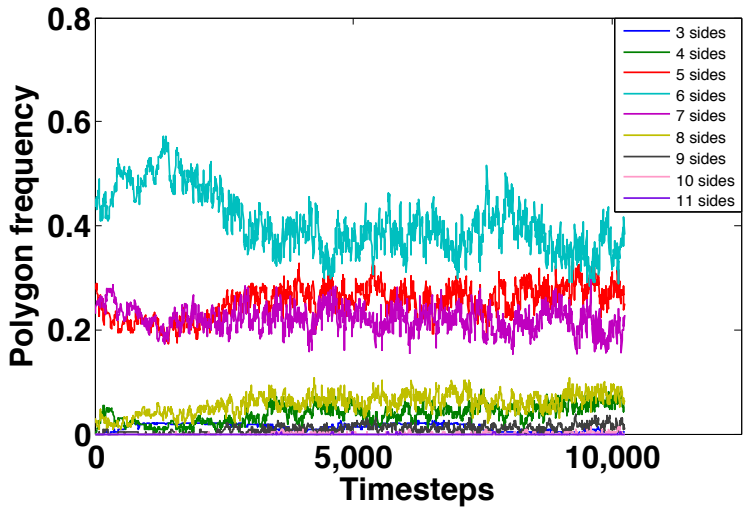

Figure 5.15: The polygonal distribution during the evolution.

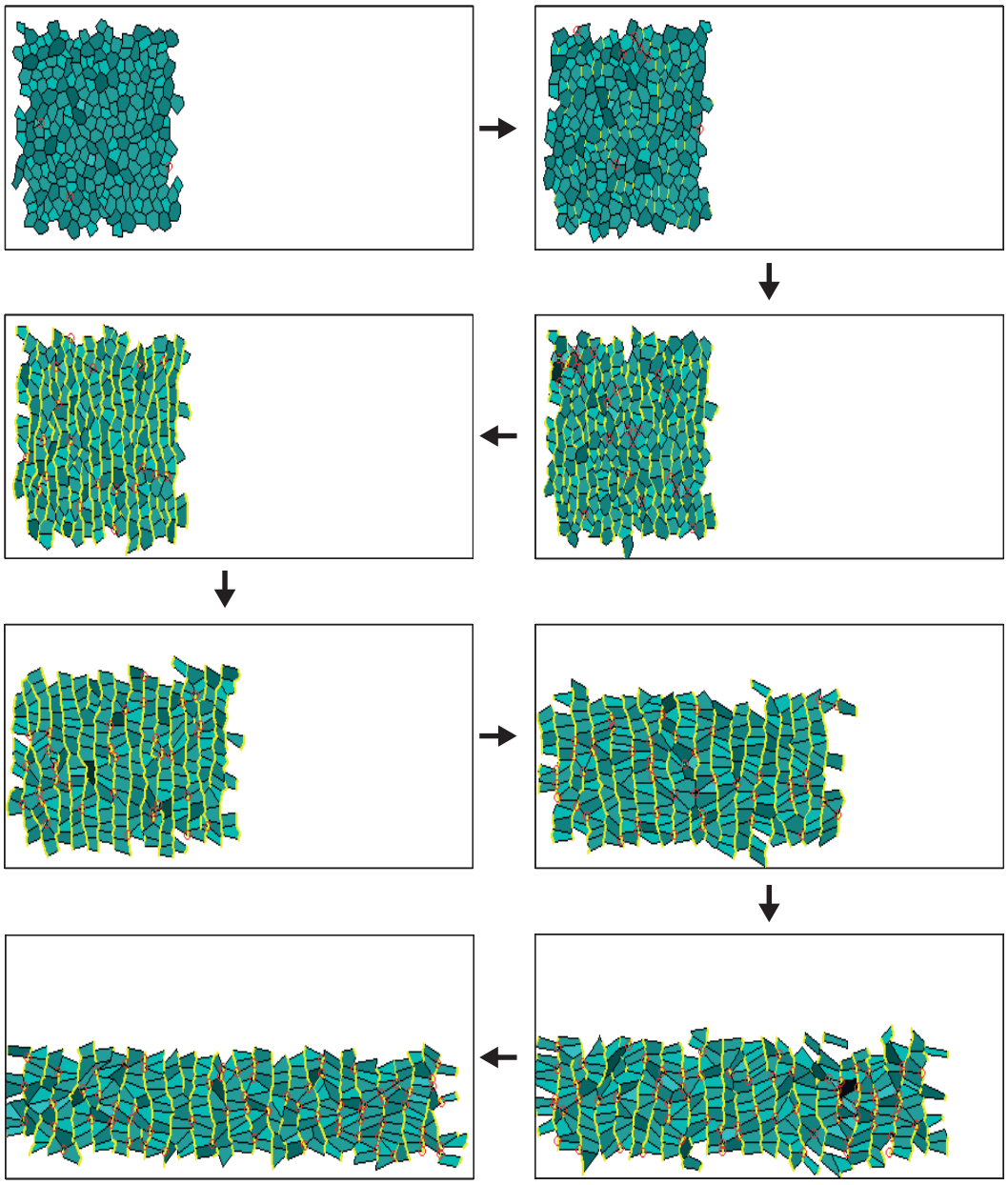

Figure 5.16: Stills showing the formation of actin cables. If $\Gamma > 2 * \Gamma_{ref}$, the junction is coloured yellow, and if $\Gamma > 3 * \Gamma_{ref}$, the junction is drawn with a thicker yellow line.

dynamics during *Drosophila* convergent extension.

Remarkably, increasing the level of noise in the computational simulation completely alters tissue evolution. With an increase in fluctuations, cells exchange neighbours more easily and the uniaxial bias in contractility induces the formation of rosettes. Tissue extends in the direction perpendicular to the direction of contractility enrichment, but in this case, the extension is not only the result of the change in the aspect ratio of individual cells, but it is also due to oriented neighbour exchanges, so that cells intercalate and this results in the depletion of the number of cells along the vertical axis. In contrast to the tissue with the low level of noise, the high noise tissue does not cease to elongate horizontally, and the rate of change of the aspect ratio does not show signs of abating (Figure 5.12).

Myosin II flows in pulses towards the vertical junctions, and this pulsing creates fluctuations in the value of effective cell junctional contractility. These fluctuations could conceivably be analogous to the role of noise in the work function of the computational model, suggesting a possible direction for further study of the role of medial Myosin pulses.

Chapter 6

Conclusion

In this thesis, we study how forces at interfaces between cells in developing epithelia affect global tissue topology. To this end, we develop a computational model of epithelial tissue mechanics.

Making use of the model, we learn in Chapter 2 that the timing of cell divisions affects tissue topology: if cell cycles are synchronised and coordinated, the tissue will resemble a regular hexagonal lattice more closely than when cell division events are uncoordinated. We also find that developing tissues which are free to expand as a result of growth and division of their cells approach a different steady state geometry when compared with tissues of fixed size with ongoing cell divisions and cell growth. This predicts that the geometry of *Drosophila* imaginal wing disc during larval development will be different from the geometry of *Drosophila* notum during pupal development, even if the mechanical properties of cellular junctions are the same in the two tissues.

It is highly likely that mechanical properties of cellular junctions undergo fluctuations in time, in response to internal cellular dynamics. By looking at steady state geometries of tissues with different intensity of noise, we conclude that noise helps the tissue to *anneal* (by analogy to glasses). Thus, in general, developing tissues with high levels of noise are expected to resemble a regular hexagonal lattice more closely than tissues with low values of noise. The exception is the situation when the tissue is already at the global minimum of the potential energy, i.e. it is already packed in a regular hexagonal lattice, then high noise would have the opposite effect and it would induce disorder and deviation from the regular hexagonal lattice.

The role of noise is further discussed in Chapter 5, when we reproduce rosette formation during convergent extension only for sufficiently high levels of noise. When noise if low, polarised acto-myosin affects cell shape by extending the cell along the direction of axis elongation, without concomitant neighbour exchanges (T1 transitions). Therefore, the tissue axis elongates as a result of elongation of individual cells and there is no cell intercalation and repacking, contrary to what is observed in *Drosophila* embryos. However, when noise is increased, cells start exchanging neighbours and forming rosettes. These observations are interesting, since they show how stochasticity in development can be instrumental in guiding tissue organisation. Further steps might involve characterising the noise better, for example by determining its spectrum.

The central result of the thesis is the finding that mechanical forces at the cellular interfaces can push live cells out of the tissue, as presented in Chapter 3. The rate of live cell delamination is found to be correlated with tissue compression and with geometric anisotropy. In collaboration with biologists Eliana Marinari and Buzz Baum, we find that such live cell delaminaton indeed occurs in the *Drosophila* notum, probably in order to limit tissue overcrowding and thus modulate tissue uniformity as cells proliferate during development. Mechanically induced live cell delamination is hence a newly identified homeostatic process.

Finally, in Chapter 4, we study how global equilibria of the work function describing junctional forces depend on the value of junctional contractility. By analysing the phase transition between an ordered and a disordered geometry, we find that an increase in contractility alone can drive the tissue to repack into a regular hexagonal lattice. This may be relevant for understanding hexagonal repacking of developing tissues such as *Drosophila* imaginal wing discs which commence hexagonal repacking concurrently with the establishment of planar cell polarity in the tissue. The localisation of proteins at cellular junctions during the onset of planar cell polarity is expected to change mechanical properties of junctions such as their contractility. The findings are also relevant for understanding hexagonal repacking of the *Drosophila* notum, in which a significant increase in junctional contractility is observed as the tissue approaches a regular hexagonal lattice at the end of pupal development.

Bibliography

[1] **Lewis J., Davies A.**, (2002) 'Planar Cell Polarity in the Inner Ear: How Do Hair Cells Acquire Their Oriented Structure?', *J Neurobiol* ***53****,190 201*

[2] **López-Schier H., Hudspeth A. J.** (2006) "A two-step mechanism underlies the planar polarization of regenerating sensory hair cells", *PNAS* ***103*** *49, 18615-18620*

[3] **Hudspeth A.J.** (2008) 'Making an effort to listen: mechanical amplification in the ear', *Neuron* ***59*** *4*

[4] **Butcher D.T., Alliston T., Weaver V.M.** (2009) "A tense situation: forcing tumour progression", *Nature Reviews Cancer* ***9*** *108-122*

[5] **Zeitlinger J., Bohmann D.** (1999) 'Thorax closure in Drosophila: involvement of Fos and the JNK pathway', *Development* ***126*** *3947*

[6] **Käfer J., Hayashi T., Marée A.F.M., Carthew R.W., Graner F.** (2007) 'Cell adhesion and cortex contractility determine cell patterning in the Drosophila retina', *PNAS* ***104*** *18549-18554*

[7] **Hayashi T, Carthew R.W.** (2004) 'Surface mechanics mediate pattern formation in the developing retina', *Nature* ***431*** *647-652*

[8] **Classen A-K, Anderson K.I., Marois E., Eaton S.** (2005) 'Hexagonal Packing of Drosophila Wing Epithelial Cells by the Planar Cell Polarity Pathway', *Dev Cell,* ***9*** *805-817*

[9] **Wootton R.** (1992) 'Functional Morphology of Insect Wings', *Ann Rev of Entom* ***37****, 113*

[10] **Alberts B., Bray D., Lewis J., Raff M., Roberts K., Watson J.D.** (1994) 'Molecular Biology of the Cell', *Garland Science*

[11] **Simpson P.**, (1990) 'Lateral inhibition and the development of the sensory bristles of the adult peripheral nervous system of Drosophila', *Development* ***109**, 509-519*

[12] **Simpson, P.**, (1996) 'Drosophila development: A prepattern for sensory bristles', *Curr. Biol.* ***6**, 948-950*

[13] **Simpson P., Woehl R. and Usui K.**, (1999) 'The development and evolution of bristle patterns in Diptera', *Development* ***126**, 1349-1364*

[14] **Calleja M., Renaud O., Usui 2., Pistillo D., Morata G., Simpson P.** (2002) 'How to pattern an epithelium: lessons from achaete-scute regulation on the notum of Drosophila', *Gene* ***292** 1-2, 1-12*

[15] **Doyle K., Hogana J., Lestera M., Collier S.** (2008) 'The Frizzled Planar Cell Polarity signaling pathway controls Drosophila wing topography', *Dev Biol* ***317** 1 354-367*

[16] **Lawrence P.A., Shelton P.M.J.** (1975) "The determination of polarity in the developing insect retina", *J Embryol Exp Morphol* ***33**, 471-486*

[17] **Klein T.J., Mlodzik M.** (2005) "Planar Cell Polarization: An Emerging Model Points in the Right Direction", *Ann Rev of Cell and Dev Bio* ***21**, 155-176*

[18] **Amonlirdviman K., Khare N.A., Tree D.R.P., Chen W-S, Axelrod J.D., Tomlin C.J.**, (2005) 'Mathematical Modeling of Planar Cell Polarity to Understand Domineering Nonautonomy', *Science* ***307** (5708), 423*

[19] **Vinson C.R., Adler P.N.** (1987) "Directional non-cell autonomy and the transmission of polarity information by the frizzled gene of Drosophila", *Nature* ***329**, 549 - 551*

[20] **Saburi S., McNeill H.**, (2005) 'Organising cells into tissues: New roles for cell adhesion molecules in planar cell polarity', *Cur. Op. in Cell Bio.,* ***17** (5 SPEC. ISS.), 482-488*

[21] **Zallen, J.A., and Zallen, R.**, (2004) 'Cell-pattern disordering during convergent extension in Drosophila', *J. Phys. Condens. Matter **16**, S5073-S5080*

[22] **Rauzi M., Verant P., Lecuit T., Lenne P.F.** (2008) 'Nature and anisotropy of cortical forces orienting Drosophila tissue morphogenesis', *'Nat Cell Biol **10**, 1401-1410*

[23] **Bertet C, Lecuit T.**, (2009) 'Planar polarity and short-range polarization in Drosophila embryos', *Semin Cell Dev Biol* [Epub ahead of print]

[24] **Montcouquiol M, Sans N, Huss D, Kach J, Dickman JD, Forge A, Rachel RA, Copeland NG, Jenkins NA, Bogani D, Murdoch J, Warchol ME, Wenthold RJ, Kelley MW.**, (2006) 'Asymmetric localization of Vangl2 and Fz3 indicate novel mechanisms for planar cell polarity in mammals', *J Neurosci **26** (19), 5265-75*

[25] **Glazier G. A., Graner F.**, (1992) 'Simulation of biological cell sorting using a two-dimensional exended Potts model', *Phys. Rev. Lett. **69**, 2013-2016*

[26] **Steinberg M.S.** (1963) 'Reconstruction of Tissues by Dissociated Cells', *Science **141** 3579, 401 - 408*

[27] **Brodland G.W.** (2002) 'The Differential Interfacial Tension Hypothesis (DITH): A Comprehensive Theory for the Self-Rearrangement of Embryonic Cells and Tissues', *J Biomech Eng **124** 2 188-197*

[28] **Steinberg M.S.** (1970) 'Does differential adhesion govern self-assembly processes in histogenesis? Equilibrium configurations and the emergence of a hierarchy among populations of embryonic cells', *J Exp Zool **173** (4), 395-433*

[29] **Green J.B.A.** (2008) 'Sophistications of cell sorting' *Nature Cell Biol **10** 375-377*

[30] **Plateau J.** (1873) 'Statique experimentale et theorique des liquides soumis aux seules forces moleculaires', *Gauthier-Villars*

[31] **Taylor J.E.** (1976) 'The Structure of Singularities in Soap-Bubble-Like and Soap-Film-Like Minimal Surfaces ', *Ann of Math, 2nd Series 103 3, 489-539*

[32] **Weaire Denis**, (1999) 'The Physics of Foams', OUP

[33] **Merks R.M.H., Glazier J.A.**, (2005), 'A cell-centered approach to developmental biology', *Physica A **352** 113130*

[34] **Glazier G. A., Graner F.**, (1993) 'Simulation of the differential adhesion driven rearrangement of biological cells', *Phys. Rev. E **47**, 2128-2154*

[35] **Hufnagel, L., Teleman, A.A., Rouault, H., Cohen, S.M., and Shraiman, B.I.** (2007) 'On the mechanismof wing size determination in fly development', *Proc. Natl. Acad. Sci. USA **104** 3835-3840*

[36] **Farhadifar R., Röper J., Aigouy B., Eaton S., Jülicher F.**, (2007) 'The Influence of Cell Mechanics, Cell-Cell Interactions, and Proliferation on Epithelial Packing', *Current Biology **17**, 2095-2104*

[37] **Axelrod J.D.** 'Cell Shape in Proliferating Epithelia: A Multifaceted Problem', *Cell **126** 4 643-645*

[38] **Rivier N., Lissowski A.** (1982) 'On the correlation between sizes and shapes of cells in epithelial mosaics', *J of Phys A: Math and Gen **15**, L143-L148*

[39] **Dubertet B, Rivier N.**, (1997) 'The Renewal of the Epidermis: A Topological Mechanism', *Biophys. J. **73** 38-44*

[40] **da Fontoura Costa L., Rocha F., de Lima S.M.A.**, (2006) 'Characterising polygonality in biological structures', *Phys Rev E **73** 011913*

[41] **Gibson M.C., Patel A.B., Nagpal R., Perrimon, N.** (2006) 'The emergence of geometric order in proliferating metazoan epithelia', *Nature **442**, 1038-1041*

[42] **Cowan R., Morris V.B.** (1988) 'Division rules for polygonal cells', *J Theor Biol. **131** 1, 33-42*

[43] **Press W.H., Teukolsky S.A., Vetterling W.T., and Flannery B.P.** (1992) 'Numerical Recipes in C: the Art of Scientic Com- puting', Second Edition, *CUP*).

[44] **Ziherl P., Hočevar A.** (2009) 'Degenerate polygonal tilings in simple animal tissues', *Phys Rev E **80**, 011904*

[45] **Brakke K.** (1992) "The surface evolver", *Exp Math **1**, 141*

[46] **Edwards S.F., Oakeshott R.B.S.** (1989) 'Theory of powders', *Physica A **157**, 1080*

[47] **Blumenfeld R., Edwards S.F.** (2003) 'Granular entropy: Explicit calculations for planar assemblies', *Phys Rev Lett **90**, 114303*

[48] **Blumenfeld R., Edwards S.F.** (2006) 'Geometric partition functions of cellular systems: Explicit calculation of the entropy in two and three dimensions', *Eur Phys J E **19**, 23*

[49] **Martin P. Stewart M.P., Helenius J., Toyoda Y., Ramanathan S.P., Muller D.J., Hyman A.A.** (2011) "Hydrostatic pressure and the actomyosin cortex drive mitotic cell rounding", *Nature **469** 226230*

[50] **Shraiman B.I.** (2005) 'Mechanical feedback as a possible regulator of tissue growth', *PNAS **102** 3318-3323*

[51] **Wartlick O., Mumcu P., Kicheva A., Bittig T. Seum C., Jülicher F., González-Gaitán F.** (2011) "Dynamics of Dpp Signaling and Proliferation Control", *Science **331** 6021 1154-1159*

[52] **Rosenblatt J., Raff M.C., Cramer L.P.** (2001) "An epithelial cell destined for apoptosis signals its neighbors to extrude it by an actin- and myosin-dependent mechanism", *Current Biology **11** 1847-1857*

[53] **Basan M. et al** (2009) "Homeostatic competition drives tumor growth and metastasis nucleation", *HFSP J. **3** 4 265-272*

[54] **Marinari E., Mehonic A., Curran S., Gale J., Duke T., Baum B.** (submitted to Nature March 2011) "Live cell delamination counterbalances epithelial growth to limit tissue overcrowding"

[55] **Bittig T., Wartlick O., Kicheva A., González-Gaitán, Jülicher F.**, (2008) 'Dynamics of anisotropic tissue growth', *New J. Phys. **10** 063001*

[56] **K. P. Landsberg, R. Farhadifar, J. Ranft, D. Umetsu, T. J. Widmann, T. Bittig, A. Said, F. Jlicher and C. Dahmann**, (2009) 'Increased Cell Bond Tension Governs Cell Sorting at the Drosophila Anteroposterior Compartment Boundary', *Current Biology **19**(22), 1950-1955*

[57] **Ranft J., Basan M., Elgeti J., Joanny J.-F., Prost J., Jülicher F.** (2010) "Fluidization of Tissues by Cell Division and Apoptosis", *PNAS **107** 20863*

[58] **Solon J., Kaya-Copur A., Colombelli J., Brunner D.** (2007) "Pulsed Forces Timed by a Ratchet-like Mechanism Drive Directed Tissue Movement during Dorsal Closure", *Cell **137** 1331-1342*

[59] **Solon J., Kaya-Copur A., Colombelli J., Brunner D.**, (2009) 'Pulsed forces timed by a ratchet-like mechanism drive directed tissue movement during dorsal closure', *Cell **137** 1331-1342*

[60] **Aegerter-Wilmsen T., Smith A.C., Christen A.J., Aegerter C.M., Hafen E. Basler K.** (2010) "Exploring the effects of mechanical feedback on epithelial topology", *Development **137**, 499-506*

[61] **Aigouy B., Farhadifar R., Staple D.B., Sagner A., Röper J.-C., Jülicher F. Eaton S.** (2010) "Cell Flow Reorients the Axis of Planar Polarity in the Wing Epithelium of Drosophila", *Cell **142** (5) 773-786*

[62] **Hengartner, M.O.** (2000) "The biochemistry of apoptosis", *Nature **407**, 770-776*

[63] **Manjón C., Sánchez-Herrero E., Suzanne M.** (2007) "Sharp boundaries of Dpp signalling trigger local cell death required for Drosophila leg morphogenesis", *Nature Cell Biology **9** 57 - 63*

[64] **Toyama Y., Peralta X.G., Wells A.R., Kiehart D.P., Edwards G.S.** (2008) 'Apoptotic Force and Tissue Dynamics During Drosophila Embryogenesis', *Science **19** 321, 1683-1686*

[65] **Nagpal R., Patel A., Gibson M.C.** (2008) 'Epithelial Topology', *BioEssays **30**, 260-266*

[66] **Patel A.B., Gibson W.T., Gibson M.C., Nagpal R.** (2009) 'Modeling and Inferring Cleavage Patterns in Proliferating Epithelia', *PLoS Comput Biol **5)** (6) e1000412*

[67] **Théry M, Jiménez-Dalmaroni A, Racine V, Bornens M, Jülicher F.**, (2007) 'Experimental and theoretical study of mitotic spindle orientation', *Nature **447** 493-498*

[68] **Cohen M., Georgiou M., Stevenson N.L., Miodownik M, Baum B.** (2010) "Dynamic Filopodia Transmit Intermittent Delta-Notch Signaling to Drive Pattern Refinement during Lateral Inhibition", *Developmental Cell* ***19****, 78-89*

[69] **Lewis F.T,**, (1926) 'The effect of cell division on the shape and size of hexagonal cells' , *Anat. Rec.* ***33****, 5, 331-355*

[70] **Lewis F.T,**, (1928) 'The correlation between cell division and the shapes and sizes of prismatic cells in the epidermis of cucumis' , *Anat. Rec.* ***38****, 3, 341-376*

[71] **Graustein W.C.**, (1931) 'On the Average Number of Sides of Polygons of a Net' , *Ann. of Math., 2nd Series,* ***32****, No. 1, 149-153*

[72] **Baum B.** (2004) 'Animal Development: Crowd Control', *Curr Bio* ***14*** *17 R716R718*

[73] **Irvine K.D., Wieschaus E.** (1994) 'Cell intercalation during Drosophila germband extension and its regulation by pair-rule segmentation genes', *Development* ***120*** *4 827-41*

[74] **Lecuit T., Lenne P-F.**, (2007) 'Cell surface mechanics and the control of cell shape, tissue patterns and morphogenesis', *Nature Rev Mol Cell Biol* ***8****, 633-644*

[75] **Lecuit T.** (2008) 'Developmental mechanics: cellular patterns controlled by adhesion, cortical tension and cell division', *HFSP J* ***2*** *(2) 72-78*

[76] **Bertet C., Sulak L., Lecuit, T.**, (2004) 'Myosin-dependent junction remodelling controls planar cell intercalation and axis elongation', *Nature* ***429****, 667-671*

[77] **Zallen J.A., Wieschaus E.**, (2004) 'Patterned Gene Expression Directs Bipolar Planar Polarity in Drosophila', *Dev Cell* ***6*** *3 343-355*

[78] **Kasza M., Zallen J.** (2010) "Dynamics and regulation of contractile actin-myosin networks in morphogenesis", *Curr Op in Cell Bio* ***23*** *1-9*

[79] **Blankenship, J. T., Backovic, S. T., Sanny, J.S.P., Weitz, O., Zallen, J. A.**, (2006) 'Multicellular Rosette Formation Links Planar Cell Polarity to Tissue Morphogenesis', ***11*** *4 459-470*

[80] **Rauzi M. et al** (2010) "Planar polarized actomyosin contractile flows control epithelial junction remodelling", *Nature **468** 1110-1114*

[81] **Zajac M., Jones G.L., Glazier J.A.** (2000) "Model of Convergent Extension in Animal Morphogenesis", *Phys. Rev. Lett. **85** 2022-2025*

[82] **Concha M.L. and Adams R.J** (1998) "Oriented cell divisions and cellular morphogenesis in the zebrafish gastrula and neurula: a time-lapse analysis", *Development **125***, pp. 983994